ISBN 0-612-16486-1

Name TODD MICHAEL FULLER

Dissertation Abstracts International is arranged by broad, general subject categories. Please select the one subject which most nearly describes the content of your dissertation. Enter the corresponding four-digit code in the spaces provided.

ASTRONOMY AND ASTROPHYSICS — SUBJECT TERM

0606 — SUBJECT CODE

U·M·I

Subject Categories

THE HUMANITIES AND SOCIAL SCIENCES

COMMUNICATIONS AND THE ARTS
Architecture 0729
Art History 0377
Cinema 0900
Dance 0378
Fine Arts 0357
Information Science 0723
Journalism 0391
Library Science 0399
Mass Communications 0708
Music 0413
Speech Communication 0459
Theater 0465

EDUCATION
General 0515
Administration 0514
Adult and Continuing 0516
Agricultural 0517
Art 0273
Bilingual and Multicultural 0282
Business 0688
Community College 0275
Curriculum and Instruction 0727
Early Childhood 0518
Elementary 0524
Finance 0277
Guidance and Counseling 0519
Health 0680
Higher 0745
History of 0520
Home Economics 0278
Industrial 0521
Language and Literature 0279
Mathematics 0280
Music 0522
Philosophy of 0998
Physical 0523
Psychology 0525
Reading 0535
Religious 0527
Sciences 0714
Secondary 0533
Social Sciences 0534
Sociology of 0340
Special 0529
Teacher Training 0530
Technology 0710
Tests and Measurements 0288
Vocational 0747

LANGUAGE, LITERATURE AND LINGUISTICS
Language
- General 0679
- Ancient 0289
- Linguistics 0290
- Modern 0291

Literature
- General 0401
- Classical 0294
- Comparative 0295
- Medieval 0297
- Modern 0298
- African 0316
- American 0591
- Asian 0305
- Canadian (English) 0352
- Canadian (French) 0355
- English 0593
- Germanic 0311
- Latin American 0312
- Middle Eastern 0315
- Romance 0313
- Slavic and East European 0314

PHILOSOPHY, RELIGION AND THEOLOGY
Philosophy 0422
Religion
- General 0318
- Biblical Studies 0321
- Clergy 0319
- History of 0320
- Philosophy of 0322

Theology 0469

SOCIAL SCIENCES
American Studies 0323
Anthropology
- Archaeology 0324
- Cultural 0326
- Physical 0327

Business Administration
- General 0310
- Accounting 0272
- Banking 0770
- Management 0454
- Marketing 0338

Canadian Studies 0385
Economics
- General 0501
- Agricultural 0503
- Commerce-Business 0505
- Finance 0508
- History 0509
- Labor 0510
- Theory 0511

Folklore 0358
Geography 0366
Gerontology 0351
History
- General 0578
- Ancient 0579
- Medieval 0581
- Modern 0582
- Black 0328
- African 0331
- Asia, Australia and Oceania 0332
- Canadian 0334
- European 0335
- Latin American 0336
- Middle Eastern 0333
- United States 0337

History of Science 0585
Law 0398
Political Science
- General 0615
- International Law and Relations 0616
- Public Administration 0617

Recreation 0814
Social Work 0452
Sociology
- General 0626
- Criminology and Penology 0627
- Demography 0938
- Ethnic and Racial Studies 0631
- Individual and Family Studies 0628
- Industrial and Labor Relations 0629
- Public and Social Welfare 0630
- Social Structure and Development 0700
- Theory and Methods 0344

Transportation 0709
Urban and Regional Planning 0999
Women's Studies 0453

THE SCIENCES AND ENGINEERING

BIOLOGICAL SCIENCES
Agriculture
- General 0473
- Agronomy 0285
- Animal Culture and Nutrition 0475
- Animal Pathology 0476
- Food Science and Technology 0359
- Forestry and Wildlife 0478
- Plant Culture 0479
- Plant Pathology 0480
- Plant Physiology 0817
- Range Management 0777
- Wood Technology 0746

Biology
- General 0306
- Anatomy 0287
- Biostatistics 0308
- Botany 0309
- Cell 0379
- Ecology 0329
- Entomology 0353
- Genetics 0369
- Limnology 0793
- Microbiology 0410
- Molecular 0307
- Neuroscience 0317
- Oceanography 0416
- Physiology 0433
- Radiation 0821
- Veterinary Science 0778
- Zoology 0472

Biophysics
- General 0786
- Medical 0760

EARTH SCIENCES
Biogeochemistry 0425
Geochemistry 0996
Geodesy 0370
Geology 0372
Geophysics 0373
Hydrology 0388
Mineralogy 0411
Paleobotany 0345
Paleoecology 0426
Paleontology 0418
Paleozoology 0985
Palynology 0427
Physical Geography 0368
Physical Oceanography 0415

HEALTH AND ENVIRONMENTAL SCIENCES
Environmental Sciences 0768
Health Sciences
- General 0566
- Audiology 0300
- Chemotherapy 0992
- Dentistry 0567
- Education 0350
- Hospital Management 0769
- Human Development 0758
- Immunology 0982
- Medicine and Surgery 0564
- Mental Health 0347
- Nursing 0569
- Nutrition 0570
- Obstetrics and Gynecology 0380
- Occupational Health and Therapy 0354
- Ophthalmology 0381
- Pathology 0571
- Pharmacology 0419
- Pharmacy 0572
- Physical Therapy 0382
- Public Health 0573
- Radiology 0574
- Recreation 0575
- Speech Pathology 0460
- Toxicology 0383

Home Economics 0386

PHYSICAL SCIENCES

Pure Sciences

Chemistry
- General 0485
- Agricultural 0749
- Analytical 0486
- Biochemistry 0487
- Inorganic 0488
- Nuclear 0738
- Organic 0490
- Pharmaceutical 0491
- Physical 0494
- Polymer 0495
- Radiation 0754

Mathematics 0405
Physics
- General 0605
- Acoustics 0986
- Astronomy and Astrophysics 0606
- Atmospheric Science 0608
- Atomic 0748
- Electronics and Electricity 0607
- Elementary Particles and High Energy 0798
- Fluid and Plasma 0759
- Molecular 0609
- Nuclear 0610
- Optics 0752
- Radiation 0756
- Solid State 0611

Statistics 0463

Applied Sciences

Applied Mechanics 0346
Computer Science 0984
Engineering
- General 0537
- Aerospace 0538
- Agricultural 0539
- Automotive 0540
- Biomedical 0541
- Chemical 0542
- Civil 0543
- Electronics and Electrical 0544
- Heat and Thermodynamics 0348
- Hydraulic 0545
- Industrial 0546
- Marine 0547
- Materials Science 0794
- Mechanical 0548
- Metallurgy 0743
- Mining 0551
- Nuclear 0552
- Packaging 0549
- Petroleum 0765
- Sanitary and Municipal 0554
- System Science 0790

Geotechnology 0428
Operations Research 0796
Plastics Technology 0795
Textile Technology 0994

PSYCHOLOGY
General 0621
Behavioral 0384
Clinical 0622
Developmental 0620
Experimental 0623
Industrial 0624
Personality 0625
Physiological 0989
Psychobiology 0349
Psychometrics 0632
Social 0451

Contents

Certificate of Examination iii

List of Figures iv

List of Tables vi

Acknowledgments vii

Abstract viii

1 Introduction 1

2 Observations 8

3 Image reduction 18

3.1 Overscan subtraction 18

3.2 Flat fielding 22

3.3 Mosaicking images 25

4 Surface photometry 28

4.1 Object removal 29

4.2 Creation of artificial images 31

4.3 Testing `ellipse` 33

4.4 Errors incurred by seeing 34

4.5 Errors incurred by sky subtraction 37

4.6 Computation of isophote intensity 40

5 Transformation to standard magnitudes **51**

5.1 Standard star photometry 51

5.2 Transformation equations 52

5.3 Extinction and K-corrections 55

6 Results **58**

6.1 Sky measurement 58

6.2 Surface photometry 59

7 Discussion **75**

7.1 Isophote position angles 75

7.2 Isophote ellipticities 77

7.3 Surface photometry 78

7.4 de Vaucouleurs parameters 83

8 Summary **86**

Glossary **88**

Appendix 1: ANNULI code listing **94**

Curriculum Vitae **112**

Certificate of Examination

Saint Mary's University

Department of Astronomy and Physics

Dr. Michael J. West (Supervisor)

Associate Professor of Astronomy and Physics

Saint Mary's University

Dr. James M. Schombert

NASA

Dr. David Clarke

Associate Professor of Astronomy and Physics

Saint Mary's University

Dr. George Mitchell

Professor of Astronomy and Physics

Saint Mary's University

List of Figures

1 *B* image of 10276 – 0255, the BCG of MKW 2. 10

2 *B* image of 10246 – 0304, the BCG of MKW 2S. 11

3 *B* image of NGC 5920, the BCG of MKW 3S. 12

4 *B* image of NGC 4073, the BCG of MKW 4. 13

5 *B* image of NGC 5400, the BCG of MKW 5. 14

6 *B* image of NGC 6051, the BCG of AWM 4. 15

7 *B* image of NGC 6269, the BCG of AWM 5. 16

8 *B* image of UGC 09799, the BCG of Abell 2052. 17

9 Intensity versus line for an unstable bias 18

10 A raw image with an unstable bias region. 20

11 A two piece cubic spline fit to an overscan region containing three discontinuities. 21

12 Overscan region after a two piece cubic spline subtraction. 21

13 Bias frame, column plot 24

14 Unflattened image, line plot 24

15 Flattened image, line plot 27

16 Mean change in median intensity vs. iteration 27

17 Ellipticity versus semi-major axis, brightest 40% of pixels clipped . . 35

18 Position angle versus semi-major axis, brightest 40% of pixels clipped 36

19 Seeing effects on isophotal magnitude 38

20 Seeing effects on isophote ellipticity 39

21 Seeing effects on isophote position angle 39

22 Effect of an error in sky subtraction on magnitude 41

23 Effect of a 1% error in sky subtraction on isophotal magnitude. . . . 41

24 Effect of a 1% error in sky subtraction on isophote ellipticity. 42

25 Effect of a 1% error in sky subtraction on isophotal position angle. . . 42

26 Consequence of an incorrect ellipticity 48

27 Consequence of an incorrect position angle 48

28 A comparison of `ellipse` and ANNULI 49

29 Measurement of a de Vaucouleurs profile with ANNULI 50

30 Surface brightness profile of UGC 09799 (Abell 2052) 61

31 Surface brightness profile of NGC 6051 (AWM 4) 62

32 Surface brightness profile of NGC 6269 (AWM 5). 63

33 Surface brightness profile of 10276 – 0255 (MKW 2) 64

34 Surface brightness profile of 10246 – 0304 (MKW 2S) 65

35 Surface brightness profile of NGC 5920 (MKW 3S) 66

36 Surface brightness profile of NGC 4073 (MKW 4) 67

37 Surface brightness profile of NGC 5400 (MKW 5) 68

38 Position angle versus radius for poor cluster dominant galaxies. . . . 69

39 Position angle versus radius for poor cluster dominant galaxies. . . . 70

40 Ellipticity versus radius for poor cluster dominant galaxies. 71

41 Ellipticity versus radius for poor cluster dominant galaxies. 72

42 Sky correction needed to register the profiles 82

43 de Vaucouleurs parameters 85

List of Tables

1 POOR CLUSTER LOCATIONS (b1950.0) AND MAGNITUDES 7

2 NUMBER OF EXPOSURES OF PROGRAM OBJECTS 9

3 STANDARD MAGNITUDE TRANSFORMATION COEFFICIENTS, B FILTER 57

4 STANDARD MAGNITUDE TRANSFORMATION COEFFICIENTS, R FILTER 57

5 DOMINANT GALAXY COLOURS AND EXTINCTION COEFFICIENTS . . 60

6 SKY BRIGHTNESSES 73

7 DE VAUCOULEURS PARAMETERS 74

Acknowledgments

It is with pleasure that I express my thanks to the various people who have contributed to this thesis:

To Dr. Michael West: Thank you for your excellent supervision. With your guidance, this has been a very rewarding experience. Your timely words of encouragement in frustrating periods were very appreciated. Thanks also for the use of your office! I've been told by many people that the most important factor for this degree is the choice of a supervisor. I chose very wisely.

To Dr. Terry Bridges: I couldn't have gotten through this without your observational expertise, which you have so graciously shared. Since January 22, 1996, we have exchanged over 100 email messages!

To Dr. James Schombert: Your assistance with various problems encountered was very appreciated. Thanks also for serving as the external reader and giving helpful and explicit recommendations for improving this thesis.

To Dr. David Clarke: You have been a big influence in my choice of topics to pursue for a Ph.D. Thank you also for being on the examination committee.

To Dr. George Mitchell: Thank you for serving as a member on the examination committee, and for your suggestions for improvement.

To Melvin Blake: My good friend, you are always willing to lend an ear; I very much appreciated our numerous discussions on various topics. Thanks for sharing your impressive knowledge of astronomical topics; you helped me out considerably.

Abstract

SURFACE PHOTOMETRY OF THE DOMINANT GALAXIES IN POOR CLUSTERS

Todd M. Fuller September 18, 1996

Surface photometry in B and R is presented for seven brightest cluster galaxies (BCGs) in poor clusters. The primary goal was to detect diffuse envelopes around the BCGs to determine if they are genuine cD galaxies, which have a diffuse stellar envelope that manifests itself as a break in the brightness profile. The poor cluster BCGs did show breaks in their profiles, but these occurred at brighter magnitudes than in cDs and hence was likely produced by a systematic overestimation of the sky intensity. Based on the de Vaucouleurs parameters the poor cluster BCGs are D galaxies, which lack envelopes. Both poor cluster BCGs and rich cluster cD galaxies show similar isophotal flattening and major axis alignments, and therefore must share common formation processes independent of cluster richness. However, since the poor cluster BCGs likely do not have envelopes, a rich cluster environment is necessary for envelope formation.

1 Introduction

The largest galaxies in the Universe were first identified by Matthews, Morgan, and Schmidt (1964). Originally, W. W. Morgan labeled bright elliptical galaxies surrounded by extensive amorphous stellar envelopes "D" galaxies. A subset of these were very much larger and given a special designation: cD, where the "c" stands for supergiant. The primary attributes of these cD galaxies are a large size (3 to 4 times larger than the largest lenticular galaxy in the cluster) and extensive diffuse stellar envelopes of approximately 100 kpc in extent. Some of these galaxies had *very* extensive envelopes 1 to 2 Mpc in size; for comparison, the Andromeda galaxy, our nearest large neighbour, is only 0.7 Mpc away! The distinction between D and cD galaxies was somewhat ambiguous, however, and the cross over point between the two classification was largely up to the observer's discretion. Galaxy classification was usually done by visual examination of photographic plates, but the eye is a poor detector of faint diffuse envelopes, and furthermore the $(1+z)^4$ cosmological dimming factor makes the ability to classify cDs distance dependent. Thus it is not surprising that the same galaxies have been classified differently by different authors (see Dressler, 1984, for a review).

As the study of cD galaxies evolved, so did their definition. In a surface photometry study of 342 elliptical galaxies, Schombert (1987) described brightness profile (i. e., intensity as a function of radius) morphology criteria that quantified the distintions between giant elliptical (gE), D and cD galaxies. In his sample, giant elliptical

galaxies were found to have a power-law slope ($I(r) \propto r^{\beta}$ where I is intensity and r is the radius) of $-1.9 \leq \beta \leq -1.7$, and D galaxy profile slopes were shallower, ranging from -1.7 to -1.2. cD galaxies showed the same slope as D galaxies down to a certain surface brightness, but exhibited a characteristic upturn in their profiles, caused by their large envelopes. These envelopes, even though they have a very low surface brightness, may be as much as ten times the luminosity of the underlying galaxy because of their immense size.

The origin of cD galaxies has been the subject of considerable debate. Geller and Peebles (1976) argued that cD galaxies are simply the bright tail of the galaxy luminosity function, while others (Dressler, 1978) have argued that environmental factors are responsible for the creation of cDs. Most of the evidence favours the latter. Many of the cD galaxies are simply too bright to be continuations of the luminosity function for cluster galaxies. Tremaine and Richstone (1977) derived statistical tests of cluster galaxy luminosities that are independent of the assumed luminosity function, and concluded that the luminosity of the brightest cluster galaxy (BCG) is determined by some special physical process, rather than a statistical sampling of a luminosity function. Also, no cD galaxies are found in the low-density field ($\rho < 1$ galaxy Mpc^{-1}), even though the luminosity functions for cluster and field galaxies are not significantly different.

With a few exceptions, cD galaxies always occupy a preferred position: the centre of dense clusters where the local density is at a maximum, and may reach 10^4 times

the mean galaxy number density. Beers and Geller (1983) showed that galaxies with luminous halos (i. e., D and cD) are located at local surface density maxima of galaxy clusters, and are nearer to these maxima than bright galaxies of other types. This further suggests that cD galaxies are the products of a special environment. The most important piece of evidence that cD galaxies are not simply the brightest galaxies is that between 25 and 50 percent of cD galaxies are multiply nucleated [these are not merely chance projections, see Schneider et al. (1983)]. This is very strong evidence that cDs have undergone special evolutionary processes, probably related to merging and galactic cannibalism in dense environments.

There are four popular theories to explain the origin of cD galaxies (see Schombert, 1988, for a discussion). Two of these, the tidal stripping theory (Malumuth and Richstone, 1984) and merger theory (Ostriker and Hausman, 1977), rely on dynamical processes to create a cD. In the stripping theory, tidal interactions strip stars from cluster members and deposit them onto the central galaxy. The merger theory posits that galactic cannibalism, facilitated by dynamical friction, is responsible for the cD's extreme size, and naturally explains the high incidence of multiple nuclei. Both theories, however, are inconsistent in some respects. Energy arguments indicate that material from mergers will be distributed over an area that is much smaller than the observed cluster envelope. The orbital energy and hence orbital velocity for a merging galaxy is similar to the velocity dispersion of the BCG. But, a megaparsec sized envelope requires a much larger velocity dispersion than the typical value of

300 km s^{-1} for BCGs. This is not a problem with the tidal debris theory, but a comparison between cluster ellipticals and field ellipticals gives little indication that the cluster ellipticals have halos that have been tidally truncated (Oemler, 1992).

The primordial origin theory proposed by Merritt (1984, 1985) avoids these problems. This theory assumes that *all* galaxies initially had large dark matter halos and that these were subsequently removed by the mean cluster tidal field during the initial cluster collapse. However, the central galaxy retains its own primordial envelope because of its fortuitous location at the bottom of the cluster potential well, and furthermore inherits the halo remnants of the other galaxies. van den Bergh (1983) noted morphological similarities between cD galaxies and their parent clusters: they both tend to be flattened, and furthermore have aligned principal axes, which suggests that the cD and the cluster formed simultaneously.

Cooling flows have also been invoked to explain the formation of cD galaxies (Fabian et al., 1984). Hot x-ray gas decreases in pressure from radiative cooling, and subsequently settles to the centre of the cluster potential. As the gas cools and condenses, star formation may begin once densities are high enough. A mass deposition rate of 10 to $100 M_{\odot} \mathrm{yr}^{-1}$ would build a cD galaxy in a Hubble time (Dressler, 1984). Indeed, cooling flows of between $20 M_{\odot} \mathrm{yr}^{-1}$ and $100 M_{\odot} \mathrm{yr}^{-1}$ have been observed in some of the poor clusters studied in this thesis (McNamara and O'Connell, 1992; Neumann and Böhringer, 1995). Canizares et al. (1993) noted that cooling and accretion of intracluster gas onto the dominant galaxy is a widespread phenomenon in

poor clusters.

Central to all of the cD formation theories is the role of the cluster environment. Hence it is important to determine what the differences are between the cDs in rich clusters and the BCGs — the candidate cDs — of the poor clusters examined in this thesis. It is widely believed that rich clusters most likely formed from the conglomeration of several small clusters. Merritt (1985) has argued that they are the most likely sites of cD formation, since smaller clusters are more compact and have smaller velocity dispersions ($\sigma_v \leq 500$ km s^{-1}) than do rich clusters ($\sigma_v \geq 1000$ km s^{-1}), and therefore are more condusive to galactic mergers and stripping. This model predicts that the properties of a cD galaxy should only be associated with its initial environment, the poor cluster, and not the rich cluster that forms afterward. Contrary to this, Schombert (1988) found that the luminosity of cD envelopes is related to the cluster richness, in agreement with the stripping models of Malumuth and Richstone (1984). Also, a correlation between cluster x-ray luminosity and cluster richness class have been found (Edge, 1991).

Around the time of their discovery, cD galaxies were known to reside only in rich clusters containing hundreds of galaxies, which lead Morgan, Kayser, and White (1975, MKW) and later Albert, White, and Morgan (1977, AWM) to search for candidate cD galaxies located in clusters poorer than those in the Abell catalogue. They searched the Palomar Observatory Sky Survey and found several clusterings of a few galaxies possibly containing a cD (Table 1). The size of these galaxies on the pho-

tographic plates is, however, very small (less than 0.5 cm) which makes classification quite difficult. Larger images of the galaxies would be needed to determine if these galaxies were true cDs.

Previous surface photometry studies of the AWM and MKW clusters have been mainly photographic. Thuan and Romanishin (1981, TR) did photographic surface photometry on nine of the poor cluster BCGs, and found no evidence for diffuse envelopes which are characteristic of cD galaxies in rich clusters, while Morbey and Morris (1983, MM) found some evidence of diffuse envelopes in their photographic study. Photographic plates, however, suffer from non-linearities at faint light levels which obviously affect the profiles where we are most interested.

Accurate sky determination is crucial for accurate photometry at faint levels, and it is therefore desirable to have images that cover an area large enough that the BGC light does not contaminate the entire frame. Malumuth and Kirshner (1985, MK) did CCD surface photometry of some poor cluster BCGs, but their spatial coverage was poor. A significant improvement in spatial coverage was made in this study, by mosaicking images centred and offset from the dominant galaxy.

Our principal objective for this project was to measure surface brightness profiles accurately using CCD images of poor cluster BCGs to determine definitively if they are indeed genuine cD galaxies. Therefore, we are primarily interested in detecting possible envelopes around the MKW and AWM BCGs.

Table 1: POOR CLUSTER LOCATIONS (b1950.0) AND MAGNITUDES

Cluster	α	δ	z	M	Dominant galaxy
MKW 1	09 58 22	−02 43 48	0.0207	14.2	NGC 3090
MKW 2	10 25 36	−03 02 24	0.0377	14.4	10276−0255
MKW 3	11 46 54	−03 11 00	0.0271	14.9	11469−0311
MKW 4	12 01 52.8	+02 10 30	0.0204	13.8	NGC 4073
MKW 5	13 58 00	−02 37 00	0.0249	14.5	NGC 5400
MKW 6	14 15 06	+02 16 00	0.0256	15.3	14151+0216
MKW 7	14 31 30	+04 00 00	0.0289	15.0	14315+0500
MKW 8	14 38 12	+03 40 00	0.0272	14.7	NGC 5718
MKW 9	15 30 00	+04 51 00	0.0397	15.3	15300+0451
MKW 10	11 39 48.9	+10 32 30	0.0205	13.8	NGC 3825
MKW 11	13 26 54	+12 00 00	0.0220	14.7	NGC 5171
MKW 12	14 00 28.4	+09 39 38	0.0190	14.3	NGC 5724
MKW 1S	09 17 30	+01 15 00	0.0172	14.1	09175+0115
MKW 2S	10 24 36	−03 04 00	0.0381	15.2	10246−0304
MKW 3S	15 19 25.3	+07 53 13	0.0450	15.5	NGC 5920
MKW 4S	12 04 05.3	+28 27 13	0.0283	13.7	NGC 4104
AWM 1	09 13 59.7	+20 24 30	0.0293	14.0	NGC 2804
AWM 2	12 13 06.2	+24 15 38	0.0218	14.3	NGC 4213
AWM 3	14 26 02.2	+26 04 18	0.0150	14.2	NGC 5629
AWM 4	16 02 49	+24 04 03	0.0322	14.9	NGC 6051
AWM 5	16 55 58.4	+27 55 46	0.0345	14.4	NGC 6269
AWM 6	12 58 48	+40 07 00	0.0356	15.0	IC 4062
AWM 7	02 51 13.3	+41 22 37	0.0172	14.6	NGC 1129

2 Observations

Images were acquired by Dr. Terry Bridges from April 25 to April 30, 1995, using the Jacobus Kapteyn Telescope (hereafter JKT) in La Palma, Canary Islands, Spain. The JKT has a $1.0m$ diameter parabolic primary mirror with a focal ratio of $f/4.6$. The telescope can be used in two different Cassegrain optical configurations by interchanging secondary mirrors. The most common configuration, and the one used here, uses a hyperbolic secondary mirror that yields a conventional Cassegrain optical system with a focal ratio of $f/15.0$.

The TEK4 CCD chip employed has an array of 1124×1124 pixels that are $0.24 \times 10^{-4}m$ square. The scale is $0''.33$ per pixel, so the chip covers a patch of sky $6'.2 \times 6'.2$ in size. The read noise of the TEK4 chip was $4.7e^-$, and the gain was set to $0.75e^-/\mathrm{ADU}$ (electrons per analogue to digital units). The regime of nonlinearity was reached around 60000 ADU. The chip has a negligible amount of dark current, hence dark frame calibration was unnecessary.

For each galaxy, a series of images (usually in two filters, B and R) was taken of three different areas. The halo light from a large galaxy could extend over a the entire CCD chip, and to compute an accurate sky value, the galaxy must not contaminate the sky measurements. Therefore, it was desired to trace the halo profile continuously over a radial distance large enough that the profile slope becomes flat, indicating that the sky intensity has been reached. To obtain a large enough image, a mosaic was taken: one set of exposures was centred on the galaxy (galaxy frame), and another

Table 2: NUMBER OF EXPOSURES OF PROGRAM OBJECTS

Frame	galaxy				overlap				offset			
Exposure	60s		900s	600s	60s		900s	600s	60s		900s	600s
Filter	*B*	*R*	*B*	*R*	*B*	*R*	*B*	*R*	*B*	*R*	*B*	*R*
Cluster												
MKW 2	1	1	5	5	1		2	3	1		2	2
MKW 2S	1	1	5	5		2	3	3			4	4
MKW 3S	1	1	5	5	1	1	3	3	1		2	2
MKW 4	1	1	5	5	1	1	3	3	1		2	2
MKW 5	1		5		1		2				2	
AWM 4	1		5				3				2	
AWM 5	1	1	5	5	1		3	3	1		2	2
Abell 2052	1	1	5	5		1	3	3		1	2	2

set was shifted 4′ east of the galaxy centre (overlap frame). These frames shared a common overlap region of about 1′ that was used to bring the galaxy and overlap frames into registration. In order to create a dark sky flatfield, a third set of exposures were taken of an area offset approximately 30′ away from the galaxy (offset frame). In most cases, five galaxy frames, three overlap frames, and two offset sky frames were obtained (table 2). The galaxy and overlap frames were dithered by 20″, and the offset sky frames were dithered by 30″.

In order to calibrate the surface photometry, photometric standards measured by Landolt (1992), were observed at the beginning, middle, and end of each night. The seeing varied over the course of the observing session; the full width at half maximum (FWHM) of stars ranged from $\approx 1\farcs6$ (in B) on the first four nights, then degraded to $\approx 2\farcs1$ on the last two nights. The last night of the seven awarded was cloudy, and no data were obtained.

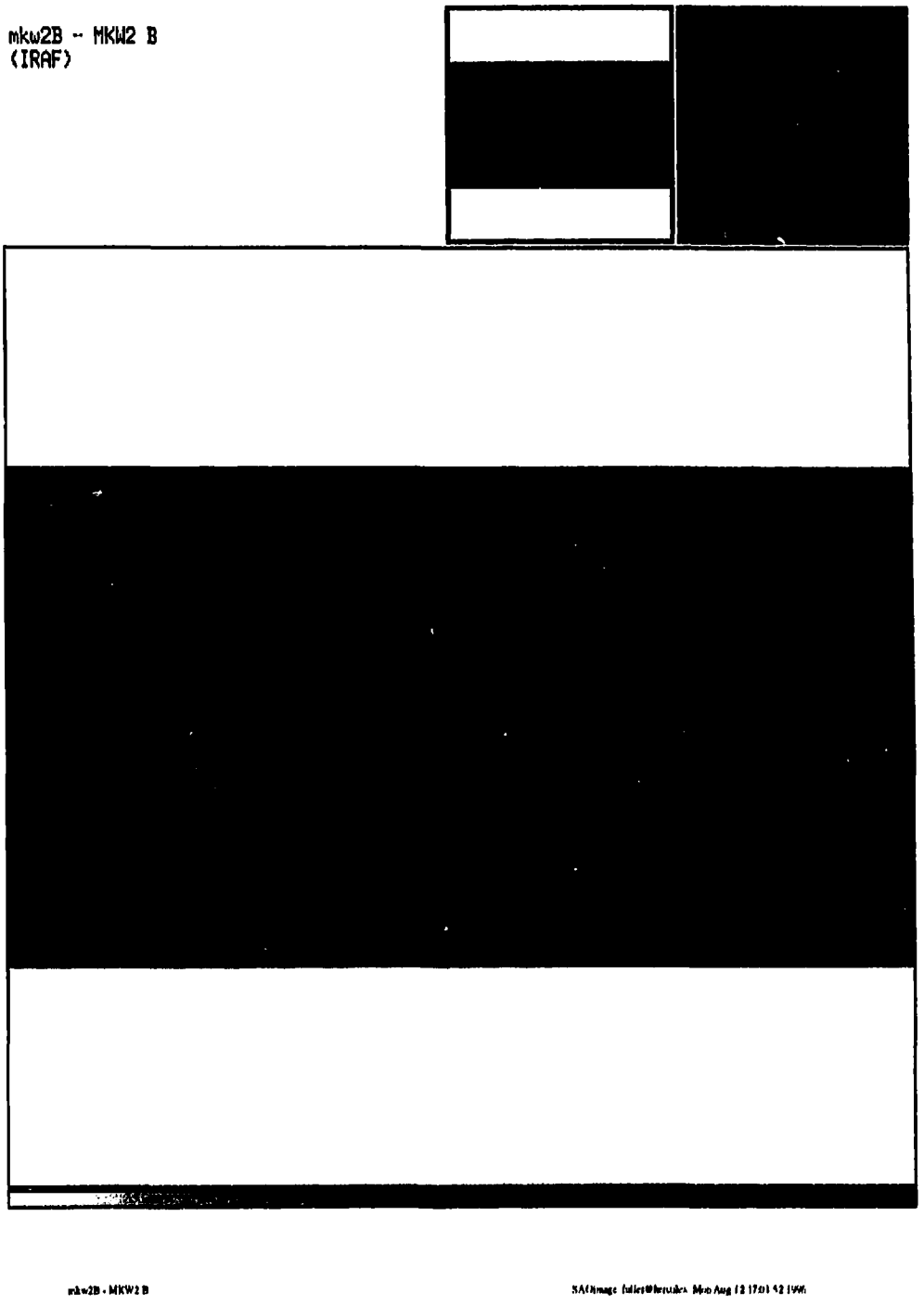

Figure 1: B image of 10276 − 0255, the BCG of MKW 2.

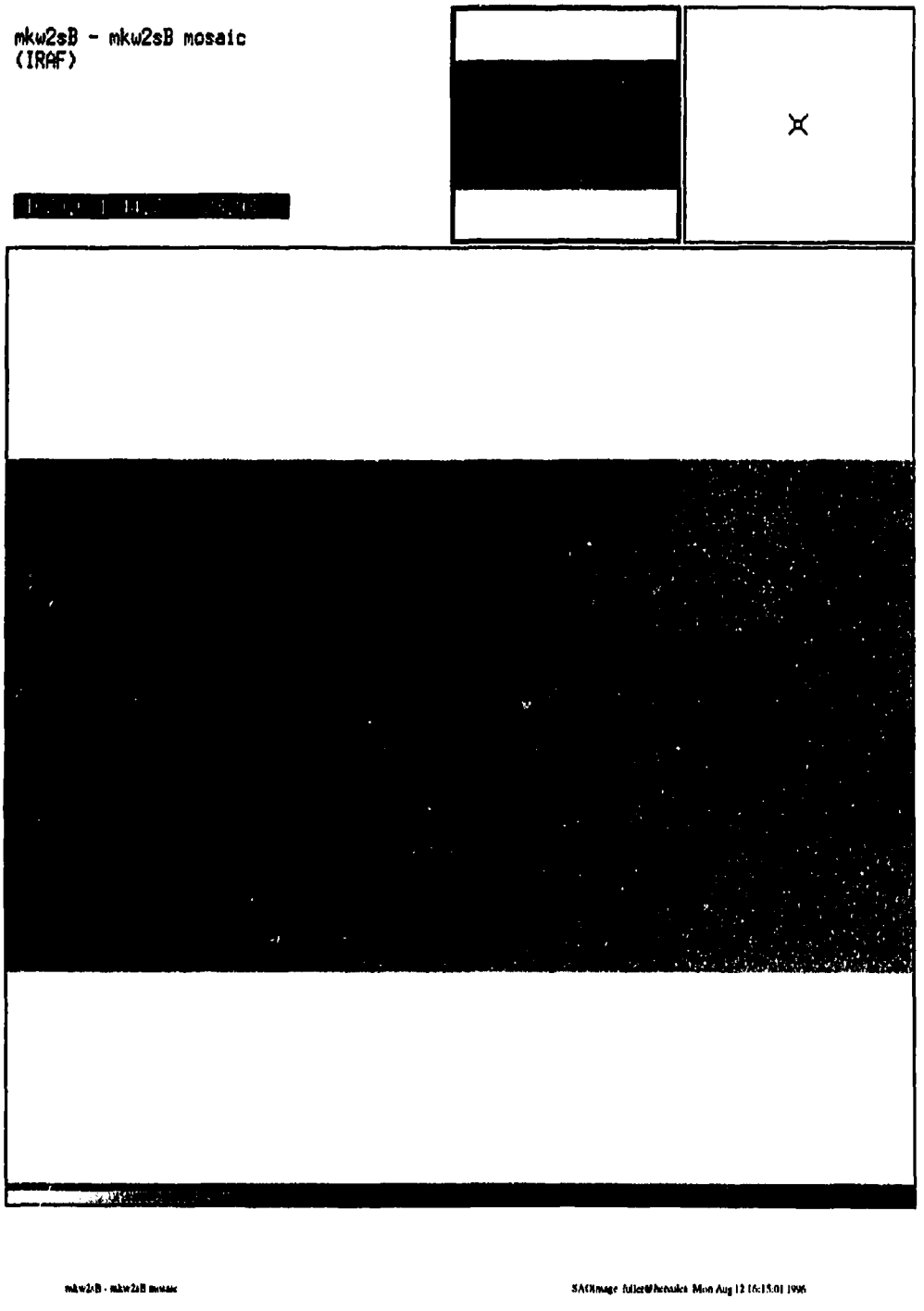

Figure 2: B image of 10246 – 0304, the BCG of MKW 2S.

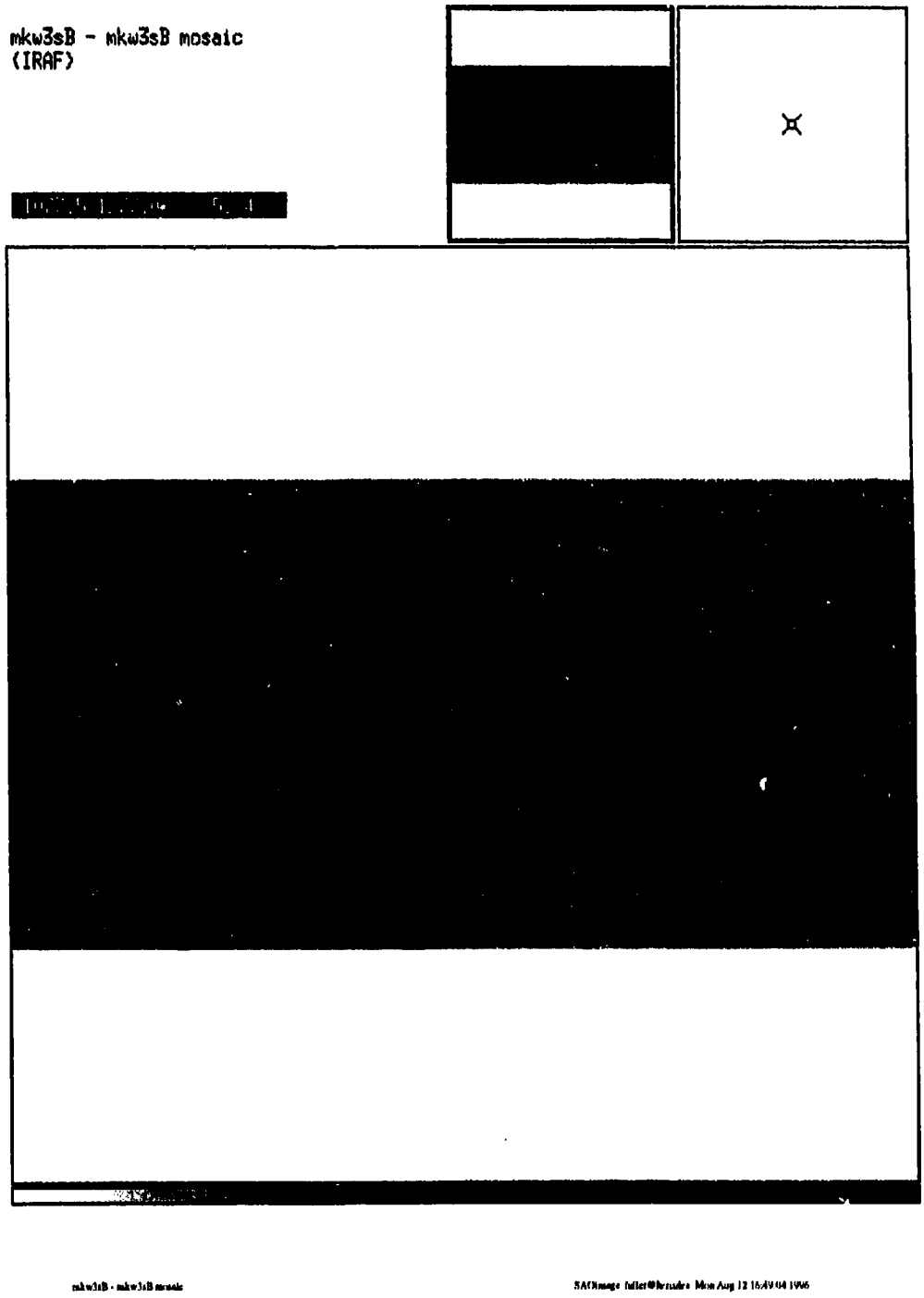

Figure 3: B image of NGC 5920, the BCG of MKW 3S.

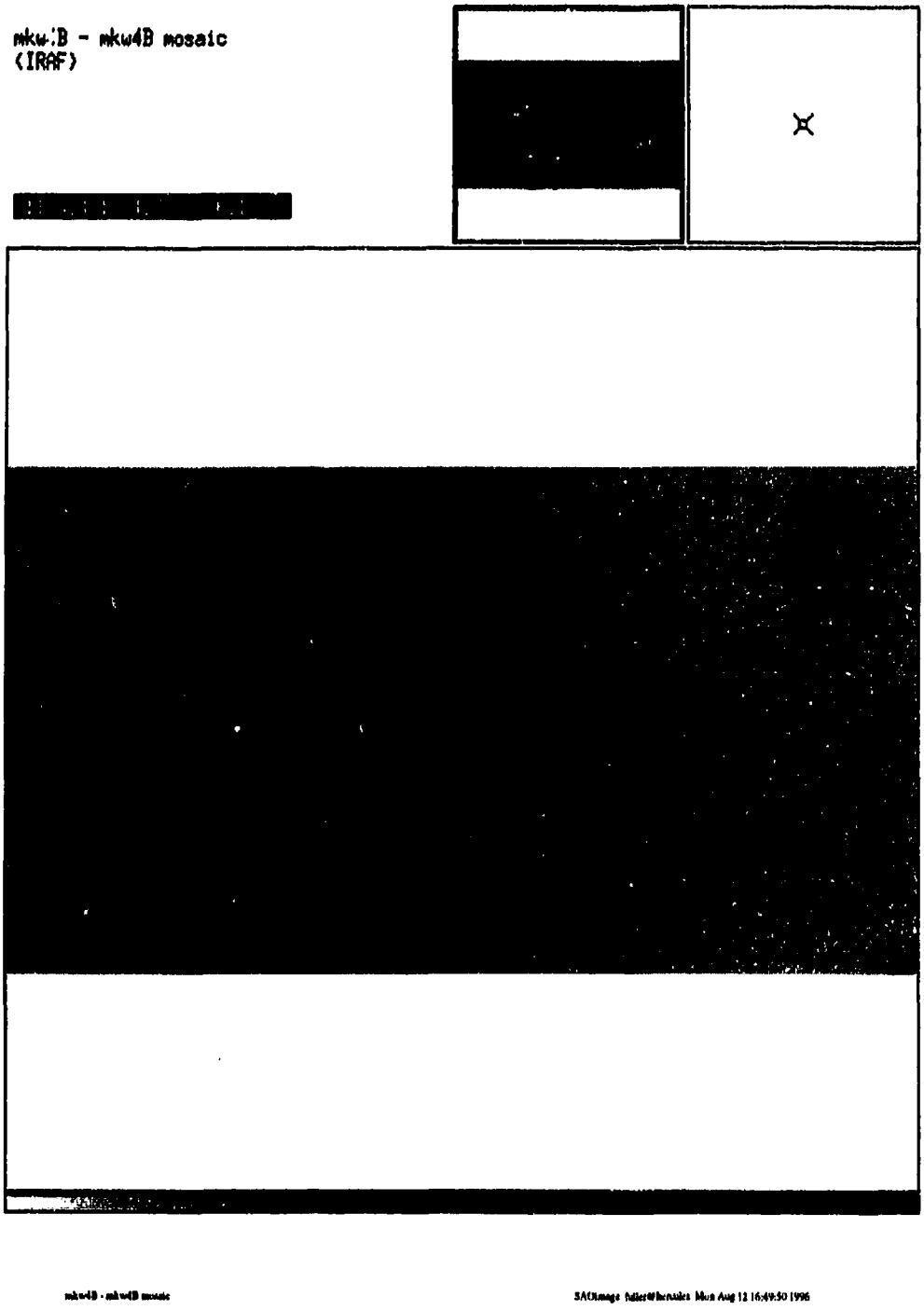

Figure 4: B image of NGC 4073, the BCG of MKW 4.

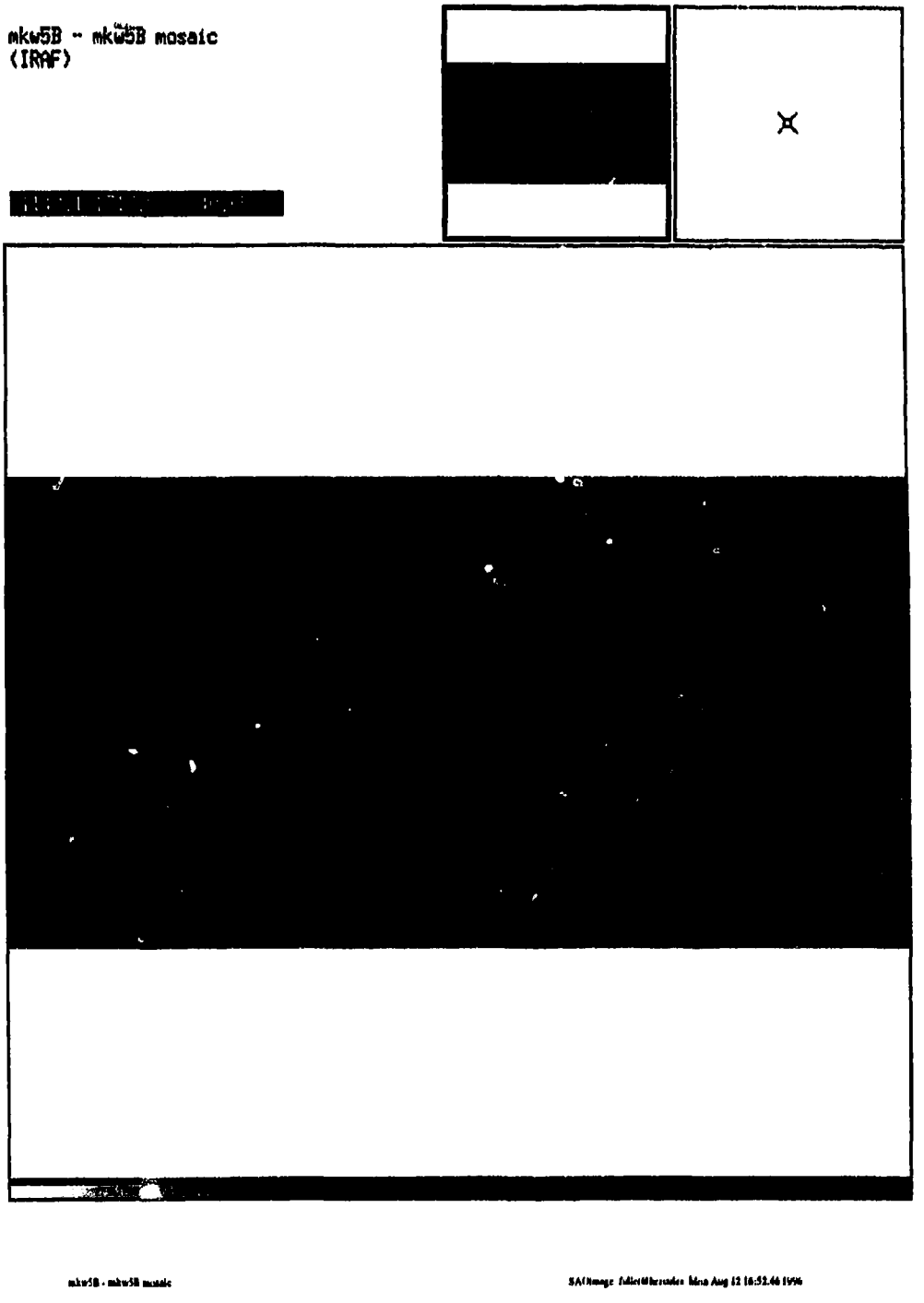

Figure 5: B image of NGC 5400, the BCG of MKW 5.

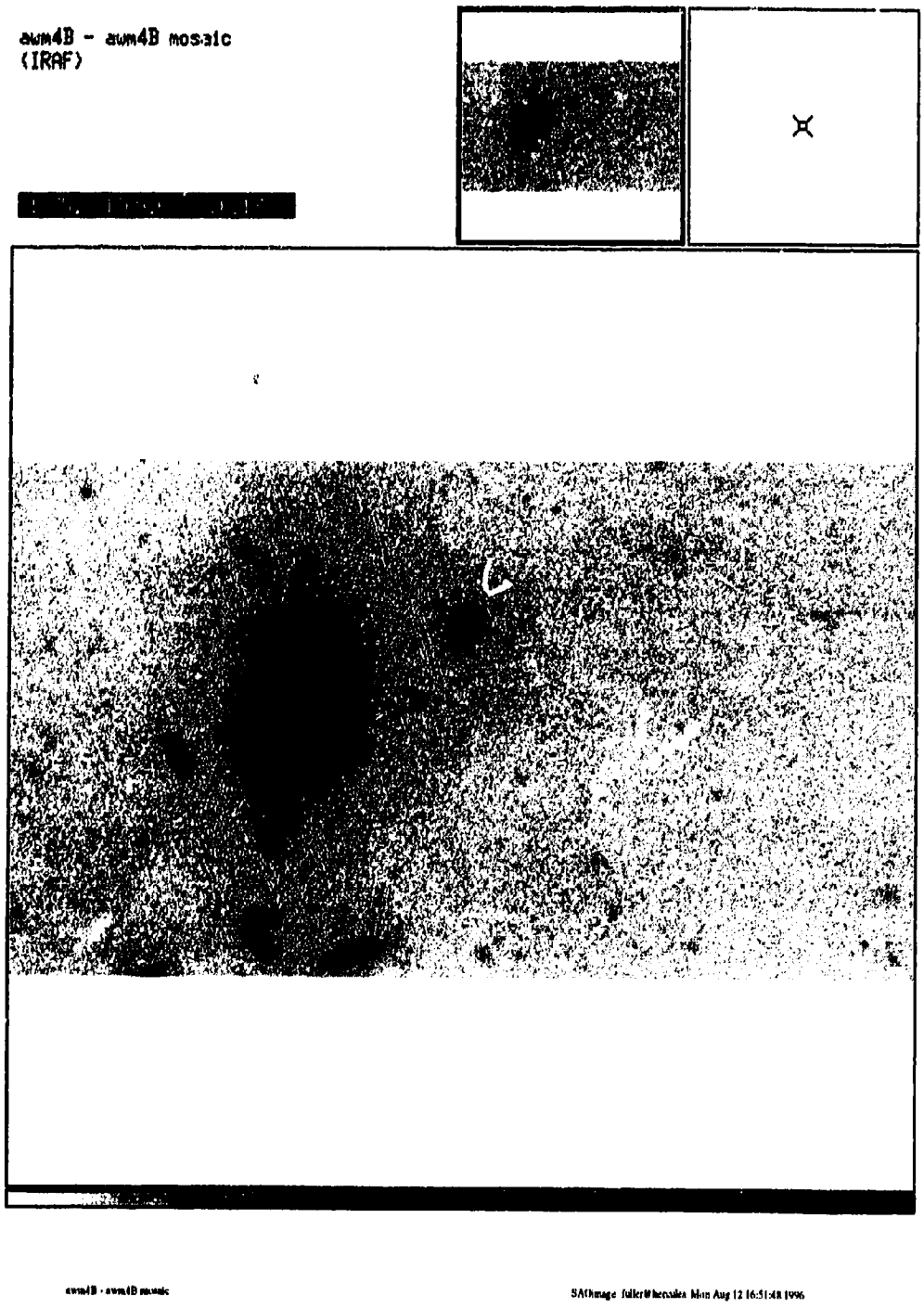

Figure 6: *B* image of NGC 6051, the BCG of AWM 4.

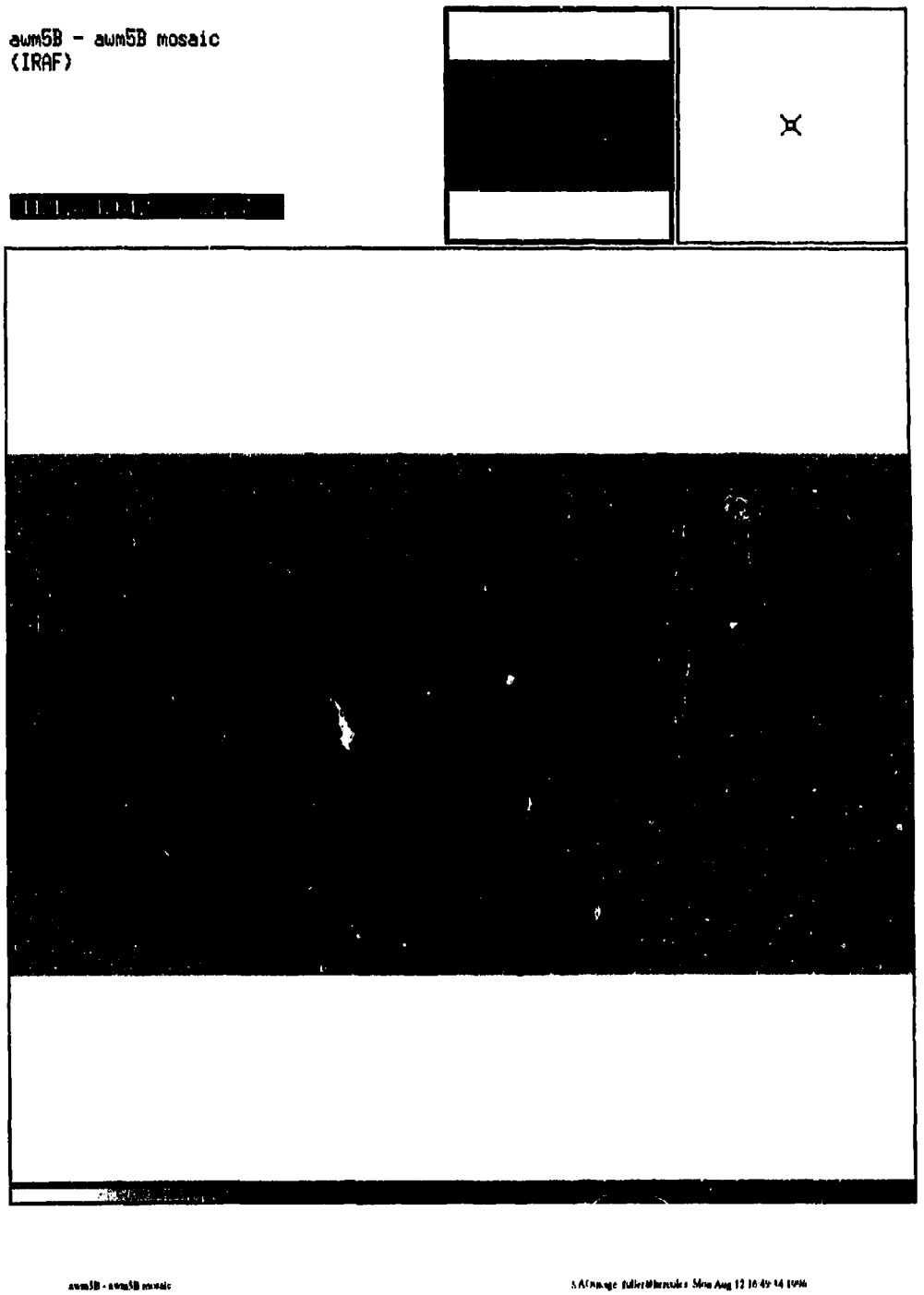

Figure 7: B image of NGC 6269, the BCG of AWM 5.

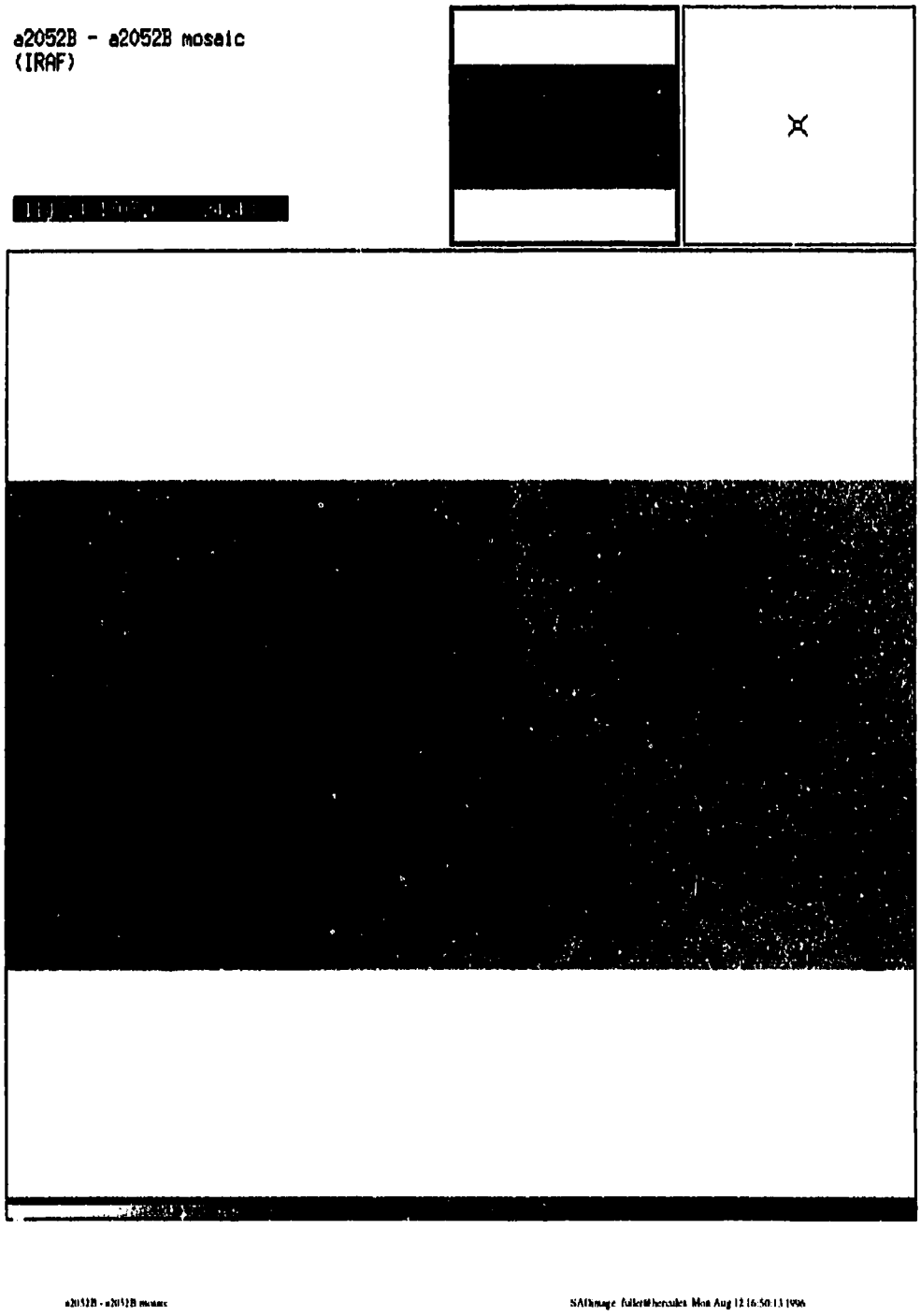

Figure 8: B image of UGC 09799, the BCG of Abell 2052.

3 Image reduction

3.1 Overscan subtraction

CCD frames are "biased" by adding an electronic pedestal level of several hundred ADU (analogue/digital units). This bias level must be subtracted from each image individually since it varies with many factors such as temperature. The bias level is usually a slight function of position on the chip; normally, a zeroth or first order function (i. e., a constant value or straight line) is fit to the overscan region[1] of the chip and subtracted from the image. This is ordinarily a very simple process, but was complicated in this case since some of the images suffered from an unstable bias level (figs. 9, 10), the cause of which is unknown.

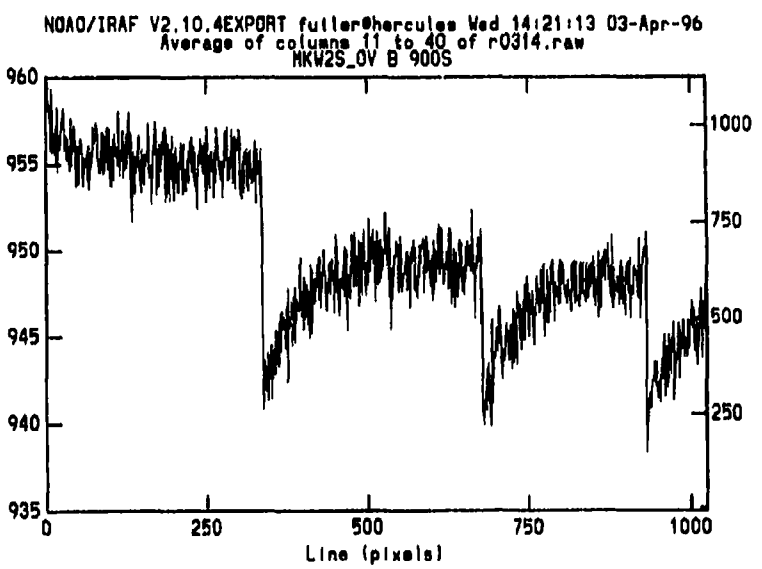

Figure 9: Intensity versus line for an unstable bias

[1]defined in glossary

The discontinuities were removed from the overscan region by the following procedure. First, the IRAF task **blkavg**[2] was run on the overscan region, which averaged the pixel intensities along a line of the CCD, and produced a one dimensional image having the same number of columns as the overscan region, but only one line. Next, the locations of the discontinuities were accurately determined, and the task `fit1d` fitted a user specified function, such as a Chebychev polynomial or a cubic spline, to the regions between the discontinuities. The user may also specify the order of the function, or the number of spline pieces for a cubic spline fit. Figure 11 shows a cubic spline fit to an overscan region that has three discontinuities.

A two-piece cubic spline was fit to the overscan for all of the images, because it produced a reasonable fit to overscan regions that had and did not have discontinuities. Other functions could be made to fit the overscan regions containing discontinuities well, but did not fit non-defective overscan regions as well as the cubic spline. After the function was fit to the overscan region, a two dimensional image was created from the one dimensional fit by using **blkrep**. Lastly, this image was subtracted from the original image (Figure 12). After this correction was performed, in most cases it was impossible to tell that there had ever been a problem with the image, while in the few remaining cases, it was still difficult to see any residual imperfections.

It is standard practice to take a series of bias frames each night during an observing run, then combine them and subtract the combined bias frame from program frames.

[2]IRAF tasks are printed in the `typewriter` font

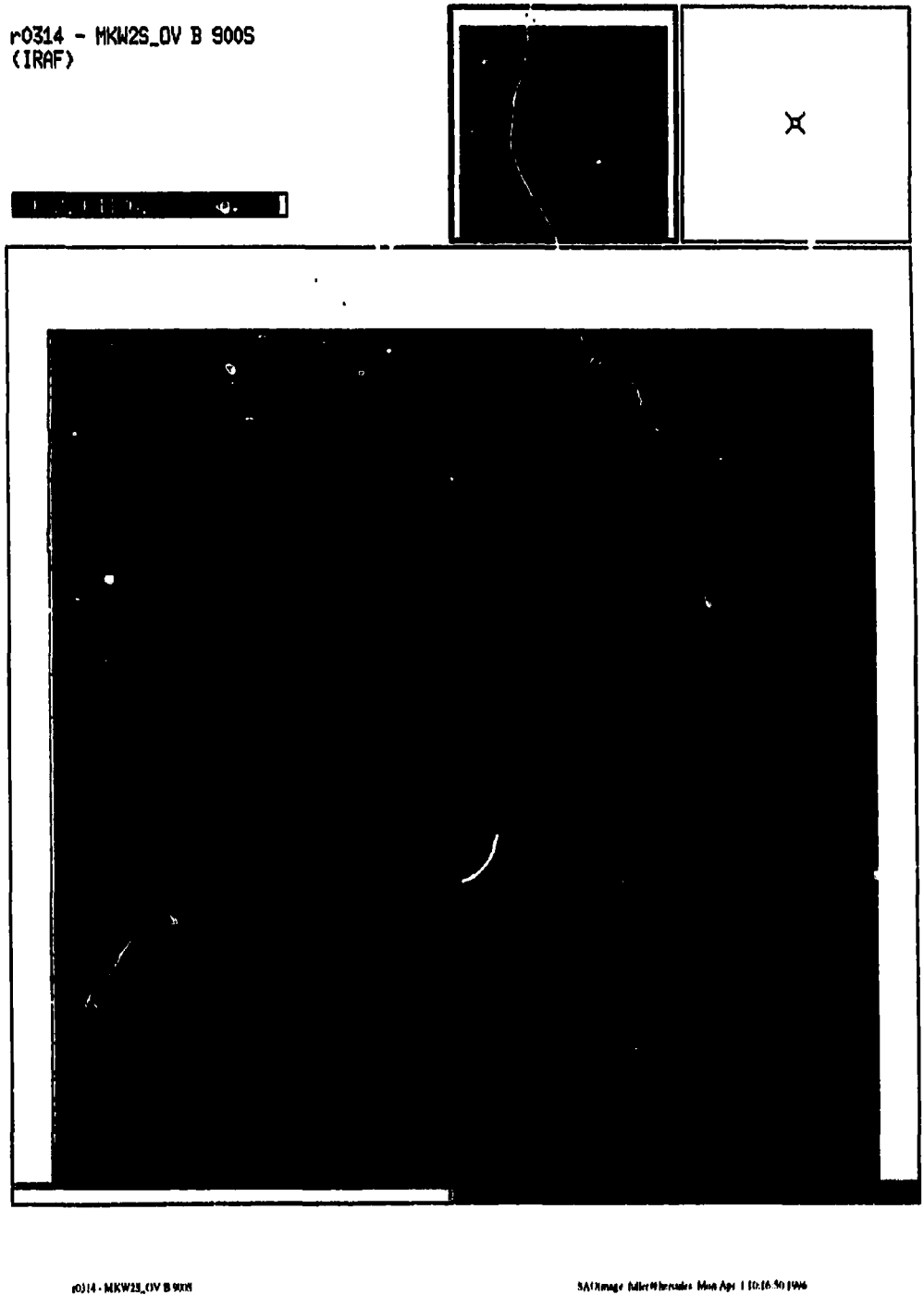

Figure 10: A raw image with an unstable bias region.

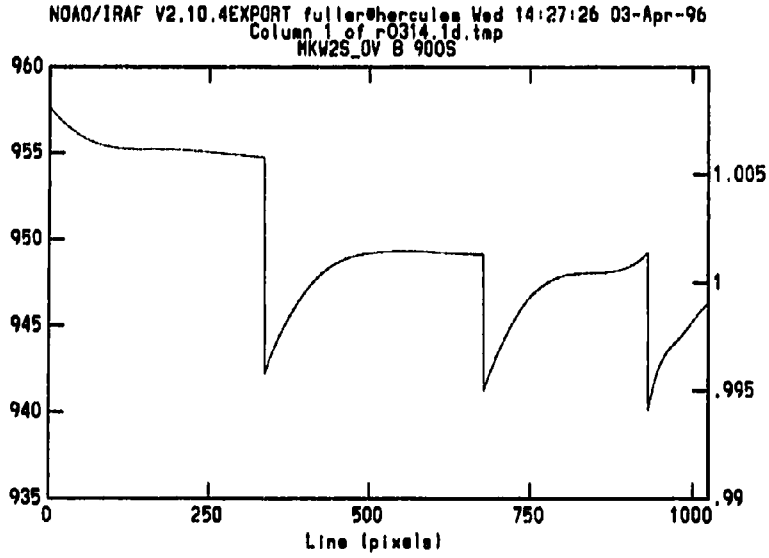

Figure 11: A two piece cubic spline fit to an overscan region containing three discontinuities.

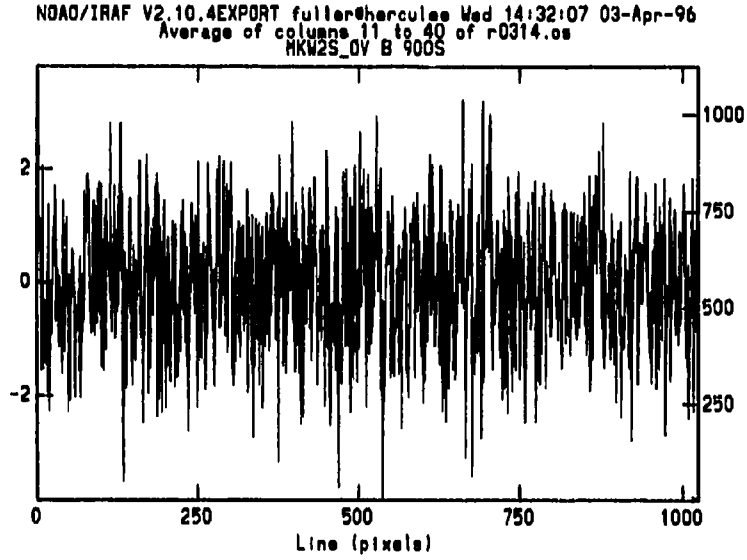

Figure 12: Overscan region after a two piece cubic spline subtraction.

This is necessary if the CCD chip displays any bias structure. As mentioned above, a zeroth or first order function is normally fit to the overscan region and subtracted, which removes the bias pedestal. The combined bias frame is then subtracted from the program image, which removes any bias structure. In this case, a high order function was fit and subtracted from the program frame, thus removing any structure in the y direction, so bias frame subtraction was not necessary, since the structure in the x direction was small and unimportant. Since the bias structure was not consistent from frame to frame, bias frame subtraction was pointless. The bias frames show almost no structure (Figure 13): there is only a small, insignificant gradient of less than one ADU across the CCD chip lines, and no noticeable gradient across the columns. For images with a smooth overscan region, bias frame subtraction is not necessary. Indeed, when the CCD chip is functioning properly, bias frame subtraction is not usually necessary (T. Bridges, private communication).

3.2 Flat fielding

Twilight flats were obtained in the evening or morning or both of each night, and combined using `flatcombine` to produce one twilight flat in B and one in R for each of the six nights. Pixel intensities for the combined image were computed using the median intensity of the combined images. Each flat was multiplicatively scaled by the mode of the pixel intensities to compensate for different exposure times, and a zero point offset was computed using the mode of the pixel intensities to compensate

for different twilight sky brightness levels. Pixel rejection was performed using the `ccdclip` rejection scheme, which determines what pixels should be excluded, based on the readnoise and gain of the CCD chip.

After an image of a blank part of the sky has been flat fielded, there still may be residual large scale gradients across the image. This can be caused by non uniform illumination of the detector when the flat field exposures are obtained. The difference between a flattened blank sky image and the actual blank sky is called the illumination pattern, and to correct for this difference, blank sky exposures are taken and flattened using the twilight flats. Any objects in these images are removed by a sigma clipping algorithm. Also, since the blank sky exposures were dithered, objects are also removed when they are median combined. Since the purpose of the blank sky images is to reduce the large scale gradients, they are heavily smoothed using a two dimensional moving boxcar algorithm. Next, they are normalized by the mean intensity and divided into the original flat field image which yields the blank sky flat. The production of the blank sky flat is performed by `mkskycor`, and once created, it is used to flatten all subsequent images.

Figures 14 and 15 show the gradients on a typical image before and after the flat fielding process. The residual gradients in the final images were always 1.0% of the sky or less; when flat fielding is done with both twilight flats and dark sky flats, gradients can be 0.5% or better (Mackie, 1992).

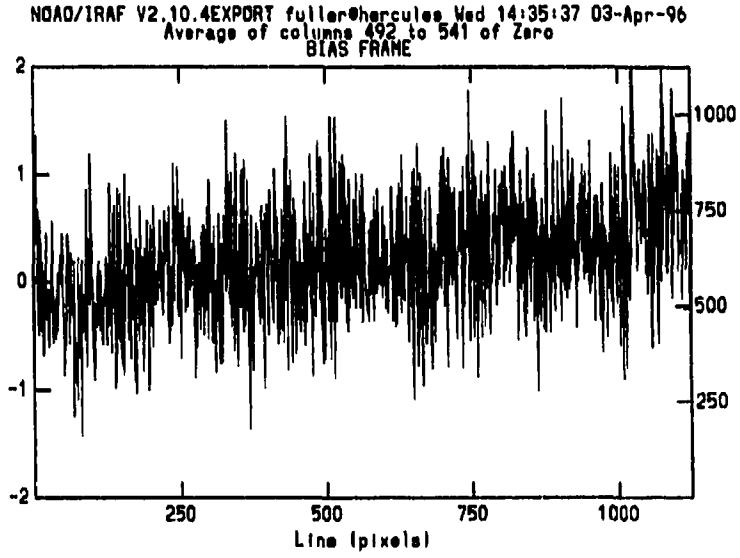

Figure 13: Bias frame, column plot

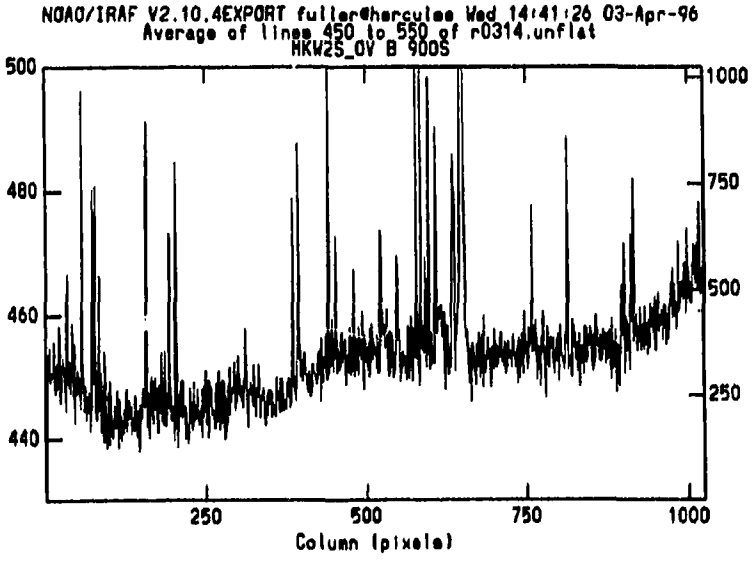

Figure 14: Unflattened image, line plot

3.3 Mosaicking images

The galaxy centred and overlapping frames were combined by `imcombine`, using the median pixel intensity. No scaling was done, since the exposures were all of identical time, but a zero point offset was performed to adjust for varying sky brightnesses.

The galaxy and overlap frames were taken such that there were a few stars common to both images. The shifts needed to align images were computed by `xregister`, and have sub-pixel accuracy. `IRAF` contains no procedure to mosaic images, but it does have the necessary tools. To mosaic two images, first a blank image was created that was large enough to contain both images. Next, the overlap frame was copied into the blank image, and shifted by the amount computed by `xregister`. The galaxy frame was then copied into the large image, finishing the process.

After the galaxy and overlap frames were mosaicked, the background sky levels had to be brought to the same level. This was done by computing the median intensity level in the region common to both frames. Image statistics on pixels that fall between a lower and upper threshold can be computed with `imstatistics`. Specifying these thresholds allows objects (e. g., stars, galaxies or other hot pixels) to be excluded from the computations.

An iterative procedure was developed using `imstatistics` to determine the median sky intensity for the overlapping region. On the first iteration, `imstatistics` was run using no lower or upper clipping threshold to compute the median and standard deviation, and for subsequent iterations, the upper and lower clipping thresh-

olds were set at the median intensity $\pm 1\sigma$ returned from the previous iteration. (A clipping threshold of $\pm 2\sigma$ was used for comparison, and the results were almost identical.) This procedure was done for ten iterations in total. The data points in Figure 16 show the median intensity change with iteration, averaged over all images. The median value converged quite rapidly in the first few iterations, and after iteration six there was little change. The intensity difference between the regions common to galaxy and overlap images was added to the overlap image using `imarith`.

All images were visually inspected after the automated process described above was completed. In some cases, the above procedure was not quite satisfactory, and small adjustments (i. e., $\leq$ two ADUs) were necessary. This occurred in frames where the light from the BCG was quite bright in the region common to the galaxy and overlap frame, and subsequently the median intensity in the overlap region was not accurately determined. For most of the images, the automated process was completely adequate, and it was difficult to determine where the seam was between the mosaicked images. In the worst case, there was less than a 1% difference in intensities across the seam. This was undoubtedly a manifestation of the 1% flat fielding; any seam would be limited by the flatness of the images mosaicked.

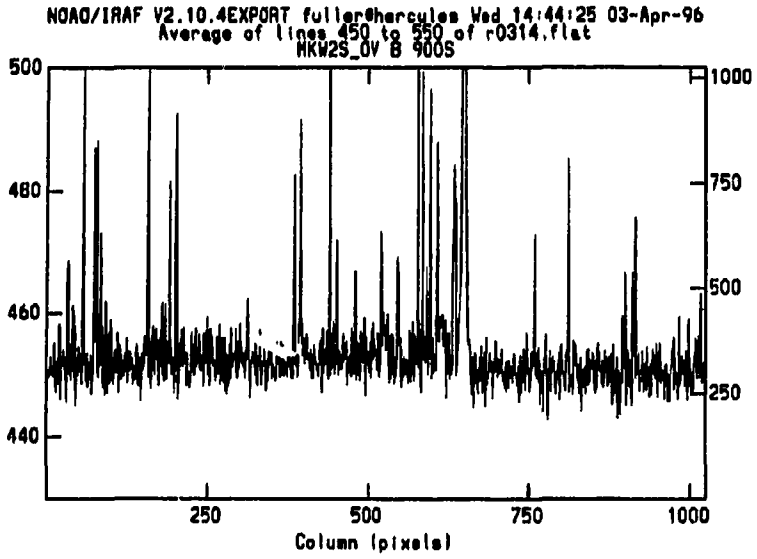

Figure 15: Flattened image, line plot

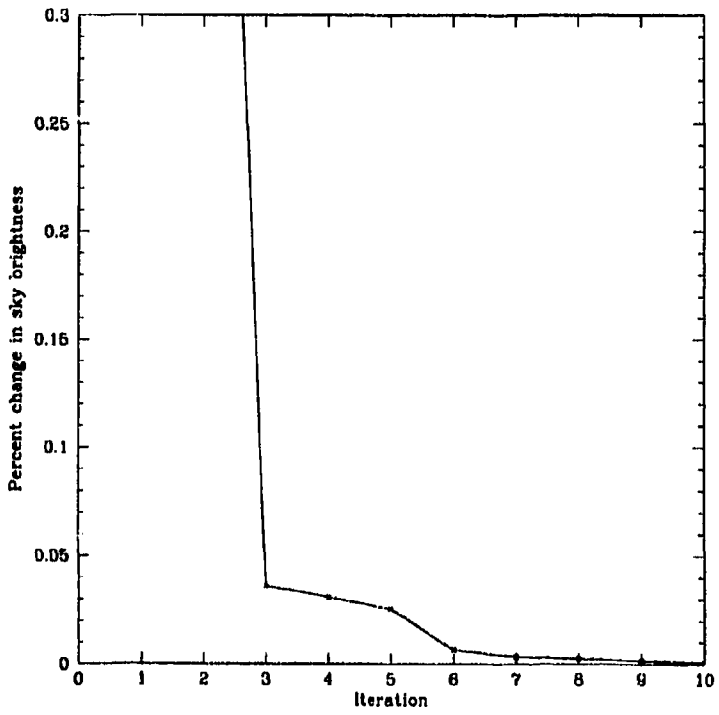

Figure 16: Mean change in median intensity vs. iteration

4 Surface photometry

Surface photometry is the measurement of the brightness profile of an object, usually a galaxy. This is accomplished by fitting elliptical annuli to the object, then summing the pixel intensities inside the annuli. The five parameters needed to completely describe an ellipse are the position angle of the elliptical annulus, the ellipticity (defined as $\frac{a-b}{a}$ where a and b are the ellipse semi-major and semi-minor axes), the x and y coordinates of the ellipse centre, and the length of the semi-major axis.

The `STSDAS` task `ellipse` uses an iterative method described by Jedrzejewski (1987). The following brief discussion of the `ellipse` algorithm was taken from the `IRAF` help pages; the interested reader is directed there for a complete discussion of the method. The user supplies initial guesses for the five ellipse parameters, the routine samples the image along the supplied elliptical path and produces a one dimensional intensity distribution as a function of the ellipse eccentric anomaly, E. The Fourier harmonics of the distribution are fit by least-squares to the function

$$y = y_0 + A_1 \sin(E) + B_1 \cos(E) + A_2 \sin(2E) + B_2 \cos(2E) \qquad (1)$$

Next, the five ellipse parameters are adjusted by a correction found from the amplitudes A_1, B_1, A_2, and B_2. The parameter with the largest amplitude is varied, a new elliptical path is chosen, and the image is resampled. The task stops after a user specified number of iterations, or after the solution converged, and the best fitting ellipse is given by the parameters that produced the lowest absolute values of the harmonic amplitude.

The task starts with a user supplied initial semi-major axis, steps outward until a user supplied maximum semi-major axis is reached, then proceeds inward from the initial radius to a user supplied minimum axis. The user may select a linear increment or a geometric increment, in which the semi-major axis grows by a factor of $1 + stepsize$ or shrinks by a factor of $1/(1 + stepsize)$. A geometric increment is useful because the outer annuli will have a larger area, which helps to compensate for their diminished brightness.

Errors in intensity and magnitude are computed from the root mean squared scatter in the pixel intensities along the sampled elliptical annulus. The five ellipse parameters errors are computed by combining the residual scatter in the pixel intensities with the internal error in the harmonics.

4.1 Object removal

Surface photometry measurements are complicated by sources of light contamination, such as stars and both cluster and background galaxies. At faint brightnesses, such as in diffuse BCG envelopes, contamination becomes very important. Stellar halos and other cluster members affect the surface brightness profiles at the $0.1 - 0.5$ magnitude level at 25 mag arcsec^{-2} (Uson et al., 1991; Mackie, 1992). The contamination of course depends on the brightness and density of the offending objects. There is also contamination from the intracluster light, but this light is 0.01% to 0.1% of the sky intensity, hence contamination is dominated by cluster members and foreground stars.

King (1971) investigated the scattered light from bright stars, and found that the intensity profile in the high surface brightness region was described by exponential falloff, while an inverse square law fit the wings of the PSF (point spread function). This finding is instrumental in removing the contamination from bright stars, because both the core and halo of bright stars can be modeled simply.

There are many possible methods of dealing with cluster members and foreground stars. Objects may be removed from the image or they may be ignored by masking or other rejection schemes. A major benefit of removing objects from an image, instead of masking them out, is that a larger amount of data is used. However, the removal of objects is not a simple task. Extreme care must be taken when fitting a function to the object to be subtracted, because if any errors are committed, then object removal can be inferior to simply masking the object.

Mackie (1992) describes one method for removing small galaxies and foreground stars. He took slices of the radial brightness profiles that avoided the cores of the objects, and ignored any slices that showed possible contamination from other objects. A best fit r^{-2} halo profile was subtracted out to a radius where the intensity was a factor of ~ 1.2 times the sky intensity. After the object was subtracted, appropriate noise was added to the region from which the object was subtracted.

Masking objects is considerably simpler. Objects are identified either manually or by automatic means, such as the DAOPHOT routine `find`. Once that is done, a radius is determined where the intensity is close to the sky value, and all pixel

coordinates encircled by this radius are put into a file. The `ellipse` routine will read and ignore any pixels listed in the mask file. There is only one free parameter: the size of the truncation radius (which is also an issue when objects are subtracted).

Objects may also be removed by iterative $k\sigma$ clipping routines, similar to the method described in §3.3. Schemes such as this have been used by Schombert (1986) and Uson et al. (1991) to reject objects. Schombert (1986) states that such a procedure, because it uses information from the entire isophotal ellipse, is superior to cleaning algorithms that use only neighbouring pixels.

The surface photometry routine `ellipse` will clip up to the brightest 40% of the pixels in an isophotal annulus, and in some situations, pixel clipping can be a very simple yet effective way of removing contaminating objects. This method of pixel rejection may be used alone or in conjunction with pixel masking. For reasons discussed in §4.6, `ellipse` was only used to compute isophote parameters, and a new code that uses an iterative $k\sigma$ rejection scheme was written to compute the isophote intensity. Obviously, it is important to determine how well these rejection schemes work; therefore they were tested on artificial BCGs created using model profiles.

4.2 Creation of artificial images

To create a large artificial galaxy, `ellipse` was run on the dominant galaxy of AWM 5, since this galaxy fills a large portion of the frame, and `bmodel` was used to create a galaxy from the measured isophotes. The model galaxy was produced in this manner

(rather than randomly sampling some model luminosity profile) because it easily produces a realistic galaxy. It is a more arduous task to create from scratch a galaxy that has realistic features such as twisting isophotes. Also, the production of a luminosity profile similar to a poor cluster dominant galaxy is guaranteed.

After the model galaxy was created, stars, galaxies, and noise were added by the `artdat` routines, which generate artificial stars and galaxies of any size and brightness. A reference image was created by adding noise similar to the noise in real images to the model galaxy. The artificial images were constructed by adding a number of stars and galaxies, such that their density and distribution resembled the real images. To give the cluster galaxies a realistic distribution, a Hubble density law centred on the dominant galaxy was randomly sampled to assign spatial coordinates to the galaxies. The Hubble density law is defined as:

$$\Sigma(r) = \Sigma_0 \left(1 + \left(\frac{r}{r_c}\right)^2\right)^{-1} \tag{2}$$

where $\Sigma(r)$ is the projected surface density, r is the distance from the centre of the distribution, and r_c is the core radius. The luminosities were assigned by randomly sampling the Schechter luminosity function (Schechter, 1976) over a magnitude range similar to that observed on the real images. A few bright foreground stars and a large number of dim background stars were distributed randomly across the images; their luminosities were chosen from uniform random deviates scaled to values similar to objects observed in the real images.

4.3 Testing `ellipse`

Pixel clipping is an attractive method of removing light contamination, because of its ease of implementation — one merely has to specify to `ellipse` what percentage of the brightest pixels to clip (the clipping parameter). Since this is such a simple and quick method, its performance on object removal was immediately investigated. Only the effects of pixel clipping on the ellipse parameters will be investigated in this section, because as discussed in §4.6, a different code was used to compute isophote intensities.

Tests were done using clipping parameters between 0% and 40% (the range allowed by `ellipse`). Above about 15% clipping, parameters generated by `ellipse` did not change significantly. Figures 17 and 18 show the effect of clipping 40% of the brightest pixels on ellipticity and position angle. The largest allowable clipping parameter was used for these figures to demonstrate the performance of pixel clipping in the extreme case.

Figure 17 plots the ellipticity versus the position angle for the reference image and the artificial image with 40% of the brightest pixels clipped; the agreement is excellent. Figure 18 shows that the agreement between the reference image and the artificial image is also excellent for a 40% clipping parameter. For both the position angles and the ellipticities, there is a slight disagreement in the core regions below ≈ 5 pixels. A stellar FWHM of $1''.6$ corresponds to ≈ 5 pixels, and thus within this radius, the effects of seeing dominate: it tends to circularize features, which renders

the measurement of the ellipticity and position angle problematic. The effects of seeing are investigated further in §4.4.

Pixel clipping is a very useful tool in the cluster cores where the density of objects is high, and the ellipse parameters were always more accurate when pixel clipping was used. Even if there are no contaminating objects, however, pixel clipping has little effect on the parameters generated by `ellipse` — one would not expect the position angle, ellipticity or ellipse centre to change by ignoring the brightest pixels at a given isophote. To make certain that this was indeed the case, an artificial image was created that had very little contamination, therefore making it possible to clip too many pixels. As expected, the ellipticity and position angles of the artificial galaxy isophotes were consistent with the reference isophotes, even when the maximum number of pixels (40%) were clipped.

4.4 Errors incurred by seeing

To test the effect of seeing on the isophotal magnitudes, ellipticities and position angles, the artificial images were convolved with Gaussian functions of widths $1.2 \leq \sigma \leq 3.2$ pixels, which corresponds to FWHM values of $0\farcs9$ to $2\farcs5$ (FWHM $= 2.354\sigma$). Figures 19,20, and 21 were produced by comparing the reference image and a convolution of the artificial image with a gaussian of FWHM $= 1\farcs6$, typical of the observed stellar FWHM. Figure 19 shows the fairly dramatic effect that seeing has on magnitude: Gaussian smoothing efficiently reduces the core brightness, making the core

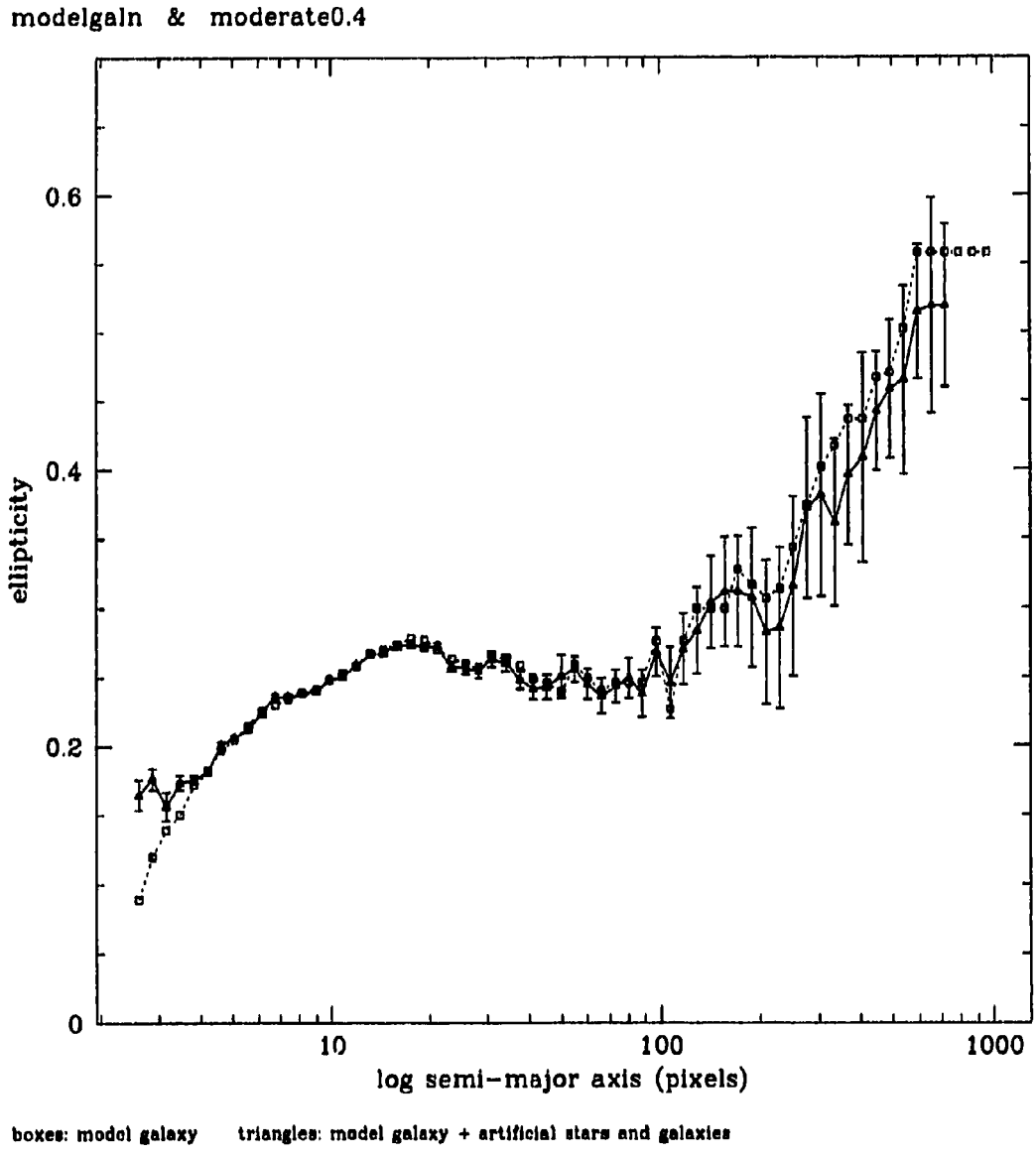

Figure 17: Isophote ellipticity plotted against the semi-major axis for the reference image [the model galaxy (boxes)], and the contaminated image [model galaxy + other stars and galaxies (triangles)]. The brightest 40% of the pixels were clipped.

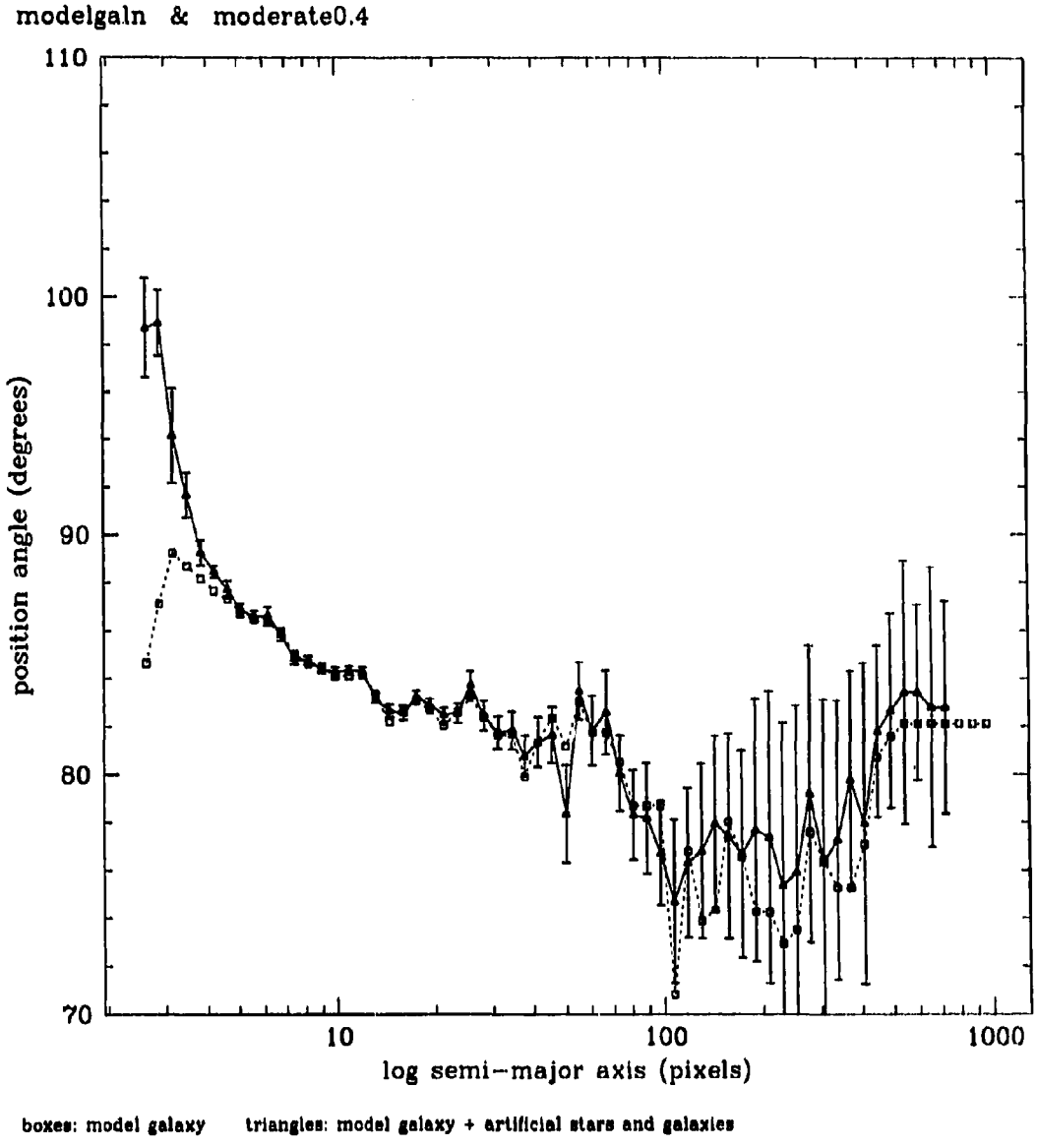

Figure 18: Isophote position angles plotted against the semi-major axis for the reference image [the model galaxy (boxes)], and the contaminated image [model galaxy + other stars and galaxies (triangles)]. The brightest 40% of the pixels were clipped.

of the reference image much brighter than the smoothed image. The large errors, however, are confined to the core; outside the core, seeing has little influence. Other simulations were done of poorer seeing conditions, and as expected the deviations steadily increase as the seeing degrades.

The effects of seeing on surface photometry have been investigated by many authors. In particular, the comprehensive study of Peletier et al. (1990) shows results similar to the ones discussed here. Also, Porter et al. (1991) found that ellipticities of galaxies are unaffected at radii larger than four or five times the FWHM of the seeing disk.

4.5 Errors incurred by sky subtraction

Accurate determination of the background sky intensity is vital for correct surface photometry, especially at the faint light levels of galaxy halos, which are marginally brighter than the sky. The effect that error in sky intensity measurement has on isophotal magnitude is analytically determined as follows. The instrumental magnitude is given by

$$m = m_0 - 2.5 \log(I - I_{bg}) \tag{3}$$

where I is a measured intensity, I_{bg} is the sky intensity, and m_0 is an arbitrary zero point. If an error (ϵ) is committed in the measurement of the sky intensity, the resulting instrumental magnitude will be

$$m' = m_0 - 2.5 \log\left(I - I_{bg}(1 + \epsilon)\right) \tag{4}$$

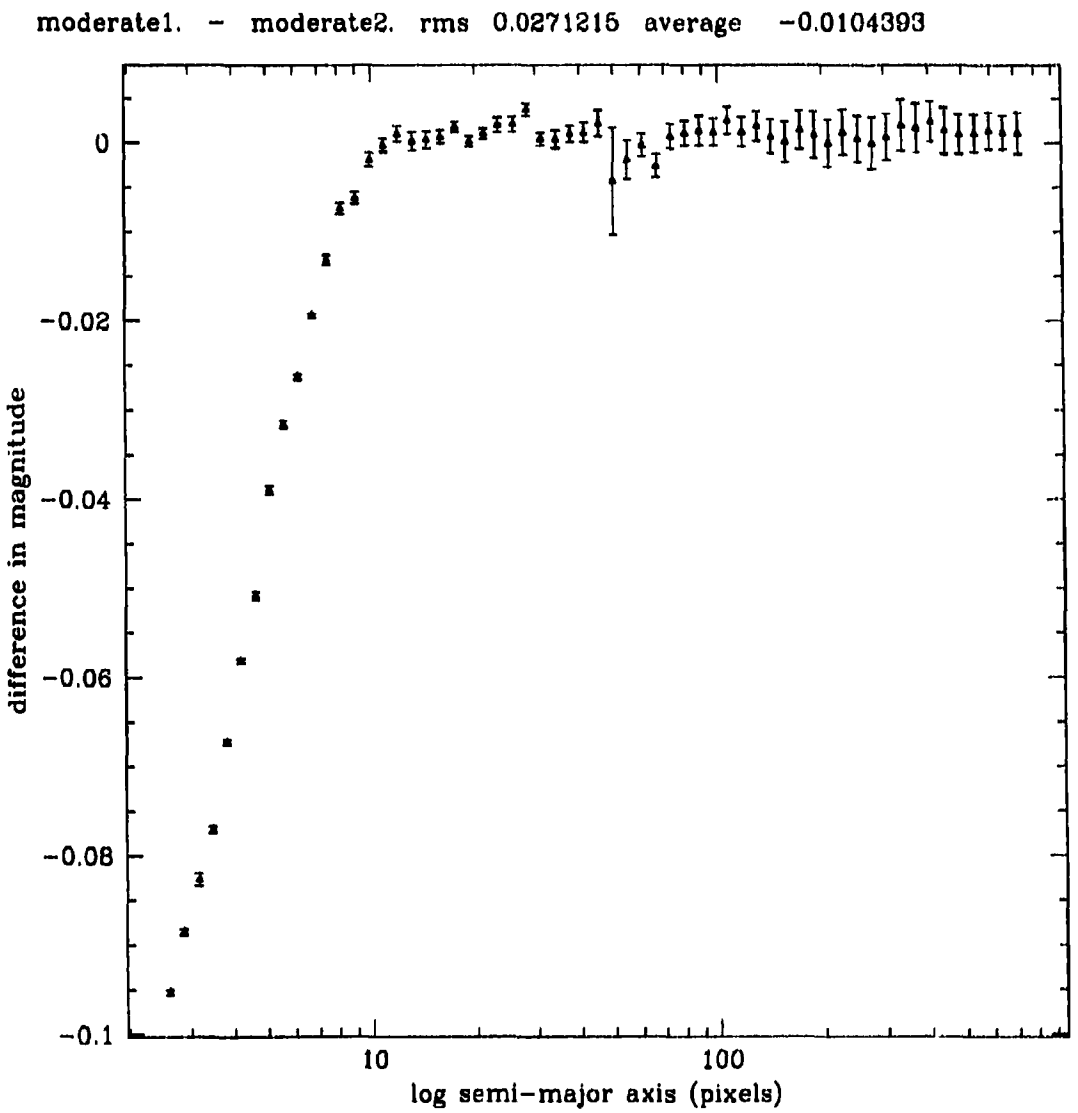

Figure 19: Isophotal magnitudes differences between the reference image and the artificial image convolved with a Gaussian of FWHM = 1″.6, as a function of the semi-major axis.

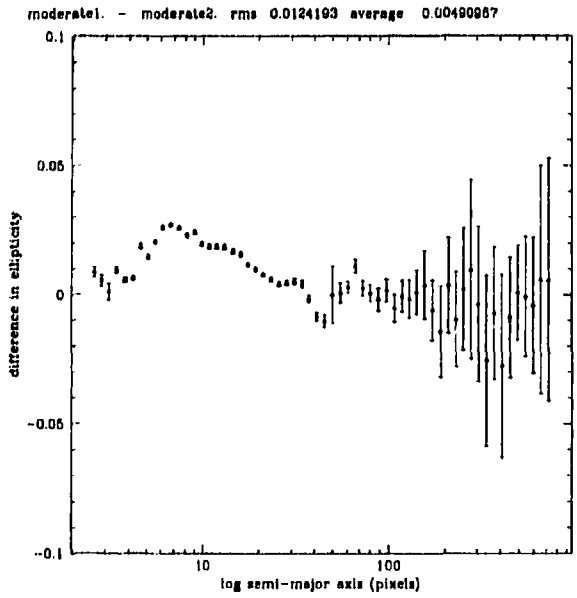

Figure 20: Isophote ellipticity differences between the reference image and the artificial image convolved with a Gaussian of FWHM = 1″.6, as a function of the semi-major axis.

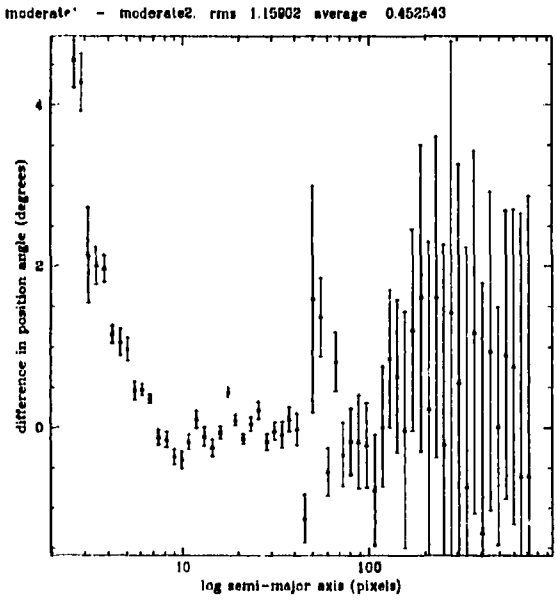

Figure 21: Isophote position angle differences between the reference image and the artificial image convolved with a Gaussian of FWHM = 1″.6, as a function of the semi-major axis.

Subtracting 4 from 3 yields

$$\Delta m = m' - m = 2.5 \log \left(\frac{I - I_{bg}(1+\epsilon)}{I - I_{bg}} \right) \tag{5}$$

As the intensity approaches the sky value, a small error in sky intensity propagates into a large error in magnitude. Figure 22 shows Equation 4 for three different values of ϵ. The effect of committing an error in sky subtraction was also tested on the artificial image. This image was given a sky intensity of 320 ADU, and 317 ADU were subtracted from the image so that a 1% error was committed (Figure 23. As in Figure 22, the error increases quickly when the isophote intensity approaches the sky intensity.

Since sky subtraction simply involves the subtraction of a constant value from the image, there should be no resulting effect on the fitted ellipse parameters; figures 24 and 25 prove this to be the case.

4.6 Computation of isophote intensity

As mentioned in §4.1, `ellipse` was used to compute the geometric parameters of the isophotes, but new code was written to the compute the isophote intensity. This was necessary because of a stricture of `ellipse`: for a given annulus, more than 50% of the pixels must have a defined intensity and lie within the image boundaries. If this limitation is exceeded, the routine terminates. So, for example, if `ellipse` gets to a semi-major axis that is so large that more than 50% of the points in the annulus are outside of the image, it stops. Since images were mosaicked into a size of $\approx 1600 \times 900$,

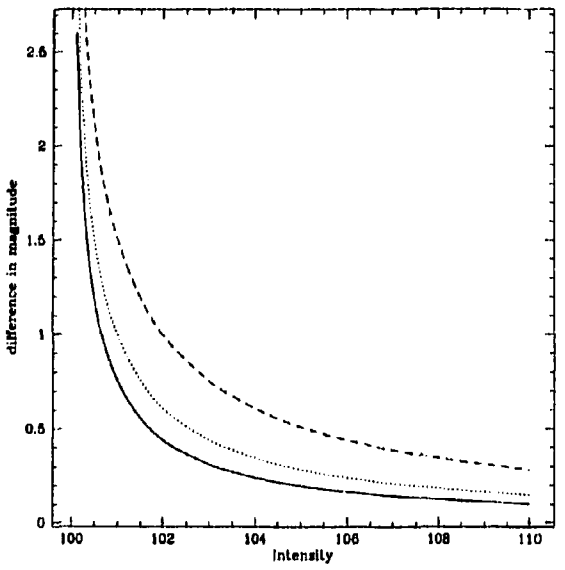

Figure 22: The error in sky subtraction is translated from intensity units to magnitude. The solid line, dotted line, and dashed line show error in sky subtraction of 0.5%, 1.0%, and 2.0%. The sky intensity is 100.

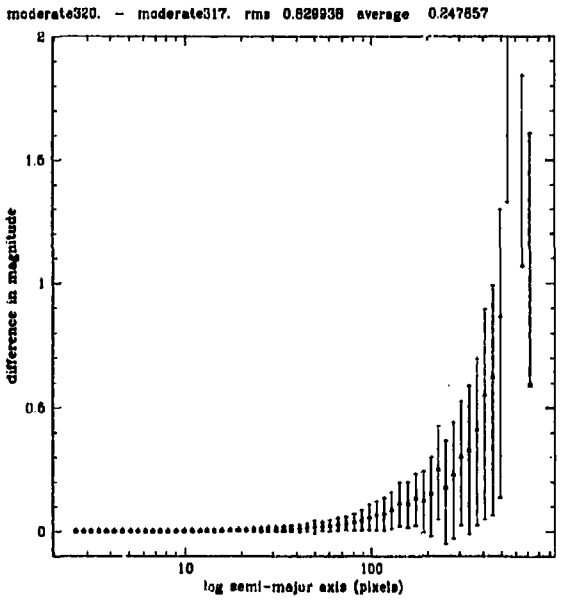

Figure 23: A 1% error was committed in sky subtraction and the resulting isophotal intensities were subtracted from the true values. The difference increases dramatically at large radii, where the isophote intensity approaches the sky intensity.

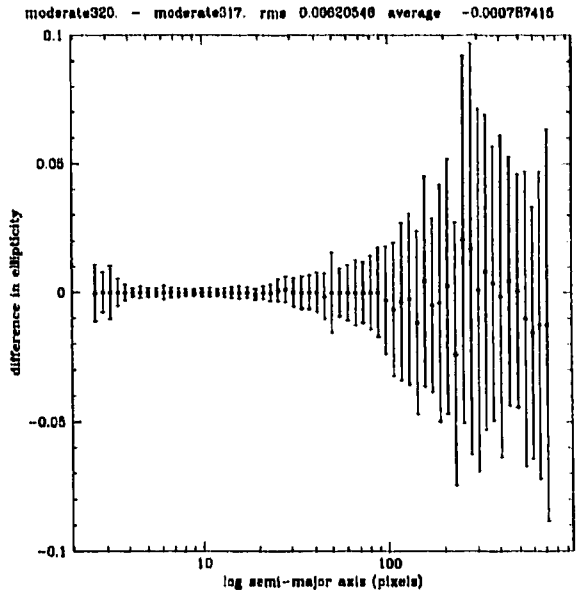

Figure 24: A 1% error was committed in sky subtraction and the resulting isophotal ellipticities were subtracted from the true values. An error in sky has no effect on ellipticity.

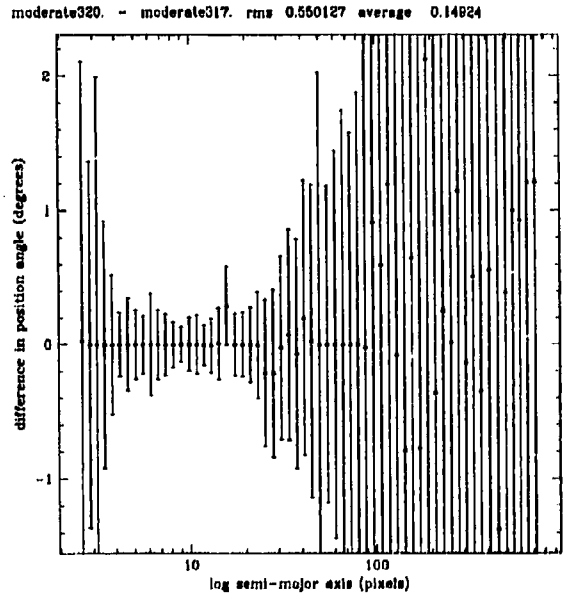

Figure 25: A 1% error was committed in sky subtraction and the resulting isophotal position angles were subtracted from the true values. An error in sky has no effect on position angle.

and the dominant galaxy lay in the centre of the left side of the frame, it was therefore impossible to measure isophotes into the right side of the frame. A new code (given the name *ANNULI*) was written to circumvent this limitation.

The routine **ellipse** has two options for rejecting objects: pixel clipping and masking. Pixel clipping has an arbitrary nature and is rather indiscriminant; the severity of this was not realized until **ellipse** was compared to the new routine, *ANNULI*, which uses an iterative sigma clipping algorithm to reject deviant pixels. For each elliptical annulus, *ANNULI* computes the mean and standard deviation of the pixel intensities. These statistics are then recomputed, ignoring any pixels that have intensities $\pm k\sigma$ away from the mean, where k was set to 2 for all computations. This iterative procedure stopped when either (1) a user specified maximum number of iterations was reached, (2) the mean intensity change between iterations was less than a user specified threshold, or (3) a user specified minimum number of pixels in the sample was reached.

Since the sophisticated algorithms used in **ellipse** can reliably and accurately compute the isophotal ellipse parameters, even when there is a fair amount of contaminating objects (as shown in §4.3), to code *ANNULI* to compute the ellipse parameters itself would only have been a duplication of effort. In this sense, *ANNULI* was not intended as replacement for **ellipse**; the new routine merely recomputes the isophotal intensities using a more robust method.

At large radii where the isophotes are dim, fitted ellipse parameters can be greatly

influenced by contaminating objects; the ellipse centre tends to wander, as do position angles and ellipticities. Therefore, *ANNULI* uses the parameters generated by `ellipse` out to a user specified semi-major axis, and after this threshold is reached the ellipse parameters were held constant. Fixing the ellipse parameters, however, assumes that the galaxy has no morphological changes (i.e., no twisting or flattening isophotes) after the threshold radius, which may not be generally true. To investigate the consequences of fixing the position angle and ellipticity, profiles of the model galaxy were computed using parameters that were fixed at various incorrect values over the *entire* range of radii — the worst case scenario. In Figure 26, isophotal intensities were computed using three different ellipticities, then subtracted from the reference intensities. An incorrect ellipticity can have quite a large effect at small radii, but in all cases the error decreases with radius. This is a pleasing result: the errors at small radii are grossly overestimated by fixing the parameters, and at large radii where the parameters are indeed fixed, the errors are small. For these tests, the threshold radius was set to zero to fix the parameters. The threshold radius for this galaxy was ≈ 150 pixels, and from Figure 26 one can see the error incurred by fixing the ellipticity was 0.02 magnitudes (at $r \simeq 150$ pixels) for the largest ellipticity used. This error is quite small when compared with errors incurred by sky subtraction (see §4.5.

Figure 27 shows the effect of fixing the position angle. Similar to the effects of fixing the ellipticity, the errors decrease with radius. The errors produced by a fixed,

incorrect position angle are much less severe than those incurred by a fixed, incorrect ellipticity. Surprisingly, even a position angle off by 60° results in an error of only ≈ 0.03 magnitudes. This result does have a simple explanation: an isophote with a position angle twisted from the actual value will pass through areas both closer to the core (hence brighter) and further from the core than the actual isophote, and compensation is achieved. The error that an incorrect position angle has on the intensity increases with ellipticity: in a circular galaxy, it makes no difference on position angle. The mean ellipticity of the reference galaxy is 0.28 (for comparison, a chicken's egg is about 0.3).

The effect of an incorrect ellipse centroid has on isophotal magnitude was not investigated, since it is much more unlikely for the isophote centre to move than it is for the position angle or ellipticity to change. The position angles and ellipticities of the poor cluster BCGs frequently varied by significant amounts (§6), but the isophote centres varied at most by two pixels. At large radii where the ellipse parameters were held fixed, an error in the isophote centre would introduce only a small error, since the radial intensity gradient is small. The de Vaucouleurs law (Equation 14) asymptotically approaches zero intensity at large r. The profile can, however, fall off rapidly at the detection threshold.

Once the integrated intensity is known in ADU, it is converted to a magnitude via:

$$\mu = \mu_0 - 2.5 \log\left(\frac{I}{tA}\right) \tag{6}$$

where μ_0 is an arbitrary magnitude zero point, t is the integration time of the exposure, and A is a factor to convert the area of a pixel into arcsec^2. To make certain that *ANNULI* was computing the isophotal intensities correctly, profiles of the real galaxies were computed and compared with those generated by `ellipse`. Immediately, a difference was noticed between the two programs that began in the middle of the profile and increased towards dimmer magnitudes, which was caused by pixel clipping. For most of the profiles, adjusting the clipping parameter could affect the profile by 0.5 magnitudes at low surface brightness levels. By adjusting the clipping parameter, the profiles computed by the two different routines could be brought into agreement. This is, admittedly, a major downfall of using indiscriminant pixel clipping for object rejection. One does not know beforehand what amount of pixel clipping to use to obtain the correct profile! The iterative $k\sigma$ rejection scheme is a much safer approach. Figure 28 compares `ellipse` and *ANNULI* to the model galaxy. The two routines break from the model profile around the twenty-first magnitude, and are systematically brighter because of contamination from other objects, but the computed profiles are always consistent with the model profile within the error bars.

Since the model galaxy used for the artificial images discussed so far was created from a real galaxy, its true profile was not known. As an additional test, a galaxy described by a de Vaucouleurs law (defined in §6.2) was created and measured using *ANNULI*. The slope of the computed profile was exactly equal to the slope used to

generate the profile, thus ruling out the possibility of systematic errors in the code. Contaminating objects were added to the image, as discussed in §4.2, and the profile was remeasured (Figure 29). All but six points are consistent with the model profile, within the error bars, assuring that the $k\sigma$ scheme is doing a reasonable job of rejecting objects. Furthermore, masking was also tested. Objects were masked out using very generous areas, to make certain that the halos of the objects were ignored. The profiles from the masked and unmasked images were almost identical; there were only a few points that showed any differences, these were less than 0.05 magnitudes, and occurred in the faintest parts of the profile, where the errors are largest. This comparison was also done on some program images, and similar results were obtained. Therefore, it can be said with confidence that the $k\sigma$ scheme adequately rejects objects, and that little is to be gained by masking.

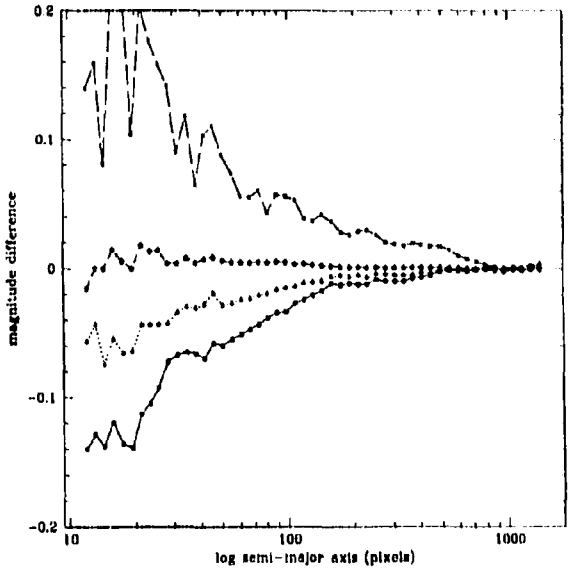

Figure 26: Consequence of an incorrect ellipticity. Isophotes were computed using an ellipticity of 0.1 (boxes), 0.2 (triangles), 0.3 (stars), and 0.6 (crosses), then subtracted from isophotes computed using the mean ellipticity of the model galaxy, 0.28.

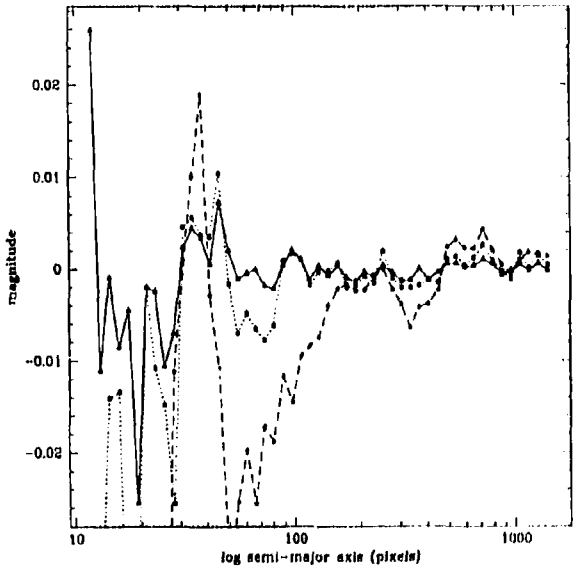

Figure 27: Consequence of an incorrect position angle. Isophotes were computed using a position angle of 10° (triangles), 20° (boxes), and 40° (stars) away from the mean position angle of the model galaxy, then subtracted from the reference isophotes.

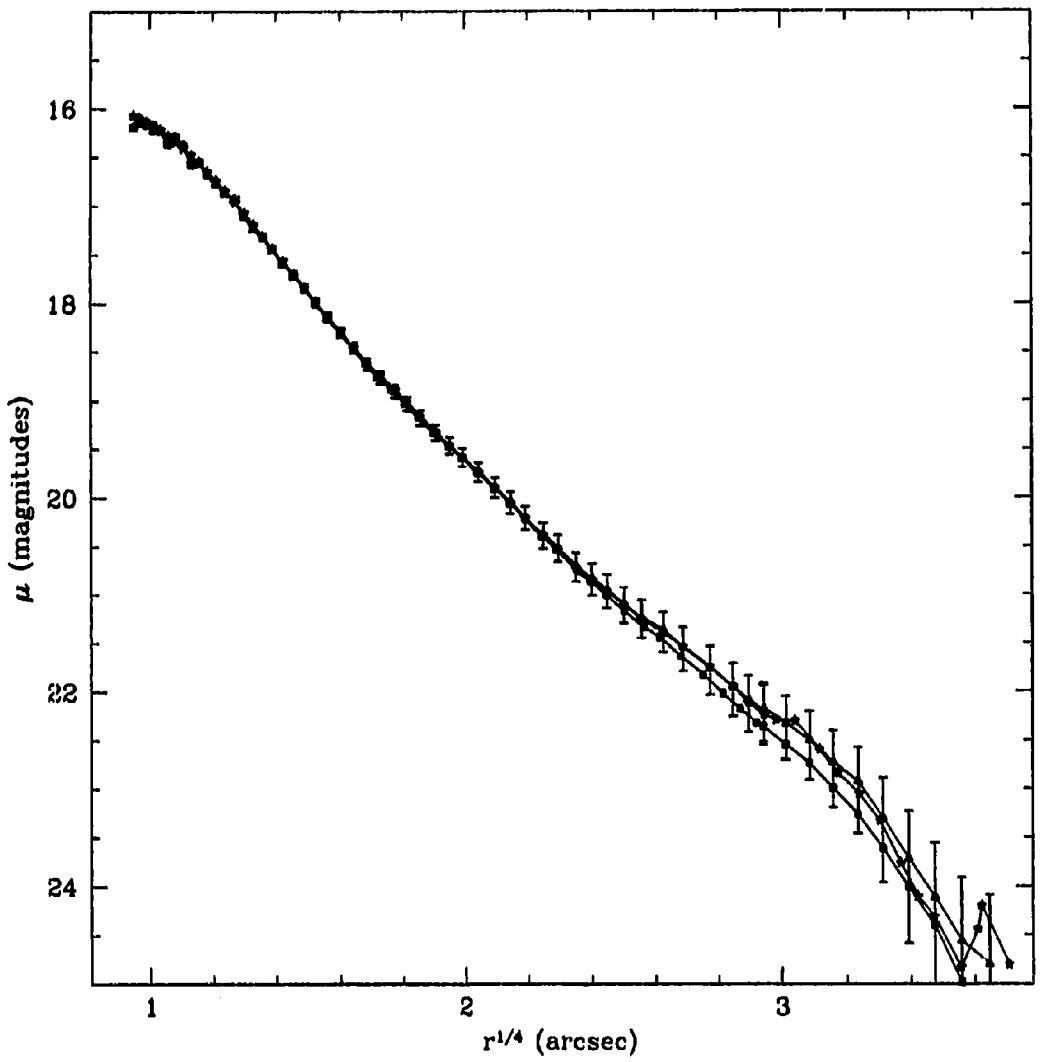

Figure 28: Surface brightness (μ) of the model galaxy (boxes) is plotted, along with the profile computed using **ellipse** (stars) and ANNULI (triangles). Error bars include Poisson shot noise, and a 0.5% error in both flat fielding and sky subtraction.

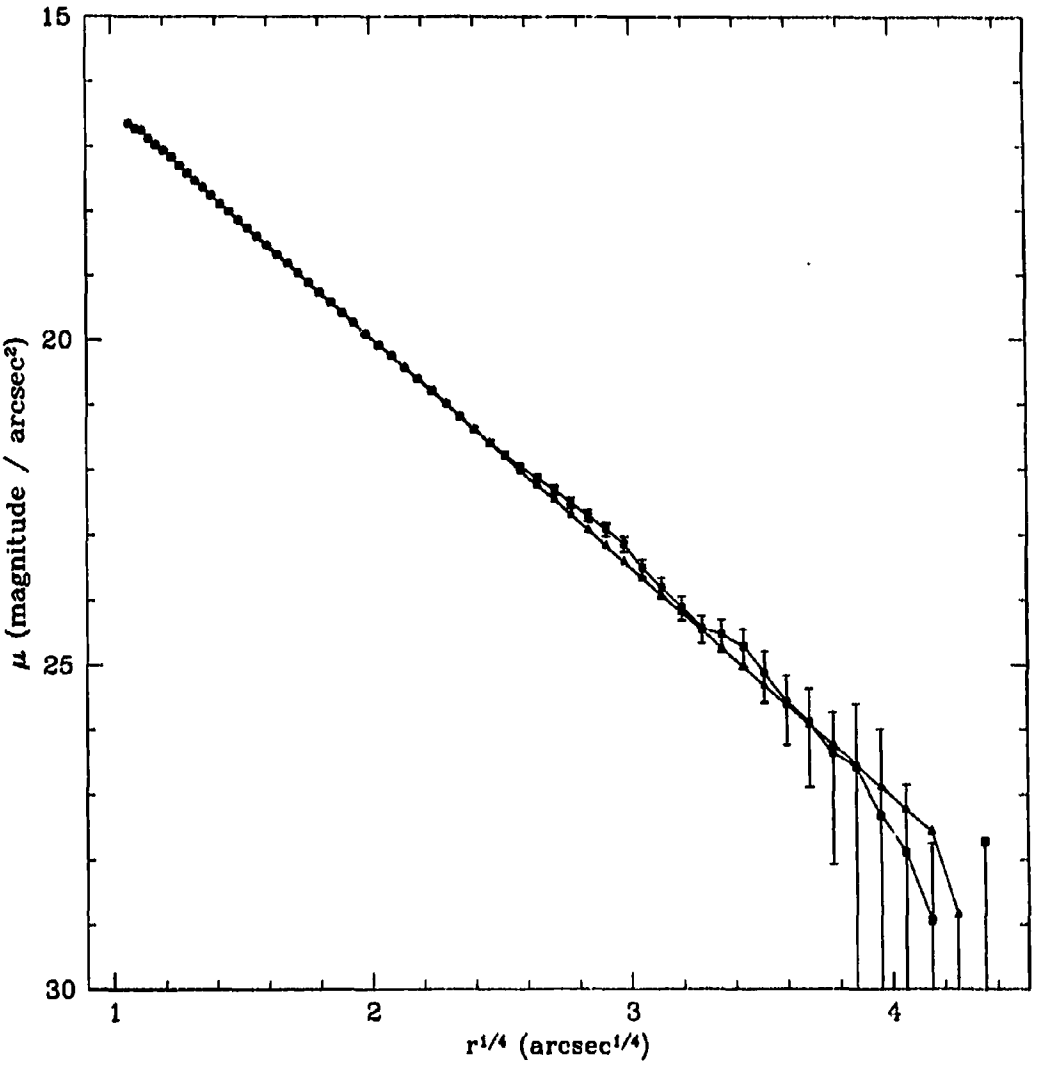

Figure 29: A de Vaucouleurs profile was created and measured with ANNULI (triangles). Contaminating objects were added to the galaxy, and the profile was remeasured (boxes). Error bars include Poisson shot noise, and a 0.5% error in both flat fielding and sky subtraction.

5 Transformation to standard magnitudes

5.1 Standard star photometry

Fourteen Landolt standard stars (Landolt, 1992) were imaged in B and R at varying airmasses over the observing run. These images were pre-processed in the same manner described in §3. Instrumental magnitudes of the standard stars were computed using the aperture photometry routines in DAOPHOT. An aperture is chosen about 4 to 5 times larger than the full width half maximum (FWHM) of the point spread function (PSF). Larger apertures will encompass more of the light in the wings of the PSF, but may also capture light from nearby stars. None of the standard stars suffered from crowding, so the aperture used was 5 times the FWHM of the PSF. The photometry routine sums the pixel intensities inside the chosen annulus, computes the sky value in an area surrounding the annulus, and adjusts the summed intensity accordingly:

$$I = \sum I_i - \pi r_a^2 I_{sky} \tag{7}$$

where I is the summed intensity, I_i are the pixel intensities, πr_a^2 is the annulus area, and I_{sky} is the sky intensity. The sky intensity is determined from a user specified radius that is, of course, larger than the aperture used to measure the star intensity. An estimation of the amount of light contributed to the sky by the star is made and corrected for. The instrumental magnitude is computed by scaling the intensity by

the integration time, and adjusting to a zero point:

$$mag = mag_0 - 2.5 \log\left(\frac{I}{t}\right) \tag{8}$$

The arbitrary magnitude zero point, mag_0 was set to 25.

5.2 Transformation equations

The transformation from instrumental to standard (apparent) magnitude involves a zero point shift, coefficients that depend on airmass, colour, and a second order coefficient that depends both on airmass and colour:

$$b = B + b_1 + b_2 X_B + b_3(B - R) + b_4 X_B(B - R) \tag{9}$$

$$r = R + r_1 + b_2 X_R + r_3(B - R) + b_4 X_B(B - R) \tag{10}$$

where the subscripted letters are the coefficients, lower case letters denote instrumental magnitudes, upper case letters denote standard magnitudes, and X is the airmass.

Once the instrumental magnitudes for the standard stars have been measured, they are used by the `fitparms` routine under DAOPHOT to compute the transformation coefficients. `fitparms` uses an iterative, non-linear least squares method to determine the coefficients, which are listed in Tables 3 and 4 along with some other important statistics that describe the fit. For example, the root mean squared of the residual between the computed and catalogued magnitude is tabulated.

Under photometric observing conditions, the second order coefficient is negligible and usually held fixed at zero. This was done for all nights, even though some were not perfectly photometric; fitting the colour-airmass coefficient did not significantly improve any of the fits. The r_4 coefficient was also negligible, but holding it fixed made no significant difference in the residuals.

Upon inspection of the coefficients, night 6 coefficients deviate significantly from the others. This night was not photometric and the calibration will be unreliable, so night 6 will be excluded from the following discussion. The B coefficients all agree, within their uncertainties. The R coefficients for nights three and four deviate significantly from nights 1, 2, and 5; the cause of this is unknown and puzzling, since the B coefficients for these nights are normal. To improve the fits, stars with large residuals were discarded, but these efforts proved futile. Instead of using night 3 and 4 R coefficients, an average over nights 1, 2, and 5 was used. Ultimately, this only affected night 4, since no galaxies were observed in R on night 3.

To quantify the errors involved in using averaged coefficients, galaxy profiles were computed using nightly coefficients and compared with profiles computed using both B coefficients averaged over nights 1 to 5, and R averaged over nights 1, 2, and 5. The only perceptible differences occurred for galaxies imaged on night 4, and it was very marginal. For night 4, $r_1 = 1.232 \pm 0.46$, $r_2 = 0.116 \pm 0.39$, while the R coefficients averaged over nights 1, 2, and 5 are $r_1 = 1.362 \pm 0.04$, $r_2 = 0.050 \pm 0.03$, and hence do not agree within the uncertainties. Substituting these

values into equation 10, assuming a typical airmass of 1.1, and ignoring the small colour term, the difference is 0.22 magnitudes. This difference is significant, but is the maximum error that can be committed, and is likely a large overestimation. As shown in §6, profiles from different authors frequently disagree by differences of this amount (and sometimes, considerably more), This is only one source of error, however, and there are many others. Furthermore, an error incurred by using averaged coefficients that are unrepresentative of the true coefficients will show up in the $(B - R)$ colour, since there was no problem with the B coefficients. This will be discussed further in §7.

To compute the isophotal standard magnitudes, Equations 9 and 10 are inverted and solved for the standard magnitudes. The implementation of this, however, was not straightforward, because the galaxy images in B were taken on different nights than those in R. Simultaneous B and R photometry on each night for the standard stars produced the coefficients. However, we did not have simultaneous B and R photometry of the galaxies, and so coefficients from different nights were used. The validity of this procedure rests on the assumption that the coefficients do not vary from night to night, which was discussed above.

To compute the standard magnitudes, an expression relating the instrumental $(b - r)$ colour to the standard $(B - R)$ colour was derived from Equations 9 and 10:

$$(B - R) = \frac{(b - r) - (b_1 - r_1) - (b_2 X_B - r_2 X_R)}{1 + (b_3 - r_3)} \tag{11}$$

Once the standard colour was found, it was substituted into Equations 9 and 10 to

obtain the standard magnitude. Note that the b_3 coefficients are small ($\bar{b_3} = -0.045$) and the r_3 coefficients are negligible. This lends further support to this procedure, since the errors in assuming the transformation coefficients do not change on a nightly basis are multiplied by a small colour coefficient. To demonstrate, consider NGC 5920 which has a $(B - R)$ colour of 1.96. The difference between the mean b_3 and the b_3 value for night 1 is 0.004. Multiplying this number by the $(B - R)$ colour gives a difference in magnitude of 0.007, which is the error committed in assuming the coefficients do not vary from night to night. It should also be noted that many authors use a colour coefficient averaged over their entire observing session, because this coefficient is dependent only on the optical train and not on atmospheric conditions.

Even though night 6 was not photometric, and there were problems with the R coefficients with nights 3 and 4, the standard calibration is not too important for the purposes of this project. We are mainly concerned with the *shape* of the BCG profile, not its magnitude. Errors in the standard calibration will shift the profile in brightness, but have almost no effect on the profile shape.

5.3 Extinction and K-corrections

Profiles have been corrected for reddening by foreground dust in the Galaxy using the $E(B - V)$ colour excess values compiled by Burstein and Heiles (1984). O'Donnell (1994) derived $A(\lambda)/A(V)$ extinctions, and expressed their extinction curves in the

form

$$\frac{A(\lambda)}{A(V)} = a(\lambda^{-1}) + \frac{b(\lambda^{-1})}{R_v} \tag{12}$$

where $R_v \equiv \frac{A_v}{E(B-V)} = 3.1$. Using their tabulated values for the B and R filters, $A_B = 4.1E(B-V)$ and $A(R) = 0.24E(B-V)$. Table 5 lists the BGC colours and extinctions.

K-corrections compensate for the redshifting of galaxy light, and are therefore dependent on z. McNamara and O'Connell (1992) give the following K-corrections: $K(U) = 3.4z$, $K(B) = 5.2z$, $K(V) = 1.5z$, $K(I) = 0.2z$. A smooth line was drawn through those points to obtain a K-correction in the R band of $K(R) = 0.6z$. Since redshift of the MKW and AWM clusters is typically $\simeq 0.02$, the K-corrections are quite small.

Once the extinction and K-correction is known, the observed magnitude is decreased appropriately:

$$B = B_{obs} - A_B - K_B \tag{13}$$

which makes the intrinsic magnitude brighter than the observed.

Table 3: STANDARD MAGNITUDE TRANSFORMATION COEFFICIENTS, B FILTER

night	1	2	3	4	5	6
minimum airmass	1.080	1.118	1.110	1.094	1.101	1.058
maximum airmass	1.564	1.503	1.750	1.552	1.964	1.787
reduced χ	1.005	1.003	0.981	1.001	1.004	1
RMS	0.011	0.014	0.017	0.011	0.015	0.419
const1	1.513	1.554	1.496	1.556	1.514	2.549
error in const1	±0.026	±0.035	±0.018	±0.044	±0.027	±0.661
const2	0.273	0.237	0.262	0.229	0.263	−0.666
error in const2	±0.021	±0.027	±0.014	±0.038	±0.021	±0.519
const3	−0.041	−0.042	−0.041	−0.048	−0.051	0.034
error in const3	±0.003	±0.004	±0.003	±0.004	±0.005	±0.13
const4	0	0	0	0	0	0
error in const4	0	0	0	0	0	0

Table 4: STANDARD MAGNITUDE TRANSFORMATION COEFFICIENTS, R FILTER

night	1	2	3	4	5	6
minimum airmass	1.080	1.118	1.110	1.094	1.101	1.058
maximum airmass	1.564	1.503	1.750	1.552	1.964	1.787
reduced χ	1.001	0.991	0.705	1.001	1.001	1
RMS	0.022	0.014	0.012	0.025	0.017	0.04
const1	1.364	1.308	1.225	1.232	1.36	0.704
error in const1	±0.046	±0.044	±0.017	±0.464	±0.032	±0.066
const2	0.045	0.069	0.138	0.116	0.035	0.716
error in const2	±0.034	±0.032	±0.013	±0.391	±0.025	±0.05
const3	0.006	0.01	0	0	−0.003	0.007
error in const3	±0.009	±0.006	±0	±0	±0.006	±0.011
const4	0	0	0	0	0	0
err const4	0	0	0	0	0	0

6 Results

6.1 Sky measurement

To measure the sky intensity, a large number of 10×10 boxes were used to sample the frame, staying as far away from the galaxy as possible and avoiding any objects. For each box, the median was computed and subsequently the median of the medians was calculated. For frames that were taken in both B and R, the sky brightness in magnitudes was calculated (table 6) and were very close to the expected values of $\mu_{B,sky} = 21.8$ and $\mu_{R,sky} = 20.4$ mag/arcsec^2 for the observing site.

As a check, the sky intensity was also computed using the same method described in §3.3. A large rectangular box containing approximately 100 000 pixels or more was chosen along the edge of the frame furthest from the galaxy. In most cases, there were few contaminating objects far from the galaxy. The sky intensities computed by the iterative $\pm k\sigma$ rejection scheme were always within a few tenths of ADUs of the multiple box measurements.

The large, mosaicked image reaches $\sim 10'$ from the galaxy centre, and at a typical redshift of $z = 0.02$, $10' \simeq 300$ kpc for $H_0 = 75$. This should allow a local sky determination to better than 0.5% (T. Bridges, private communication).

6.2 Surface photometry

The radial brightness profiles of the dominant galaxies obtained using procedures described in §4.6 are shown in figures 30 to 37, along with profiles from three different sources. The profiles of Thuan and Romanishin (1981, TR) and Morbey and Morris (1983, MM) have been corrected as described in §5.3. Malumuth and Kirshner (1985, MK) used the galactic absorption model of Sandage (1973), which has been superseded by the extinctions compiled by Burstein and Heiles (1984), and therefore Malumuth and Kirshner's profiles have been updated to the new standards.

de Vaucouleurs (1948) found a relation that describes the brightness profiles of elliptical galaxies over a large range in magnitudes:

$$\log(I(r)) = -3.33\left(\left(\frac{r}{r_e}\right)^{1/4} - 1\right) + \log(I_e) \tag{14}$$

where r_e, the effective radius, is the radius that contains one half of the total brightness, and I_e, the effective intensity, is the surface brightness at that radius. The de Vaucouleurs (or $r^{1/4}$) law, is strictly an empirical relation; it has no dynamical or other theoretical basis. The following plots include magnitude as a function of $r^{1/4}$, where $r = \sqrt{ab}$ is the geometric mean of the semi-major and semi-minor axes. In this space, the de Vaucouleurs law is a straight line. The best fitting de Vaucouleurs law was fit by least-squares and plotted for both the B and R profiles. The effective intensity and radii are extracted from the straight line fit, $\mu = A + B \times r^{1/4}$ via:

$$r_e = \left(\frac{3.33 \times 2.5}{B}\right)^4 \tag{15}$$

Table 5: DOMINANT GALAXY COLOURS AND EXTINCTION COEFFICIENTS

Galaxy	Cluster	$(B-V)$	$(V-R)$	$(B-R)$	A_V
UGC 09799	Abell 2052.....	1.11[a]	0.61	1.72[b]	0.04
NGC 6051	AWM 4.....	1.18	0.83	2.01	0.13
NGC 6269	AWM 5.....	1.20	0.94	2.14	0.20
10276 − 0255	MKW 2.....	1.14	0.90	2.04	0.04
10246 − 0304	MKW 2S.....	1.13	0.95	2.08	0.05
NGC 5920	MKW 3S.....	1.22	0.74	1.96	0.05
NGC 4073	MKW 4.....	1.06	0.90	1.96	0.01
NGC 5200	MKW 5.....	1.11	0.89	2.00	0.09

A_V taken from Burstein and Heiles (1984).
Colours taken from Schild and Davis (1979) except for:
[a]Smith and Heckman (1989)
[b]Colless et al. (1993)
[c]Thuan and Romanishin (1981)

$$\mu_e = A + 2.5 \times 3.33 \tag{16}$$

where μ_e is the effective surface magnitude defined in Equation 6. For all plots, the inner 10 points were not used in the fits, since seeing effects here are very influential, and the magnitudes are not reliable.

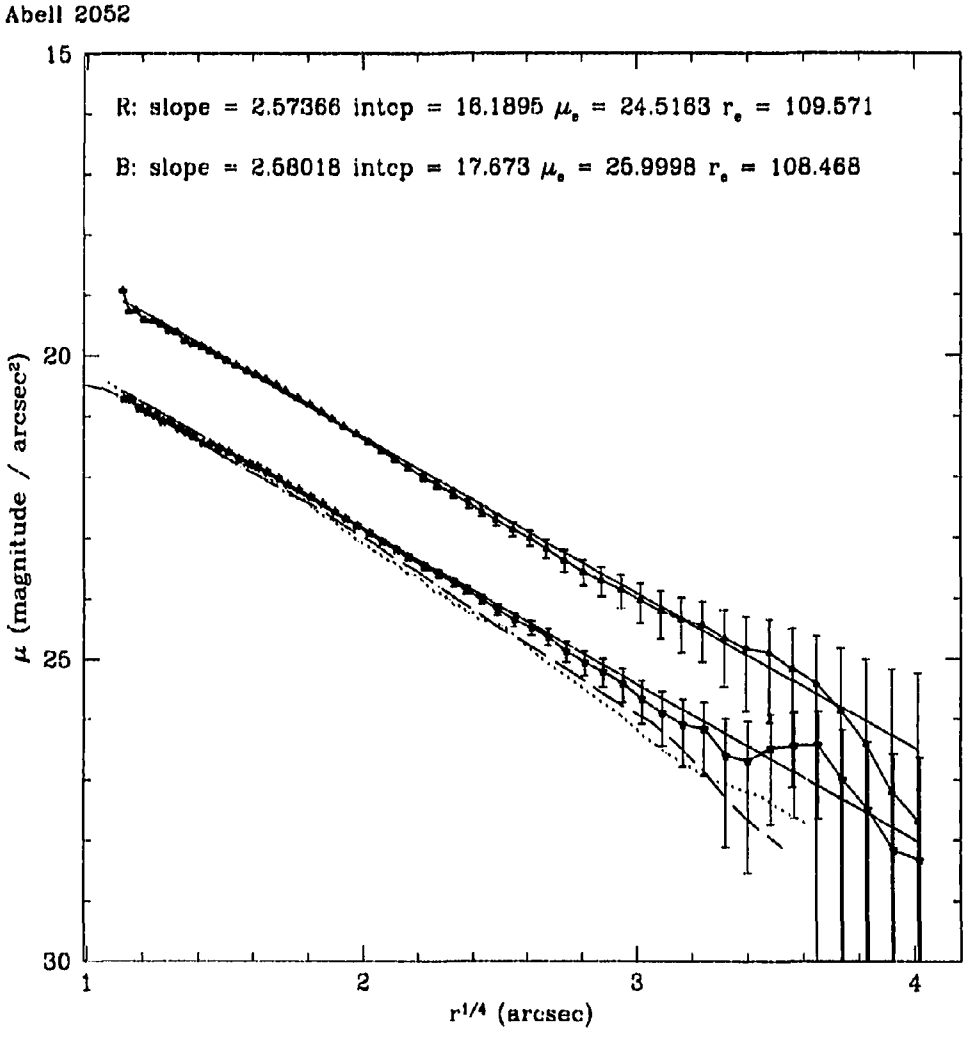

Figure 30: Surface brightness profile of UGC 09799 (Abell 2052) in B (stars) and R (triangles). The best fit de Vaucouleurs parameters are given at the top of the graph. Also plotted in B are profiles from these sources: (1) MM (dotted line); (2) MK, V transformed to B (long dash). The MM profile required a downward (faint) shift of 0.7 magnitudes bring it into registration with the other profiles.

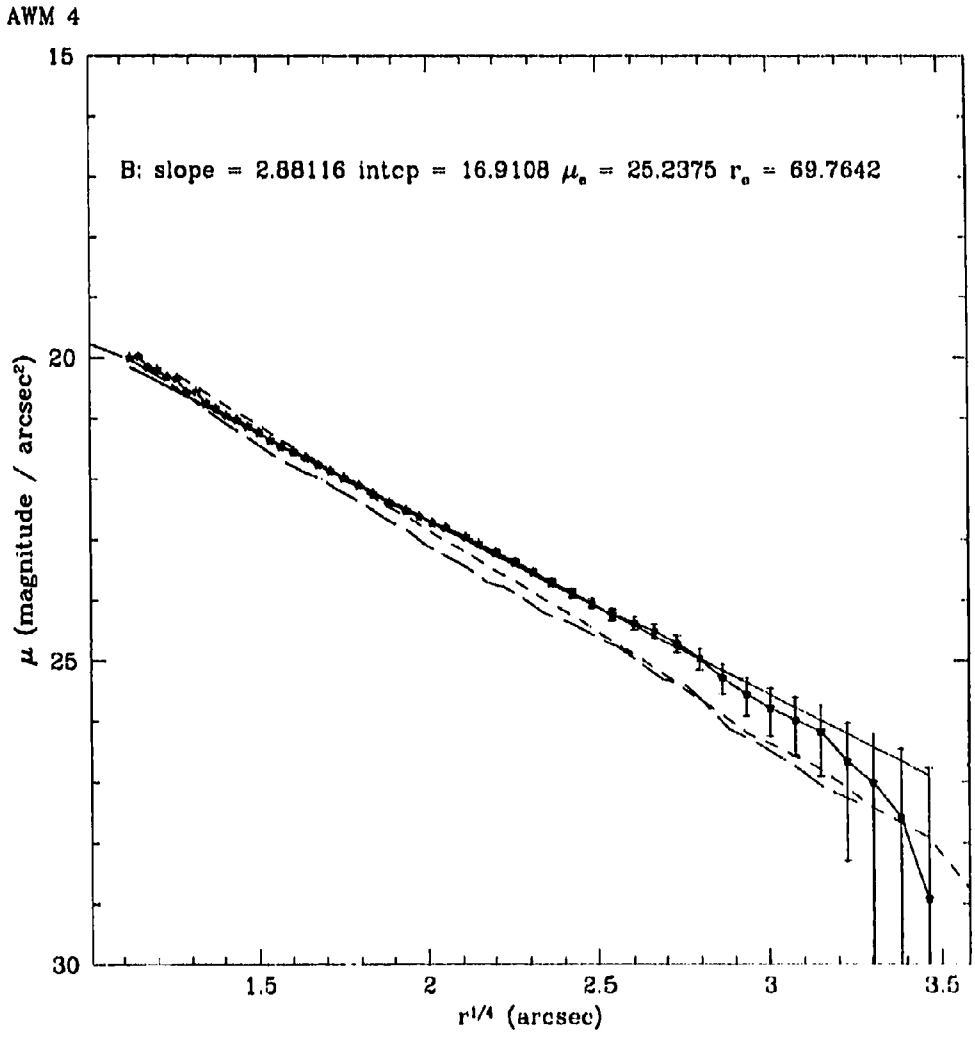

Figure 31: Surface brightness profile of NGC 6051 (AWM 4) in B (stars). The best fit de Vaucouleurs parameters are given at the top of the graph. Also plotted in B are profiles from these sources: (1) TR, g transformed to B (short dash); (2) MK, V transformed to B (long dash).

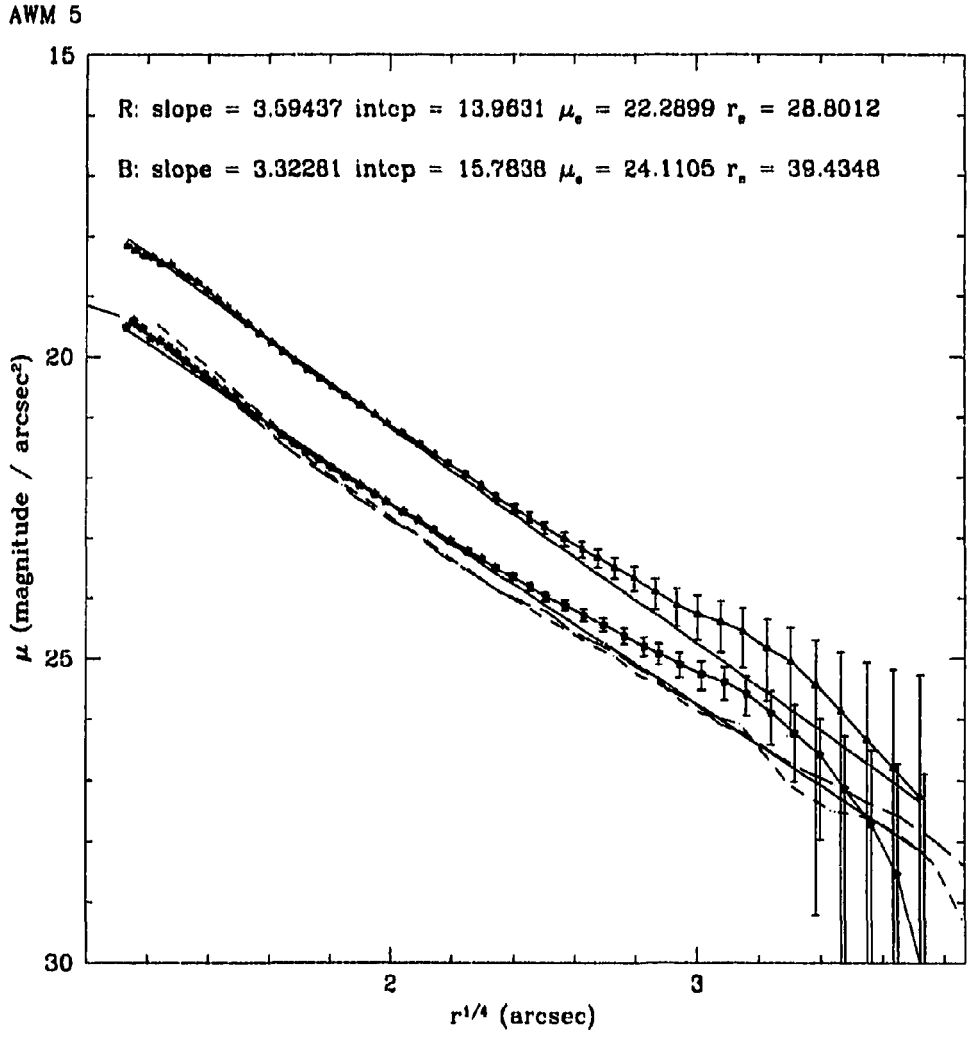

Figure 32: Surface brightness profile of NGC 6269 (AWM 5) in B (stars) and R (triangles). The best fit de Vaucouleurs parameters are given at the top of the graph. Also plotted in B are the profiles from the following sources: (1) TR, g transformed to B (short dash); (2) MK, V transformed to B (long dash).

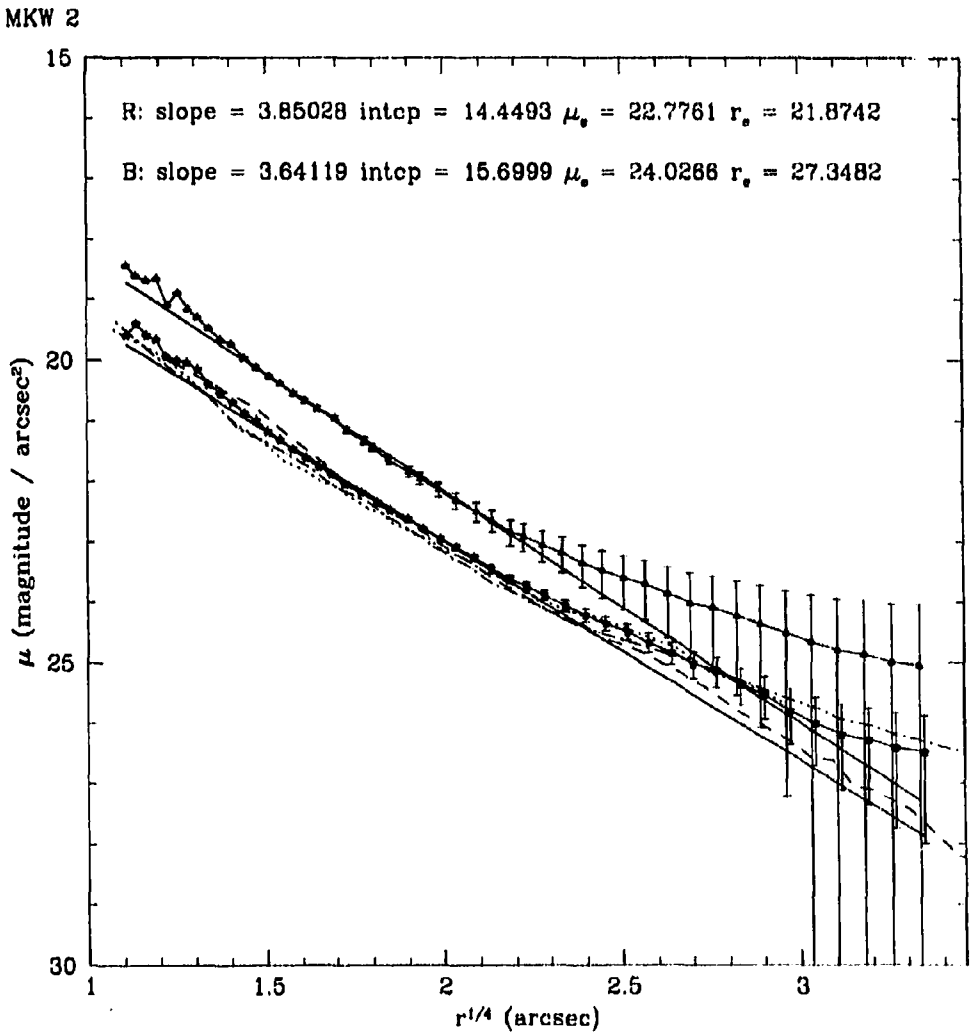

Figure 33: Surface brightness profile of 10276 − 0255 (MKW 2) in B (stars) and R (triangles). The best fit de Vaucouleurs parameters are given at the top of the graph. Also plotted in B are profiles from these sources: (1) MM (dotted line); (2) TR, g transformed to B (short dash); (3) MM, J transformed to B (dot - short dash). The R profile was obtained on night 6 which was not photometric, and hence the zero point is not reliable.

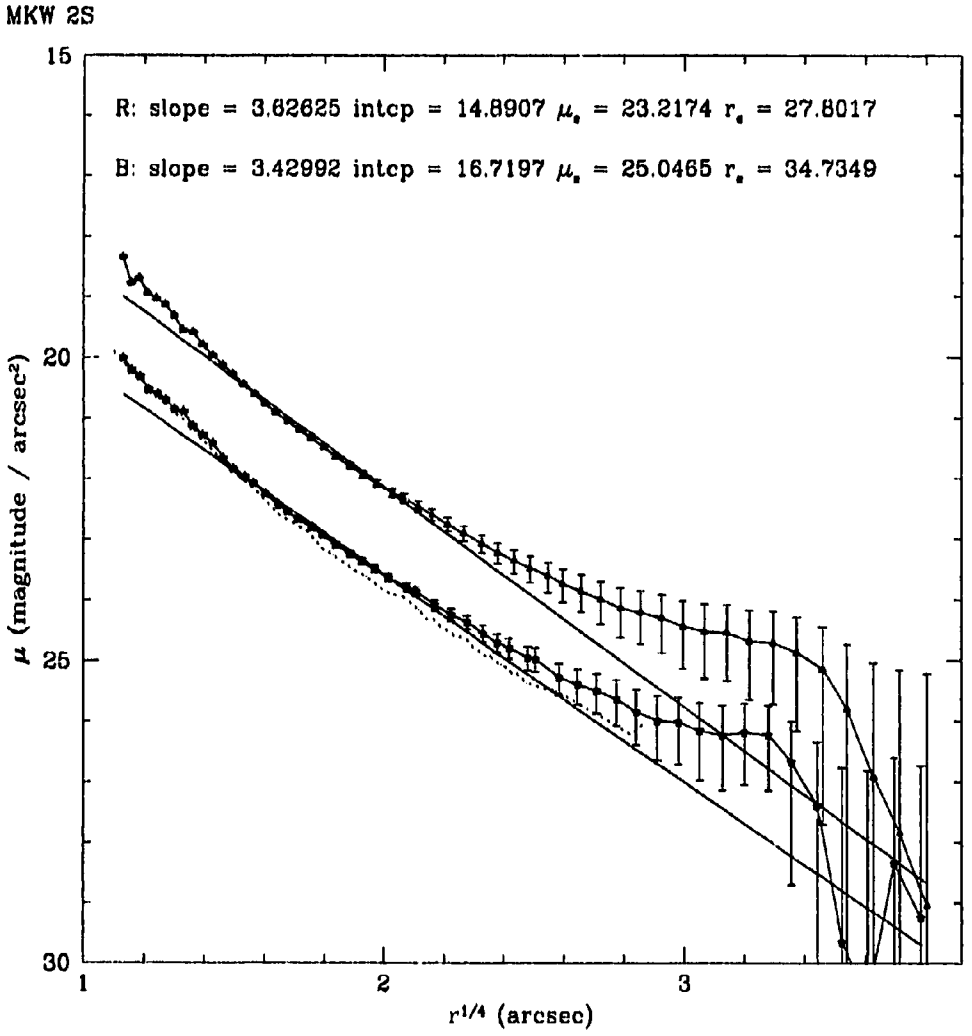

Figure 34: Surface brightness profile of 10246 − 0304 (MKW 2S) in B (stars) and R (triangles). The best fit de Vaucouleurs parameters are given at the top of the graph. Also plotted is the B profile from MM (dotted line).

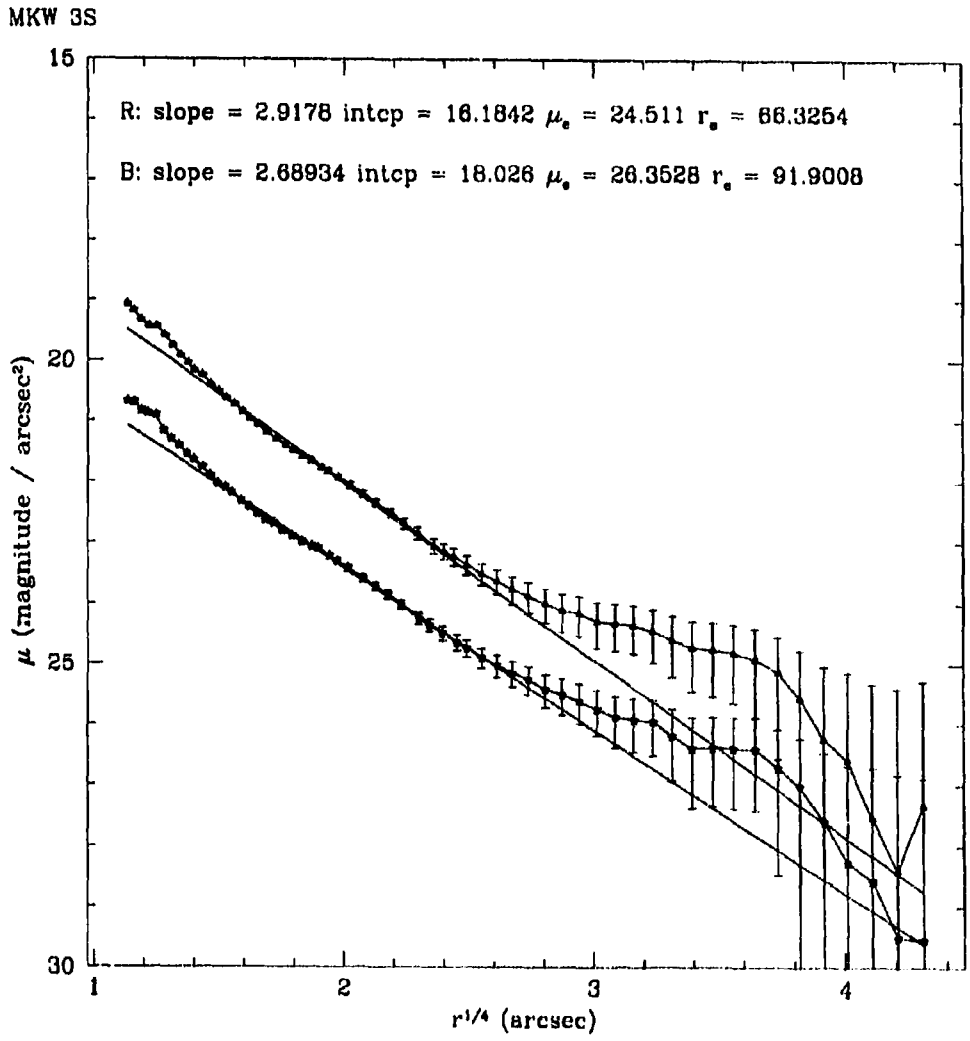

Figure 35: Surface brightness profile of NGC 5920 (MKW 3S) in B (stars) and R (triangles). The best fit de Vaucouleurs parameters are given at the top of the graph.

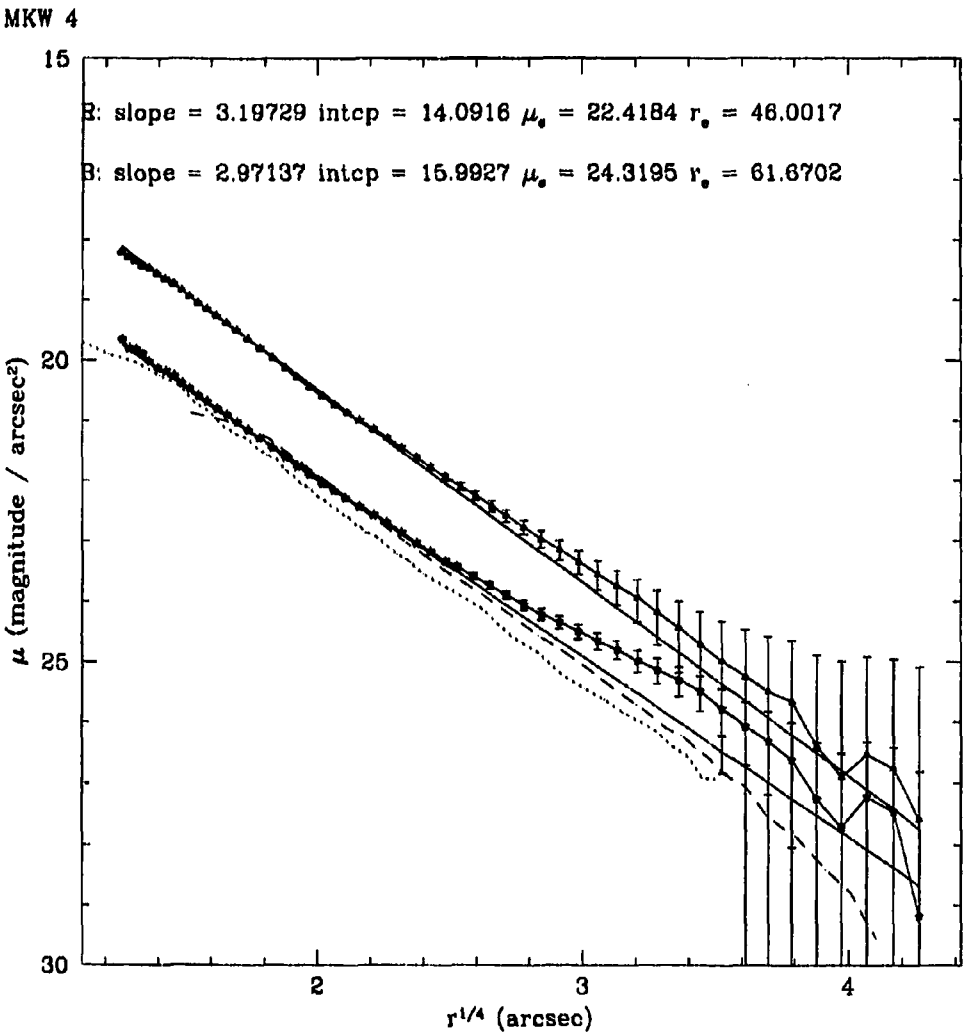

Figure 36: Surface brightness profile of NGC 4073 (MKW 4) in B (stars) and R (triangles). The best fit de Vaucouleurs parameters are given at the top of the graph. Also plotted in B are profiles from these sources: (1) MM (dotted line); (2) TR, g transformed to B (short dash).

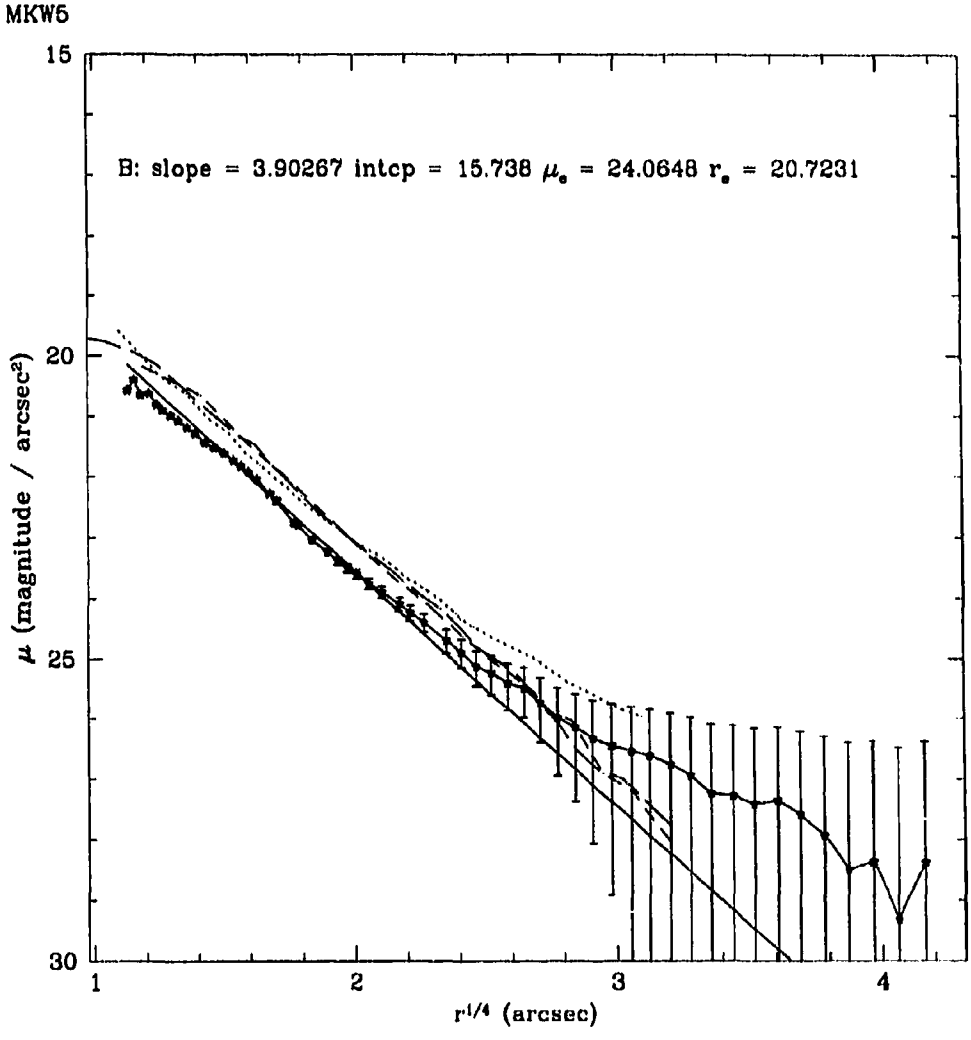

Figure 37: Surface brightness profile of NGC 5400 (MKW 5) in B (stars). The best fit de Vaucouleurs parameters are given at the top of the graph. Also plotted in B are profiles from these sources: (1) MM (dotted line); (2) TR, r transformed to B (short dash); (3) MK, V transformed to B (long dash). This night was not photometric, and the zero point is unreliable.

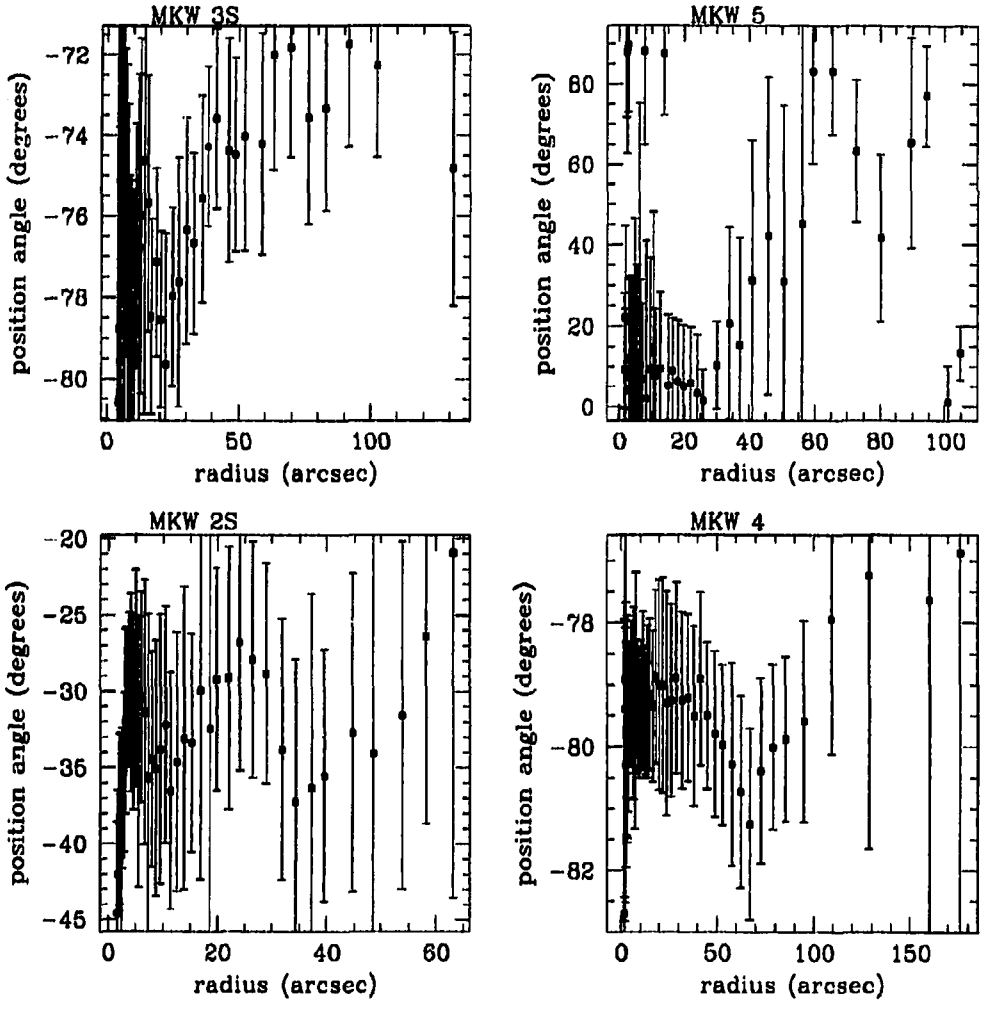

Figure 38: Position angle versus radius for poor cluster dominant galaxies. Position angle is measured counterclockwise from north, and lies between $-90°$ and $90°$. The position angles from the B and R images have been averaged.

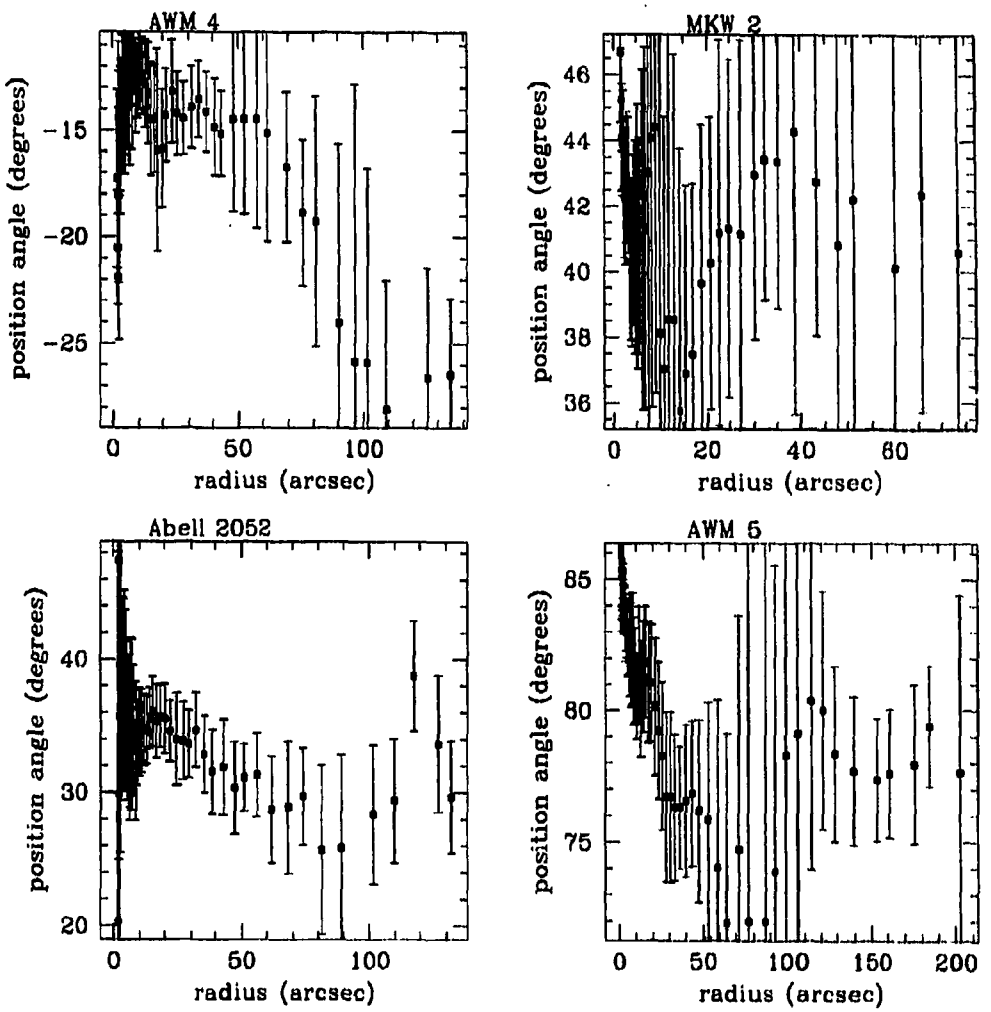

Figure 39: Position angle versus radius for poor cluster dominant galaxies. Position angle is measured counterclockwise from north, and lies between $-90°$ and $90°$. The position angles from the B and R images have been averaged.

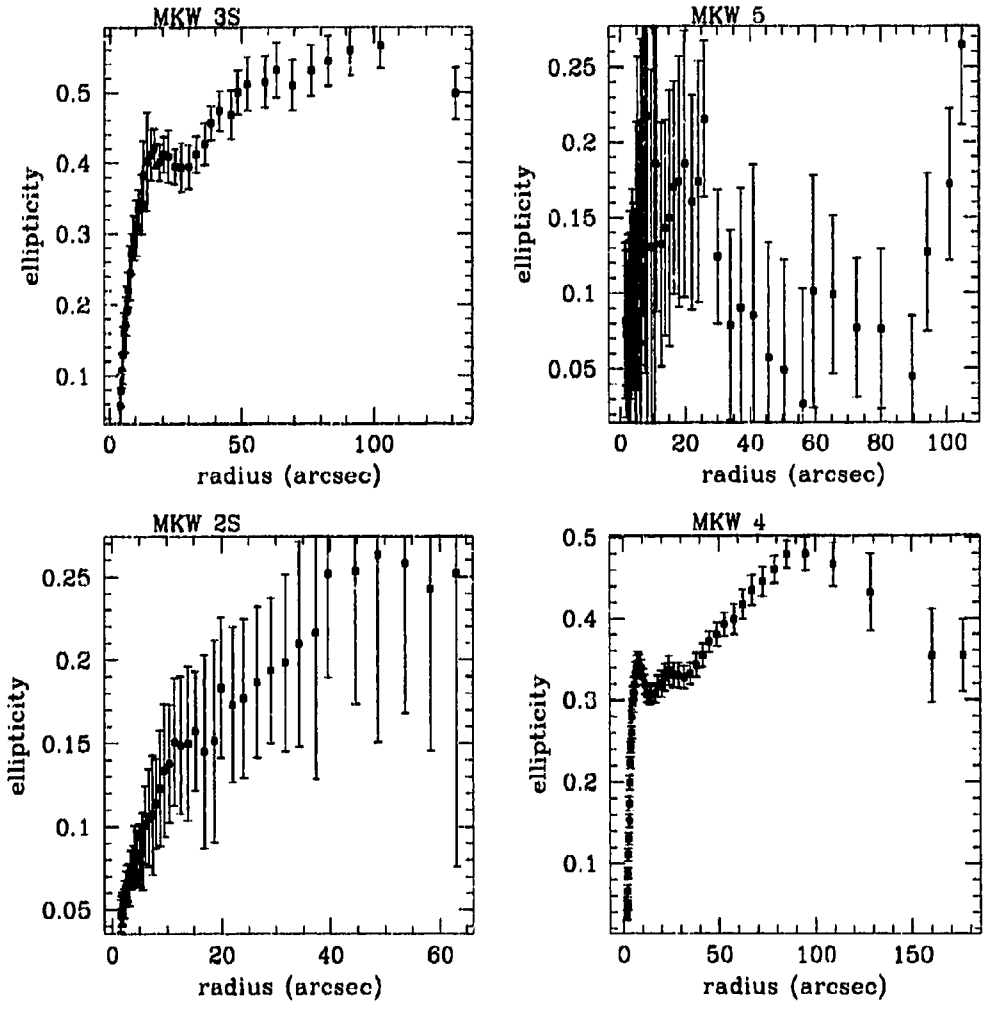

Figure 40: Ellipticity versus radius for poor cluster dominant galaxies. The ellipticities from the B and R images have been averaged.

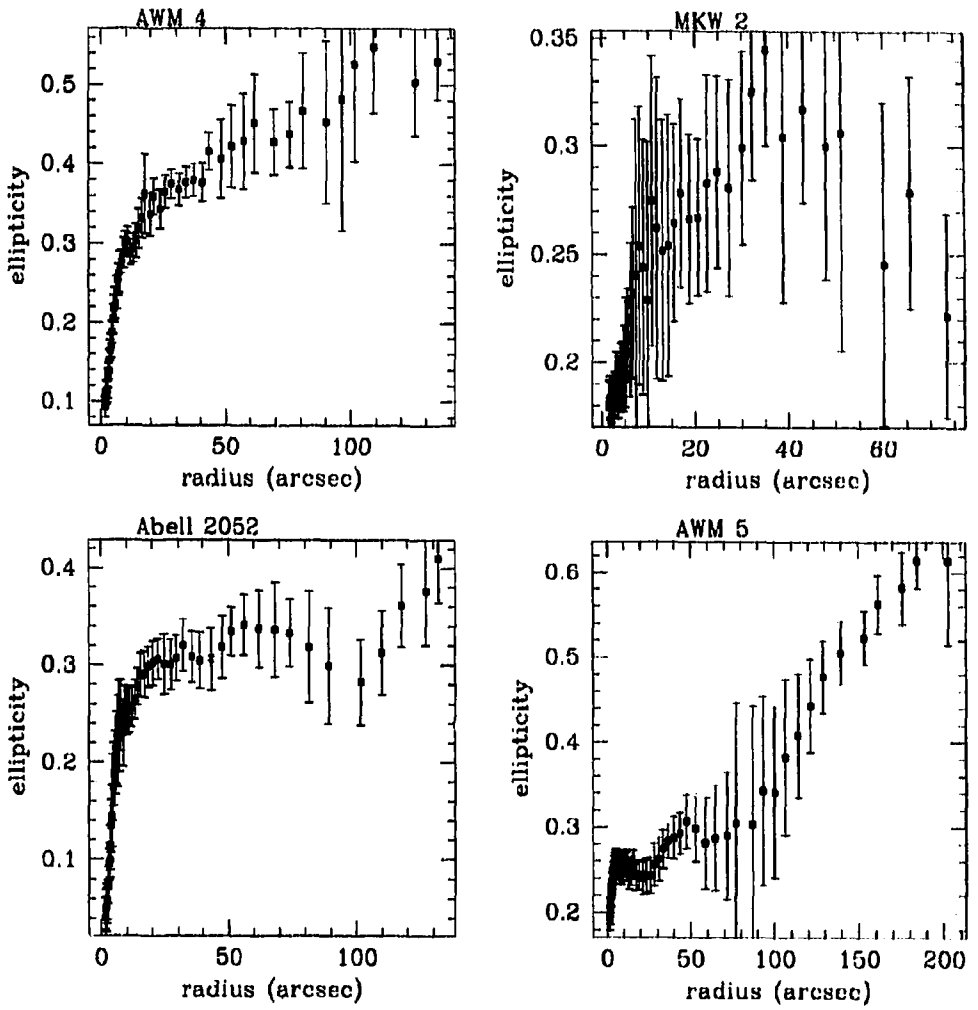

Figure 41: Ellipticity versus radius for poor cluster dominant galaxies. The ellipticities from the B and R images have been averaged.

Table 6: SKY BRIGHTNESSES

frame	filter	mean	sigma	N	mag
Abell 2052	B	402.10	2.23	189	21.75
AWM 4	B	352.91	1.70	173	
AWM 5	B	321.73	1.81	201	22.02
MKW 2	B	420.50	3.00	156	21.58
MKW 2S	B	391.77	2.12	145	21.73
MKW 3S	B	343.63	2.11	140	21.88
MKW 4	B	421.57	1.94	180	21.68
MKW 5	B	503.18	2.12	202	
Abell 2052	R	1862.58	4.72	198	20.00
AWM 5	R	1604.39	4.35	160	20.13
MKW 2	R	2936.56	6.10	213	19.26
MKW 2S	R	1937.44	5.64	140	19.91
MKW 3S	R	1578.89	3.18	152	20.14
MKW 4	R	2154.06	5.94	187	19.84

Table 7: DE VAUCOULEURS PARAMETERS

		this study		other studies	
Galaxy	Cluster	$\log(r_e)$ (kpc)	μ_{B_e} (mag arcsec^{-2})	$\log(r_e)$ (kpc)	μ_{B_e} (mag arcsec^{-2})
UGC 09799	Abell 2052	2.01[e]	26.00	1.56	25.42[b]
		2.01[f]	26.10[a]		
NGC 6051	AWM 4	1.79[e]	25.24	1.44	24.03[c]
NGC 6269	AWM 5	1.57[e]	24.11	1.54	23.91[c]
		1.44[f]	24.24[a]		
10276 − 0255	MKW 2	1.45[e]	24.03	1.43	24.14[c]
		1.35[f]	24.66[a]	1.39	24.36[d]
10246 − 0304	MKW 2S	1.56[e]	25.05	1.12	23.68[d]
		1.46[f]	25.14[a]		
NGC 5920	MKW 3S	2.05[e]	26.36		
		1.90[f]	26.28[a]		
NGC 4073	MKW 4	1.55[e]	24.32	1.12	23.83[c]
		1.42[f]	24.30[a]	1.42	24.23[d]
NGC 5400	MKW 5	1.16[e]	23.66	1.21	23.73[c]
				1.43	24.62[d]

NOTE.— $H_0 = 50$ km s^{-1}Mpc^{-1}; $q_0 = 1/2$
[a] μ_{R_e} transformed to B_e
[b] Schombert (1987); μ_{V_e} transformed to μ_{B_e}
[c] Thuan and Romanishin (1981)
[d] Morbey and Morris (1983); μ_{V_e} transformed to μ_{B_e}
[e] r_e computed using B profile
[f] r_e computed using R profile

7 Discussion

7.1 Isophote position angles

Isophotal twisting is one of many probes into the morphology of elliptical galaxies. The most obvious cause of isophotal twisting is a tidal disturbance because of a nearby companion, which can be a common occurrence in galaxy clusters. The symmetric isodensity surfaces would not share common axes in this case, and the galaxy is not in dynamical equilibrium. Isophotal twisting can also indicate that the galaxy is neither oblate nor prolate, but triaxial (i. e., not a figure of rotation), and with this geometry the isodensity surfaces share common principal axes. This model can exist in dynamical equilibrium and in general possesses twisted isophotes. Following the discussion in Mihalas and Binney (1981), consider isodensity surfaces whose principal axes at small radius are prolate and vary smoothly with increasing radius such that they become oblate at large radius. Unless one of the galaxy's principal axes lie along the line of sight, the isophote will appear to twist, since the major axis of the prolate and oblate isodensity surfaces are not co-linear.

Porter et al. (1991) found that in a sample of brightest ellipticals in 175 Abell clusters, 20% showed isophotal twists greater than 40°. None of the galaxies studied here show compelling evidence for isophotal twisting of a similar degree (Figures 38 and 39). The BCG of AWM 4 appears to twist at radii greater than 60″, but this galaxy has a bright star located nearby which most probably influences the isophote

parameters. Masking the star made a slight improvement, but unfortunately because of its proximity to the galaxy, masking the star and its halo would also result in masking out much of the galaxy. To treat this galaxy properly, the star would have to be subtracted from the image. Furthermore, the errors become so large where the twisting begins that the position angle is consistent with zero change. At first glance, the BCG of MKW 5 appears to have some isophotal twist. However, this galaxy is nearly round, which means position angle measurements have little significance. The dominant galaxy of MKW 3S shows a change of about 6° from $r = 20''$ to $r = 100''$. However, this evidence is marginal, given that the error bars cover 4°. Even if these isophotal twists are real, they are insignificant compared with the amount of twisting observed in some galaxies.

The major axis position angle of cD galaxies in rich clusters show many interesting alignments. For example, Struble (1990) has found that in Coma-like clusters, the major axis of the BCG is aligned with the long axis of the parent cluster and also with the line joining the two brightest members. Similar alignments have been observed in poor clusters. Flin et al. (1995) has found that the BCGs of the MKW and AWM poor clusters are aligned with the parent cluster position angle. Fuller (in preparation) will show that the major axis of the MKW and AWM poor cluster BCGs point to nearby rich clusters. These alignments are important pieces of information, since they must be explained by any theory of BCG formation. Since both poor and rich cluster BCGs show alignments, the processes responsible for their formation must be independent

of the cluster richness.

7.2 Isophote ellipticities

Figures 40 and 41 show that there is a common general trend towards increasing ellipticity (flattening) with radius of the BCGs. This trend has been noted previously in studies of rich cluster cD galaxies (Porter et al., 1991), and is not caused by rotation effects. The BCGs of MKW 2S and AWM 4 show smoothly increasing ellipticities, while the BCGs of MKW 3S, MKW 4, and AWM 5 have small bumps at radii less than 50″. These bumps cannot be caused by seeing effects, since these will only be important inside 5 times the FWHM (§4.4), which very conservatively is 10″. The BCG of MKW 4 also shows a downturn in the ellipticity profile at radii larger than 100″. Of the 175 galaxies studied by Porter et al. (1991), 40% had no change in slope in the ellipticity profile, 50% showed at most one slope change, and in only 9% were there more than two slope changes. Thus, bumpy ellipticity profiles are uncommon. It could be argued that the variations in the ellipticity profiles of the BCGs of MKW 3S and AWM 5 are insignificant, given the errors, but the local minimum at $r = 15''$ and the local maximum at $r = 95''$ in the profile of MKW 4 do seem real.

The two exceptions to the flattening trend are the BCGs of MKW 5 and MKW 2; the latter shows only a marginal increase and has large errors.

Plots were made of position angle versus ellipticity, but no obvious relations were apparent. This is in agreement with Porter et al. (1991), who searched for correlations

among ellipticity, ellipticity gradient, isophote twisting, effective radius, luminosity, etc., but found none.

7.3 Surface photometry

Figures 30 to 37 show the B and R profiles of the poor cluster BCGs. At surface brightnesses of $\mu_B \leq 23$, the profiles computed in this study generally agree fairly well with other published profiles. Exceptions are the R profile of MKW 2 (Figure 33) and the B profile of MKW 5 (Figure 37), which were not obtained under photometric conditions (as mentioned in §5.1) and have an unreliable zero point.

The error bars shown in Figures 30 to 37 were calculated using Poisson shot noise, and assuming a 0.5% error in sky subtraction and 1.0% error in flat fielding. For comparison, TR believe their profiles are accurate to better than 0.1 mag arcsec^{-2} for $\mu < 25$ mag arcsec^{-2} and increases to several tenths of magnitudes arcsec^{-2} at $\mu = 27$ mag arcsec^{-2}. MK claim accuracy that is very similar to TR.

At fainter brightnesses, the agreement is not good and worsens with radius; the profiles systematically become brighter than profiles published by TR, MM and MK. At first glance, the profiles seem to show the same characteristic break that are observed in cD galaxies. However, cD envelopes begin around $\mu_B = 25 - 27$ mag arcsec^{-2}, and the profile breaks in this study begin at the 23rd magnitude. David Carter (personal communication) suggested that a lack of agreement between our profiles and previous photographic profiles is not unlikely, since photographic

plates can suffer from problems, such as non-linearity at low brightnesses. Comparison with other CCD work is more useful, but unfortunately the data presented here do not agree with the CCD data of MK either (Figures 30, 31, and 37). A zero point shift can be added to register the profiles of the MKW 5 BCG, but they do not have the same shape. Their CCD photometry agrees well with the previous photographic photometry. MK did not have large spatial coverage, which makes the calculation of the sky brightness difficult. Even though both the photographic studies and the CCD study could possibly have faults, it is much more likely that the discrepancies are the result of some systematic error committed in this study.

Many possible explanations for the discrepancies have been investigated. Contamination from other stars and galaxies could make the profiles seem brighter, but there are two compelling arguments that contamination is not the cause of the problem: 1) masking was tested on three images, and the profiles did not change; 2) the Abell 2052 frame is much more heavily contaminated than the poor cluster frames, and yet the discrepancy is smaller than for many of the poor clusters.

A consistent underestimation of the sky would make the profiles too bright. An error in the actual sky measurement seems unlikely since it was measured with two independent methods that agreed with each other. Also, error in sky measurement is a random, not systematic error, and hence should produce profiles that are sometimes too dim, which was not observed. There may be underlying factors, however, that could cause the sky to appear too dim. It is possible that a gradient (from a

flat fielding error) in the region common to the galaxy and overlapping frame could manifest itself in such a way that the sky measurements are systematically too low. The accuracy of the flat fields was tested on images that contained very few objects, and was always found to be $\leq 1\%$ of sky. However, it is a very difficult task to assess the flat fielding accuracy on the program images, since the BCG fills a large portion of the frame, and the cluster galaxies also add contamination.

There could also be a systematic error in the intensity registration between the galaxy and overlap images, perhaps caused by flat fielding inaccuracies. A method of intensity registration that was not sensitive to flat fielding errors was tested to see if improvements could be made. The image of MKW 2s had two bright stars in the region common to the overlap and galaxy frames. The pixel intensities were summed within a circular radius centred on these two stars on both the images; the intensity offsets were 59 and 47 ADU. Not only are they in disagreement by 8 ADU, they disagree with the result of 39 ADU obtained with the $k\sigma$ scheme. Even if the star measurements had agreed (at, say 47 ADU) this would cause an even greater underestimation of the sky, and hence the profiles would look even brighter. Thus, this method is not useful.

To assess the amount by which the profiles disagreed, various sky corrections were applied in an attempt to make the profiles match (Figure 42). The maximum correction needed for any profile was 2% (8 ADU for the B filter), which is four times the assumed error in the sky measurement. When the profiles were made to match

up, it was found that they truncated sooner than in the other studies. This implies that the photographic plates are more sensitive than the CCD chip used here, which does not seem likely. For comparison, TR obtained their data with the Palomar 48 inch Schmidt telescope, MK used 1.3m and 0.9m telescopes, and MM used the 4m CTIO telescope. Thus, telescope size cannot be a factor for the MK and TR data.

There are three profiles that warrant individual attention. The B profile for MKW 2 agrees well with the MM profiles. Schombert (1986) also published a profile for MKW 2 that agreed well with TR but not with MM, and therefore reasoned that MM had used a sky value that was too low. Schombert (1986) found that the data of MM disagreed with his own and that of other authors, and therefore decided to exclude MM's data in his study. Thus, the data of MM should be considered to be of lesser importance than the newer CCD data of MK. It is interesting to note that within the error bars used, the profile for MKW 2 agrees with both the TR and MM data. The profile for MKW 4 shows a $\simeq 1$ magnitude colour gradient, which is likely erroneous. Such a colour gradient was not observed by McNamara and O'Connell (1992) in their study of colour gradients in cooling flow clusters. Inspection of the B image of MKW 4 reveals a large, diffuse lump on the edge of the galaxy, but there was no trace of this peculiarity in R. The origin of this peculiar feature is unknown. As mentioned in §7.1, the BCG of AWM 4 has a close companion star, and an attempt was made to mask this out. Undoubtedly, the close companion is partly responsible for the profile being too bright, and subsequently the profile slope is too shallow.

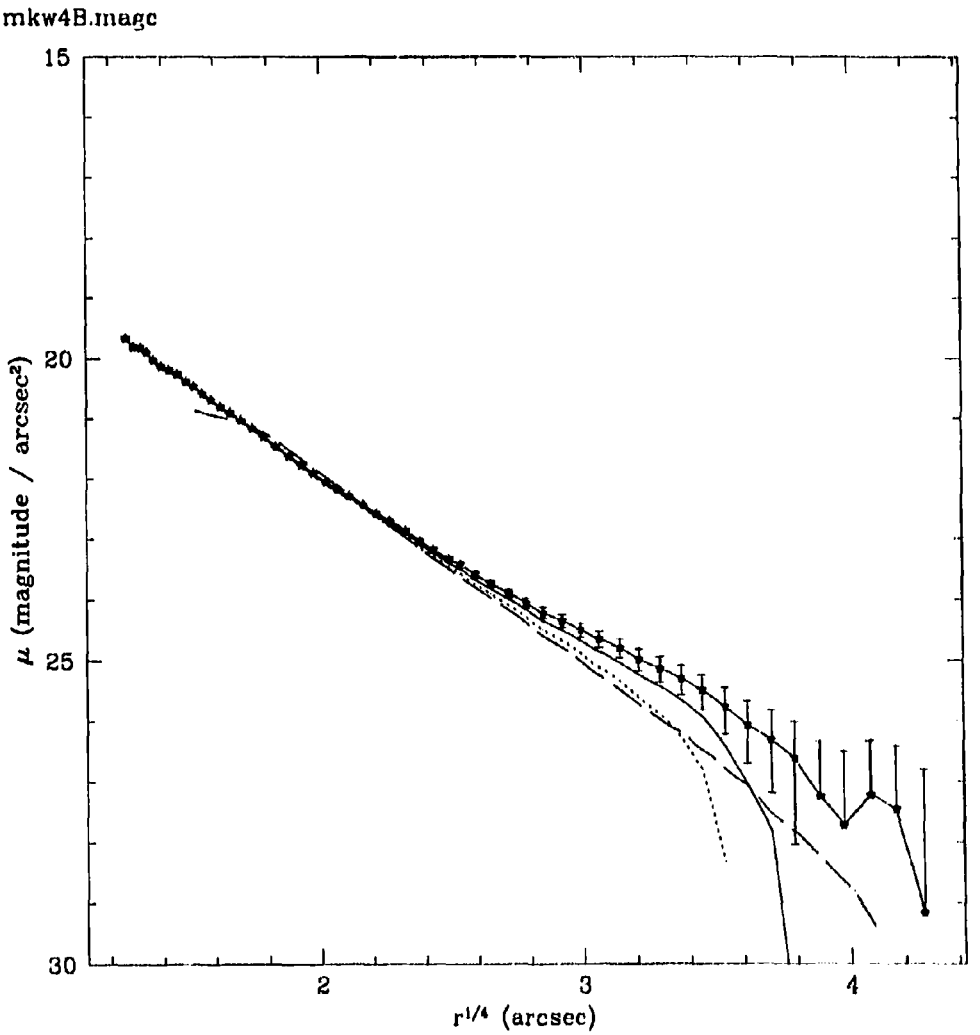

Figure 42: Various corrections were applied to the MKW 4 profile to match it with previous studies. 1% (solid line) and 2% (dotted line) of sky was added to the original profile (stars). Data from TR, g transformed to B (dashed line) is shown for comparison.

7.4 de Vaucouleurs parameters

The purpose of surface photometry is to reduce two dimensional images to one dimensional profiles, which subsequently can be fit to models to derive luminosity and structure parameters. To this end, all of the profiles have been fitted to a de Vaucouleurs law and the effective radii and surface brightness were computed (Table 7). Although the profiles are of questionable accuracy at low brightnesses, the errors in the profiles are smaller where the profiles are in better agreement, and so here the de Vaucouleurs fits are weighted more heavily. The maximum disagreement in the effective surface brightness is 1.4 magnitude arcsec^{-2} for MKW 2s, and the disagreement for AWM 4 is also high at 1.2 magnitude arcsec^{-2}. All the other effective surface brightnesses agree to better than 0.7 magnitude arcsec^{-2}. It should be noted for comparison purposes that the μ_{B_e} values of MM and TR disagree by 0.9 magnitude arcsec^{-2}. Also, a deviation from the de Vaucouleurs law does not imply that the surface photometry is incorrect, for there are many elliptical galaxies that do not fit the de Vaucouleurs law very well (Mihalas and Binney, 1981).

Figure 43 shows the effective surface brightness as a function of the effective radius for cD, D, gE, and normal elliptical galaxies, along with the BCGs of the MKW and AWM poor clusters. A brightward extrapolation of the relation for normal elliptical galaxies determined by Kormendy (1980) fits the poor cluster BCGs quite well. cD galaxies are distributed over a much greater range of r_e and μ_e than the poor cluster BCGs, and the gE galaxies have higher μ_e. The poor cluster BCGs have a distribution

similar to D galaxies, however the poor cluster BCGs have a smaller dispersion about Kormendy's relation. Thus, based on the de Vaucouleurs parameters, the poor cluster BCGs can be classified as D galaxies (or perhaps a subset of D galaxies); this is consistent with a classifications done by other authors (Thuan and Romanishin, 1981; Schombert, 1986) based on profile shapes.

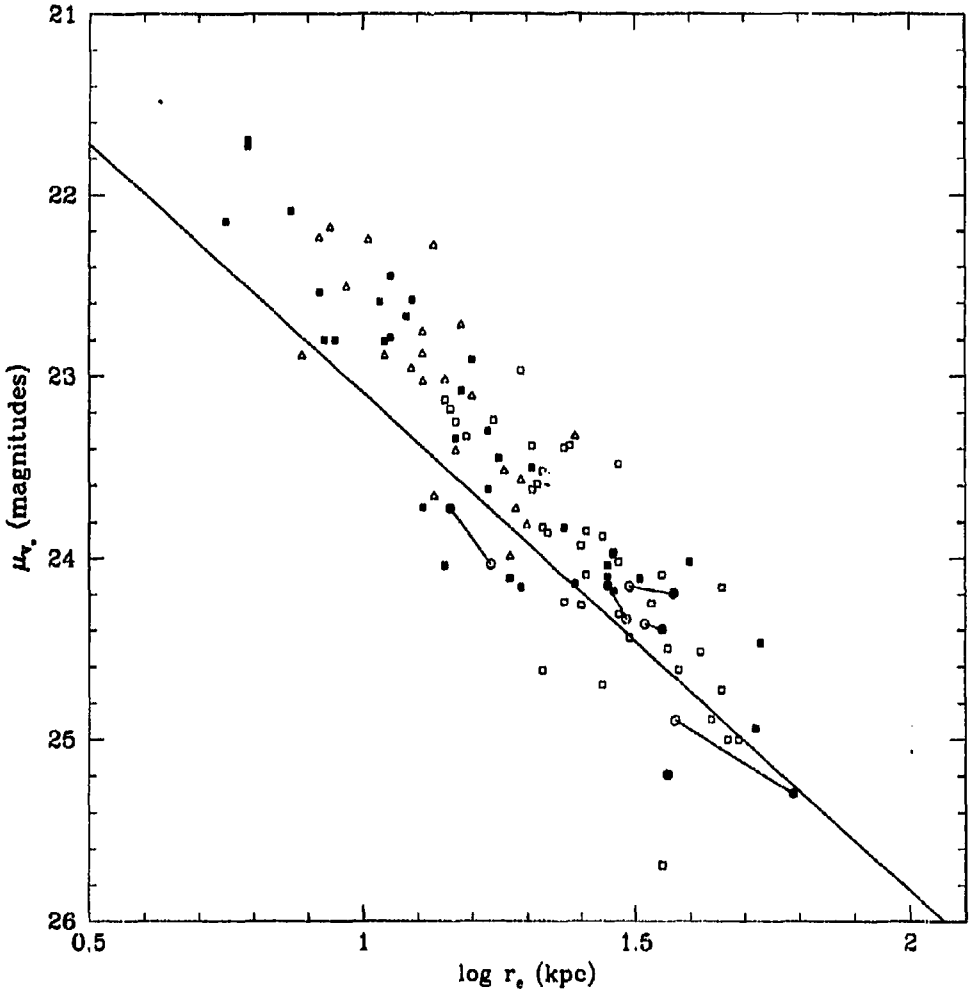

Figure 43: de Vaucouleurs effective brightness and radius for the various galaxy types. The filled circles are the poor cluster BCGs examined in this study, and the open circles are the data obtained by MK. The five galaxies common to both this study and MK are connected by a line. The filled squares are cDs, the open squares are Ds, and the triangles are gEs from the data given by Schombert (1987). The straight line is the relation for normal ellipticals found by Kormendy (1980). The $(1+z)^4$ cosmological dimming correction has been applied.

8 Summary

CCD images of the BCGs in the MKW and AWM poor clusters were taken with the 1.0m JKT telescope. Some of the images suffered from an unstable bias level, and so a non-standard method of bias subtraction was necessary. The images were flattened using twilight and sky flats, and are thought to be accurate to 1%. The galaxy centred and overlap frames were spatially registered, mosaicked, then brought to a common intensity level by computing the intensity in the region common to both images. This format allows tracing the halo out far enough that the true sky level is reached.

Isophote position angles and ellipticities were measured with the STSDAS routine `ellipse`. Five of the seven poor cluster BCGs show significant isophotal flattening with increasing radius, a common trend among gE, D, and cD galaxies. Three of the BCGs (MKW 3S, 4, and AWM 5) show uncommon structure in the ellipticity profiles (changes in slope). No significant amount of isophotal twisting was observed in any of the galaxies, therefore none are being tidally disrupted or are triaxial systems. Similar to their rich-cluster cousins, the poor cluster BCGs show position angles alignment effects which suggests that the rich and poor cluster BCGs do share some common formation processes.

New software was developed to measure the isophotal magnitudes, because of a limitation of `ellipse`. The new algorithm used an iterative $k\sigma$ clipping scheme to remove contaminating objects, and is a significant improvement over the brightest

pixel clipping scheme used by `ellipse`. The profiles compared well with other published data at surface brightnesses $\mu_B \leq 23$ mag arcsec^{-2}, but do not agree well at dimmer magnitudes. The source of this discrepancy is unclear; a variety of possibilities have been considered, such as flat fielding problems. The most likely cause of the problem is a systematic underestimation of the sky intensity. Since the profiles at faint brightnesses are of questionable validity, no conclusion regarding the existence of diffuse halos surrounding the galaxies may be drawn.

A de Vaucouleurs law was fit to the profiles, and the de Vaucouleurs parameters were compared with other published data. There were disagreements of up to 1.4 mag arcsec^{-2} (MM and TR have disagreed by up to 0.9 mag arcsec^{-2}). On a plot of the effective radius versus effective surface brightness, the poor cluster BCGs lie in the same region as D galaxies (which do *not* have diffuse envelopes), but lie closer to the relation of Kormendy (1980) for normal elliptical galaxies. The classification of the poor cluster BCGs as D galaxies is consistent with classifications based on profile shapes (Thuan and Romanishin, 1981; Schombert, 1986).

Since the poor and rich cluster BCGs do share some similarities (position angle alignments and increasing flattening with radius) there must be formation processes common to both types of clusters that are independent of cluster richness. It seems likely that the poor cluster BCGs do not have diffuse envelopes, based on the de Vaucouleur profiles and on previous studies. Hence, it may be reasoned that a rich cluster environment is necessary for the formation of diffuse envelopes.

Glossary

ADU (Analogue Digital Unit) The analogue signal from the CCD pixels are converted to a digital signal by an analogue to digital converter (ADC). The photons incident on the CCD chip cause electrons to accumulate in the pixels. The pixel intensity is measured in ADU and is given by the number of ele ons multiplied by the gain.

BCG (Brightest Cluster Galaxy) The dominant member of a cluster of galaxies. Similar terms include Brightest Cluster Elliptical (BCE) and Brightest Cluster Member (BCM).

bias frame An exposure of zero time. This exposure records any structure in the chip cause by the electronics alone.

CCD (Charge Coupled Detector) A two dimensional grid of light sensitive picture elements (pixels) on a very thin silicon wafer.

cD The largest, most massive galaxies in the Universe. These galaxies are surrounded by very large (up to 2 Mpc), faint envelopes.

dark current Exposing a CCD chip to photons causes currents to run though the chip. However, in the absence of all light, there still may be a small current present (the dark current) which must be removed to obtain accurate intensities.

dithering When taking successive pictures of the same area of the sky, the telescope

is shifted by a few arcseconds and hence objects (stars, galaxies, etc.) do not occupy the same position on the CCD.

flat fields Every CCD chip has pixel to pixel differences in sensitivity. These may be corrected by exposing the CCD to a uniformly illuminated source (e. g., the twilight sky). This exposure is called the flat field and is divided into the program frames to remove the pixel to pixel sensitivity differences.

FWHM (Full Width at Half Maximum) The width of a Gaussian function at one half of its maximum value.

gain An electronic amplification applied to the CCD chip, measured in electrons per ADU.

overscan region Every CCD chip contains a few consecutive columns along one edge that are not exposed to any light. They record the instrumental bias signature, which varies with time and hence must be corrected on each exposure individually.

PSF (Point Spread Function) The function that describes the image produced by a point source. Diffraction and atmospheric disturbances cause point sources to deviate from their theoretical shape.

read noise The readout electronics introduces an uncertainty (the read noise) in the number of electrons present in each pixel.

References

C. E. Albert, Richard A. White, and W. W. Morgan. 1977. *ApJ*, 211:309.

Timothy C Beers and Margaret J. Geller. 1983. *ApJ*, 274:491.

S. P. Boughn and J. R. Kuhn. 1986. *ApJ*, 309:33.

David Burstein and Carl Heiles. 1984. *ApJ*, 54:33–79.

Claude R. Canizares, Gordon C. Stewart, and Andrew C. Fabian. 1993. *ApJ*, 272: 449.

David Carter. 1977. *MNRAS*, 178:137.

Matthew Colless, D. Burstein, G. Wegner, R. P. Saglia, R. McMahan, R. L. Davies, E. Bertschinger, and G. Baggley. 1993. *MNRAS*, 262:475.

G. de Vaucouleurs. 1948. *Ann. d'Astrophys.*, 11:247.

A. Dressler. 1978. *ApJ*, 222:23.

A. Dressler. 1984. *ARAA*, 22:185.

A. C. Edge. 1991. *MNRAS*, 250:103.

A. C. Fabian, P. E. J. Nulsen, and C. R. Canizares. 1984. *MNRAS*, 201:933.

P. Flin, D. Trevese, J. Krywult, and G. Cirimele. In *Observational Cosmology; SESTO Meeting*, 1995.

M. J. Geller and P. J. E Peebles. 1976. *ApJ*, 206:939.

R. I. Jedrzejewski. 1987. *NMRAS*, 226:747.

I. R. King. 1971. *PASP*, 83:199.

J. Kormendy. 1980. *ApJ*, 217:406.

A. U. Landolt. 1992. *AJ*, 104:340.

Glen Mackie. 1992. *ApJ*, 400:65.

Glen Mackie, N. Visvanathan, and Dave Carter. 1990. *ApJ*, 73:637.

E. M. Malumuth and D. O. Richstone. 1984. *ApJ*, 276:413.

Eliot M. Malumuth and Robert P. Kirshner. 1985. *ApJ*, 291:8.

T. A. Matthews, W. W. Morgan, and M. Schmidt. 1964. *ApJ*, 140:35.

Brian R. McNamara and Robert W. O'Connell. 1992. *ApJ*, 393:579.

D. Merritt. 1984. *ApJ*, 276:26.

D. Merritt. 1985. *ApJ*, 289:18.

Dmitri Mihalas and James Binney. *Galactic Astronomy*, page 332. W. H. Freeman and Company, 1981.

Christopher Morbey and Stephen Morris. 1983. *ApJ*, 274:502.

W. W. Morgan, Susan Kayser, and Richard A. White. 1975. *ApJ*, 199:545.

D. M. Neumann and H. Böhringer. 1995. *AA*, 301:865.

James E. O'Donnell. 1994. *ApJ*, 422:158.

A. Oemler. *The Astronomy and Astrophysics Encyclopedia*, page 97. Van Nostrand Reinhold, 1992.

J. P. Ostriker and M. A. Hausman. 1977. *ApJL*, 217:L:125.

Reynier F. Peletier, Roger L. Davies, Garth D. Illingworth, Lindsey E. Davis, and Michael Cawson. 1990. *AJ*, 100:1091.

Alain C. Porter, Donald P. Schneider, and John G. Hoessel. 1991. *AJ*, 101:1561.

Douglas O. Richstone. 1976. *ApJ*, 204:642.

A. R. Sandage. 1973. *ApJ*, 183:711.

P. Schechter. 1976. *ApJ*, 203:297.

R. Schild and Marc Davis. 1979. *AJ*, 84:311.

D. P. Schneider, J. E. Gunn, and J. G. Hoessel. 1983. *ApJ*, 268:476.

James M. Schombert. 1986. *ApJS*, 60:603.

James M. Schombert. 1987. *ApJS*, 64:643.

James M. Schombert. 1988. *ApJ*, 328:475.

Eric Smith and T. M. Heckman. 1989. *ApJS*, 69:365.

Mitchell F. Struble. 1990. *AJ*, 99:743.

Trinh X. Thuan and William Romanishin. 1981. *ApJ*, 248:439.

Scott D. Tremaine and Douglas O. Richstone. 1977. *ApJ*, 212:311.

Juan M. Uson, Stephen P. Boughn, and Jeffrey R. Kuhn. 1991. *ApJ*, 369:446.

Sidney van den Bergh. 1977. *PASP*, 89:746.

Sidney van den Bergh. 1983. *PASP*, 95:275.

Appendix: *ANNULI* code listing

```
/*                    annulus.c
   USE:  annulus parmfile ellipse_output image.text ouput_file

   AUTHOR:  Todd Fuller, Saint Mary's University, fuller@ap.stmarys.ca

   all files must be text files!
   no column headers, or other extraneous info!

   parmfile must contain:
   xcenter, ycenter, theta, ellipticity, #ellipse parameters (float)
   minimum a, maximum a, ajump, anwidth, #annuli pamameters  (float)
   lsigfac,          #elliminate points lsigfac*sigma < mean (float)
   usigfac,          #elliminate points usigfac*sigma > mean (float)
   maxiter, miniter, #termination critera for iterations (integer)
   minchange,        # "                                 (float)
   linear_flag       #linear increase in a (0=no,1=yes)  (integer)
   xdim, ydim,       #dimensions of image                (integer)
   a_cutoff          #when to stop using ellipse output  (float)
   example parmfile:
   ----------------------------
   10.0 25.0 45.3 0.30 10.0
   50 0.5 5.0 1.0 1.0
   10 10 5.0 0
   50 50 15.00
   ----------------------------
   C is not really picky about number of spaces between numbers,
   what is on what line, etc., so you can put each number on it's
   own line if you like.

   ellipse output contains the output from the iraf routine ellipse
   use tprint or tdump to make a text file from the ellipse output
   ellipse_output must contain:
   a, x, y, theta, ellipticity

   image.text is a text file containing the pixel intensities.
   create this file from an image by using the iraf routine wtextimage
   do not have wtextimage write a header!!!!

   output_file is created by the program, and will be overwritten if
   it exists without warning.
```

```
   output_file contains:
   a, ainner, aouter, number_of_pixels, integrated_intensity,
   mean_intensity, standard_deviation, number_of_iterations

   Algorithm starts at amin and increases a by ajump if linear == 1 or
   increases a like this: a *= (1+ajump) if linear = 0
   and stops when amax is reached.  The width of the annulus is
   computed if linear = 0, or if linear = 1 the width of the annulus
   is specified bynwidth.  When linear = 0, the annulus width used is
   the differenceetween a and a*(1+ajump).

   The program reads the ellipse output and uses the ellipse center,
   position angle, and ellipticity to compute the ellipses.
   Once a > a_cutoff, the program holds the ellipse center, position
   angle and ellipticity fixed at the values specified in parmfile.
   The algorithm looks at each pixel within the specified dimensions,
   and determines which elliptical annuli the pixel belongs to (note
   that one pixel may belong to more than one annuli).
   Then, these statistics are computed on pixel intensities within the
   elliptical bins: mean, sigma, N.  Then, iteratively, the
   algorithm retains the pixels that are:
   lsigfac*sigma - mean <= pixel intensity <= usigfac*sigma + mean
   and discards all others.  The iterative process is continued while
   the iteration number is less than miniter and less than maxiter.
   Once the minimum number of iterations have been done, the algorithm
   willtop when reaching maxiter, or when the %change between the last
   mean and the current mean intensity is less than minchange.
 */

/*define PRECISION float to  use single precision numbers
   define PRECISION double to use double precision */
#define PRECISION double

/*this sets a print format string */
/*#define Pf "l" */
#define Pf ""

/*this sets a read format string */
#define Rf "l"

#include <math.h>
#include <stdio.h>
```

```
#include <stdlib.h>
#include <string.h>
#include <values.h>
#define YEP  1
#define NOPE 0

/* program will plot ellipses when compiled under Borland C */
/*#define graphics */

/*structure for the elliptical annuli bins */
struct bin_struct
  {
    PRECISION *intens;
    struct bin_struct *next;
  };

/*structure for the ellipse parameters and related data */
struct ell_parm_struct
  {
    PRECISION x, y;
    PRECISION teta;
    PRECISION eps;
    PRECISION A1, B1, C1, D1, E1, F1; /*parameters for the */
    PRECISION A2, B2, C2, D2, E2, F2; /*general ellipse equation*/
    PRECISION a, b, a1, b1;
    PRECISION a2, b2;
    struct bin_struct *head;
    PRECISION sum, sum_sq, mean, sigma, start_sigma;
    long N, startN;
    int last_iter;
  };

/*input parameters */
struct input_parm_struct
  {
    PRECISION Fx, Fy, Fteta, Feps, amin, amax, ajump, anwidth;
    PRECISION lsigfac, usigfac;
    int miniter, maxiter;
    PRECISION minchange;
    int linear;
    int xdim, ydim;
    PRECISION a_cutoff, a_last;
```

```
    int num_annuli;
  };

#ifdef graphics
#include <conio.h>
#include "display.c"
#endif

void compute_coeffs (struct ell_parm_struct *ep);
struct input_parm_struct *get_parms
    (char *filename, struct input_parm_struct *ip);
PRECISION *readimage
    (char *filename, PRECISION * image, struct input_parm_struct *ip);
struct ell_parm_struct *get_ellipse
    (char *ellipse_data_file, struct ell_parm_struct *ell_parm,
     struct input_parm_struct *ip);
PRECISION ellval1
    (struct ell_parm_struct ep, PRECISION x, PRECISION y);
PRECISION ellval2
    (struct ell_parm_struct ep, PRECISION x, PRECISION y);
void bin_it (struct ell_parm_struct *ell_parm,
     struct input_parm_struct *ip,
     PRECISION * image);
void iterate
    (struct ell_parm_struct *ep, struct input_parm_struct *ip);
void output
    (char *outfile_name, struct ell_parm_struct *ell_parm,
     struct input_parm_struct *ip);

int main (int argc, char *argv[])
{
  struct ell_parm_struct *ell_parm = NULL;
  struct input_parm_struct *ip = NULL;
  PRECISION *image = NULL;
  char *parm_file_name, *ellipse_output_name;
  char *image_data_name, *outfile_name;

  if (argc != 5)
    {
      printf ("useage: annulus parm_file ellipse_output"
          " imagedata outfile\n");xit (0);
    }
```

```
#ifdef graphics
  Initialize ();
#endif

  parm_file_name = argv[1];
  ellipse_output_name = argv[2];
  image_data_name = argv[3];
  outfile_name = argv[4];

  printf ("\n %s \n", ellipse_output_name);

  /*get the input parameters */
  ip = get_parms (parm_file_name, ip);

  /*read the ellipse output */
  ell_parm = get_ellipse (ellipse_output_name, ell_parm, ip);

  /*read the image data */
  image = readimage (image_data_name, image, ip);

  /*put the pixels into the elliptical bins */
  bin_it (ell_parm, ip, image);

  /*plot the data */
#ifdef graphics
  plot_it (ell_parm, ip, image);
  while (!kbhit ());
  closegraph ();
#endif

  /*calculate the mean intensity in the annuli */
  iterate (ell_parm, ip);

  /*output the results */
  output (outfile_name, ell_parm, ip);

  return (0);
}

/*this procedure calculates the mean, sigma of the pixels within
  the elliptical annuli, then throws out the pixels that are
```

```
  beyond l/usigfac*sigma from the mean. */
void iterate
    (struct ell_parm_struct *ep, struct input_parm_struct *ip)
{
  struct bin_struct *prev_ptr, *ptr, *next_ptr;
  PRECISION oldmean, oldsigma, oldsum;
  long oldN;
  int iteration;
  int b;

  /*loop through all annuli */
  for (b = 0; b < ip->num_annuli; b++)
    {
      /*initialize the old statistics */
      oldmean = ep[b].mean;
      oldsigma = ep[b].sigma;
      oldsum = ep[b].sum;
      oldN = ep[b].N;

      /*do the iterations */
      for (iteration = 1; iteration <= ip->maxiter; iteration++)
{
  /*remove all elements from the list that are more than
     u/lsigfac*sigma from the mean */
  prev_ptr = NULL;
  ptr = ep[b].head;
  while (ptr != NULL)
    {
      next_ptr = ptr->next;
      if (((ep[b].mean - ip->lsigfac * ep[b].sigma)
          > *ptr->intens) ||
  ((ep[b].mean + ip->usigfac * ep[b].sigma)
  < *ptr->intens))
{

  /*point is deviant, so delete it
    from the linked list */
  if (ptr != ep[b].head)
    /*not the first element, so prevptr
      has been defined */
    prev_ptr->next = next_ptr;
  else
```

```
    ep[b].head = next_ptr;
  free (ptr);
  /*prev_ptr stays where it is!!! */
}
      else
/*point stays in the list, so update prev_ptr */
prev_ptr = ptr;

      ptr = next_ptr;
    }

  /*all points in the list are now within
     u/lsigfac*sigma of the mean */
  /*now, recompute the statistics */
  ptr = ep[b].head;
  ep[b].N = 0;
  ep[b].sum = 0.0;
  ep[b].sum_sq = 0.0;
  while (ptr != NULL)
    {
      ep[b].sum += *ptr->intens;
      ep[b].sum_sq += *ptr->intens * *ptr->intens;
      ep[b].N++;
      ptr = ptr->next;
    }
  if (ep[b].N > 0)
    {
      ep[b].mean = ep[b].sum / (PRECISION) ep[b].N;
      ep[b].sigma = ep[b].sum_sq / (PRECISION) ep[b].N -
ep[b].mean * ep[b].mean;
      if (ep[b].sigma > 0.0)
ep[b].sigma = sqrt (ep[b].sigma);
      else
ep[b].sigma = MINDOUBLE;
    }
  else
    {
      ep[b].mean = MINDOUBLE;
      ep[b].sigma = MINDOUBLE;
    }

  /*is the iteration breaking criteria satisfied? */
```

```
  if (ep[b].mean != 0.0)
    {
      if ((iteration > ip->miniter) &&
  (((oldmean - ep[b].mean) / ep[b].mean * 100.0)
     < ip->minchange))
break;
    }

  if (ep[b].mean == oldmean)
    break;

  /*check if sigma is ok */
  if ((ep[b].sigma == MINDOUBLE) || (ep[b].N < 1))
    {
      ep[b].mean = oldmean;
      ep[b].sigma = oldsigma;
      ep[b].sum = oldsum;
      ep[b].N = oldN;
      iteration--;
      break;
    }

  /*output iteration to screen */
  /*printf("%3i %15.6"Pf"f %15.6"Pf"f %10li\n",
     iteration, ep[b].mean, ep[b].sigma, ep[b].N); */


  /*save the statistics */
  oldmean = ep[b].mean;
  oldsigma = ep[b].sigma;
  oldN = ep[b].N;
  oldsum = ep[b].sum;
  ep[b].last_iter = iteration;

} /*for iteration... */
    } /*for b... */
  return;
}

/*this procedure puts the pixels into elliptical bins */
void
bin_it (struct ell_parm_struct *ell_parm,
```

```
struct input_parm_struct *ip,
PRECISION * image)
{
  int i, j;
  int b;
  PRECISION e_outer, e_inner;
  struct bin_struct *ptr;

  /*scan over the image indices */
  for (i = 0; i < ip->xdim; i++)
    {
      for (j = 0; j < ip->ydim; j++)
{
  /*scan over the ellipse bins to see which
     bins this pixel belongs to */
  /* check that pixel hasn't been masked */
  if (*(image + j * ip->xdim + i) > -90.0)
    {
      for (b = 0; b < ip->num_annuli; b++)
{
  /*compute the ellipse equations */
  e_inner = ellval1 (ell_parm[b],
      (PRECISION) i, (PRECISION) j);
  e_outer = ellval2 (ell_parm[b],
      (PRECISION) i, (PRECISION) j);

  /*check that the pixel is inside the annulus,
    and has not been masked out by -99.0 */
  if ((e_inner >= 0.0) && (e_outer <= 0.0))
    {

      /*a hit */
      if ((ptr = calloc (1, sizeof (struct bin_struct)))
          == NULL)
{
  printf ("\n\nCannot allocate memory.  bin_it\n");
  printf ("\n i = %i j = %i \n", i, j);
  exit (0);
}

#ifdef graphics
      /*plot the point */
```

```
      {
int color;
color = 16 - (int) (fmod ((double) b,
    (double) 16));
putpixel (i, j, color);
      }
#endif

      /*link up the element to the list */
      if (ell_parm[b].head == NULL)
{
  ell_parm[b].head = ptr;
  ptr->next = NULL;
}
      else
{
  ptr->next = ell_parm[b].head;
  ell_parm[b].head = ptr;
}

      /*set intens to point to the corresponding
        element of image */
      ptr->intens = (image + j * ip->xdim + i);

      /*update the statistical parameters */
      ell_parm[b].sum += *ptr->intens;
      ell_parm[b].sum_sq += *ptr->intens *
          *ptr->intens;
      ell_parm[b].N++;
      ell_parm[b].startN = ell_parm[b].N;
      ell_parm[b].mean =
ell_parm[b].sum / (PRECISION) ell_parm[b].N;
      ell_parm[b].sigma =
ell_parm[b].sum_sq/(PRECISION) ell_parm[b].N -
ell_parm[b].mean * ell_parm[b].mean;

      if (ell_parm[b].sigma > 0.0)
ell_parm[b].sigma = sqrt (ell_parm[b].sigma);
      ell_parm[b].start_sigma = ell_parm[b].sigma;
    } /*end if (in annulus) */
} /*end for b... */
    } /*end if (pixel masked?) */
```

```
} /*end for j */
    } /*end for i */
  return;
}

/*feed in x,y into the general ellipse eqations
   if the result is greater than zero, the point is inside the ellipse
   other wise outside */
PRECISION
ellval1 (struct ell_parm_struct ep, PRECISION x, PRECISION y)
{
  PRECISION ell1;
  ell1 = ep.A1 * x * x + ep.B1 * x * y +
    ep.C1 * y * y + ep.D1 * x +
    ep.E1 * y + ep.F1;
  return (ell1);
}
PRECISION
ellval2 (struct ell_parm_struct ep, PRECISION x, PRECISION y)
{
  PRECISION ell2;
  ell2 = ep.A2 * x * x + ep.B2 * x * y +
    ep.C2 * y * y + ep.D2 * x +
    ep.E2 * y + ep.F2;
  return (ell2);
}

/*this procedure reads the ellipse output and computes the ellipse
   parameters.  When a_cutoff is passed, the fixed x,y,theta,
   ellipticity are used to compute the ellipse parameters */
struct ell_parm_struct *
get_ellipse (char *ellipse_data_file,
     struct ell_parm_struct *ell_parm,
     struct input_parm_struct *ip)
{
  FILE *ellipse_data;

  char string[300];
  char *token;
  int i;
  PRECISION a;
```

```
  /*allocate enough memory for the ellipse parameters array */
  a = ip->amin;
  ip->num_annuli = 0;
  while (a <= ip->amax)
    {
      if (ip->linear == YEP)
a += ip->ajump;
      else
a *= (1.0 + ip->ajump);
      ip->num_annuli++;
    }
  if ((ell_parm = calloc (ip->num_annuli,
      sizeof (struct ell_parm_struct))) == NULL)
    {
      printf ("\n\nCannot allocate memory for ell_parm\n");
      exit (0);
    }

  /*open ellipse data for input */
  if ((ellipse_data = fopen (ellipse_data_file, "r")) == NULL)
    {
      printf ("\n\nCannot open %s\n", ellipse_data_file);
      exit (0);
    }

  i = 0;
  while (fgets (string, 299, ellipse_data) != NULL)
    {

      if (i == ip->num_annuli)
{
  printf ("\n\narray out of bounds: Too many annuli\n");
  exit (0);
}

      token = strtok (string, " ");
      a = atof (token);
      if (a > ip->a_cutoff)
break;
      /*compute a1 and a2 */
      if (ip->linear == NOPE)
ip->anwidth = a * ip->ajump;
```

```
      if (ip->anwidth > 10.0)
ip->anwidth = 10.0;

      ell_parm[i].a = a;
      ell_parm[i].a1 = a - ip->anwidth / 2.0;
      ell_parm[i].a2 = a + ip->anwidth / 2.0;

      token = strtok (NULL, " ");
      ell_parm[i].x = atof (token);
      token = strtok (NULL, " ");
      ell_parm[i].y = atof (token);
      token = strtok (NULL, " ");
      ell_parm[i].teta = atof (token);
      token = strtok (NULL, " ");
      ell_parm[i].eps = atof (token);

      compute_coeffs (&ell_parm[i]);
      i++;
    }
  fclose (ellipse_data);

  /*now, compute the ellipse coefficients using
     the fixed ellipse parameters */
  if (a <= ip->amin)
    a = ip->amin;
  while (i < ip->num_annuli)
    {
      /*compute a1 and a2 */
      if (ip->linear == NOPE)
ip->anwidth = a * ip->ajump;

      ell_parm[i].a = a;
      ell_parm[i].a1 = a - ip->anwidth / 2.0;
      ell_parm[i].a2 = a + ip->anwidth / 2.0;
      ell_parm[i].teta = ip->Fteta;
      ell_parm[i].eps = ip->Feps;
      ell_parm[i].x = ip->Fx;
      ell_parm[i].y = ip->Fy;

      compute_coeffs (&ell_parm[i]);
```

```
      if (ip->linear == YEP)
a += ip->ajump;
      else
a *= (1.0 + ip->ajump);

      i++;
    }
  return ell_parm;
}

/*this procedure does the computation of the ellipse parameters
  given the x,y,theta,ellipticity,a */
void
compute_coeffs (struct ell_parm_struct *ep)
{
  PRECISION cos_teta, sin_teta;
  PRECISION a_sq, b_sq;
  PRECISION x, y;

  /*compute b, b1 and b2 */
  ep->b = ep->a * (1.0 - ep->eps);
  ep->b1 = ep->a1 * (1.0 - ep->eps);
  ep->b2 = ep->a2 * (1.0 - ep->eps);

  /*compute the inner ellipse coefficients */
  ep->teta = ep->teta - 90.0;
  ep->teta = ep->teta * M_PI / 180.0;
  cos_teta = cos (ep->teta);
  sin_teta = sin (ep->teta);
  a_sq = ep->a1 * ep->a1;
  b_sq = ep->b1 * ep->b1;
  x = ep->x;
  y = ep->y;
  ep->A1 = (cos_teta * cos_teta / a_sq) +
           (sin_teta * sin_teta / b_sq);
  ep->B1 = 2.0 * sin_teta * cos_teta * (1.0 / a_sq - 1.0 / b_sq);
  ep->C1 = (sin_teta * sin_teta / a_sq) +
           (cos_teta * cos_teta / b_sq);
  ep->D1 = -2.0 * x * ep->A1 - y * ep->B1;
  ep->E1 = -x * ep->B1 - 2.0 * y * ep->C1;
  ep->F1 = x * x * ep->A1 + x * y * ep->B1 + y * y * ep->C1 - 1.0;
```

```
  /*compute the outer ellipse coefficients */
  a_sq = ep->a2 * ep->a2;
  b_sq = ep->b2 * ep->b2;
  ep->A2 = (cos_teta * cos_teta / a_sq) +
           (sin_teta * sin_teta / b_sq);
  ep->B2 = 2.0 * sin_teta * cos_teta * (1.0 / a_sq - 1.0 / b_sq);
  ep->C2 = (sin_teta * sin_teta / a_sq) +
           (cos_teta * cos_teta / b_sq);
  ep->D2 = -2.0 * x * ep->A2 - y * ep->B2;
  ep->E2 = -x * ep->B2 - 2.0 * y * ep->C2;
  ep->F2 = x * x * ep->A2 + x * y * ep->B2 + y * y * ep->C2 - 1.0;

  return;
}

/*read the parameters that the program needs to run from file */
struct input_parm_struct *
get_parms (char *filename,
   struct input_parm_struct *ip)
{
  FILE *fptr;

  if ((ip = calloc (1, sizeof (struct input_parm_struct))) == NULL)
    {
      printf ("\n\nCannot allocate memory for ip\n");
      exit (0);
    }

  fptr = fopen (filename, "r");
  if (fptr == NULL)
    {
      printf ("\n\n Cannot open file %s\n", filename);
      exit (0);
    }

  fscanf (fptr, "%" Rf "f %" Rf "f %" Rf "f %" Rf "f %" Rf "f",
  &ip->Fx, &ip->Fy, &ip->Fteta, &ip->Feps, &ip->amin);
  fscanf (fptr, "%" Rf "f %" Rf "f %" Rf "f %" Rf "f %" Rf "f ",
  &ip->amax, &ip->ajump, &ip->anwidth, &ip->lsigfac,
  &ip->usigfac);
  fscanf (fptr, "%d %d %" Rf "f %d ",
  &ip->maxiter, &ip->miniter, &ip->minchange, &ip->linear);
```

```
  fscanf (fptr, "%d %d %" Rf "f ",
  &ip->xdim, &ip->ydim, &ip->a_cutoff);

  fclose (fptr);
  /*
     printf("%"Pf"f %"Pf"f %"Pf"f\n", ip->Fx, ip->Fy, ip->Fteta);
     printf("%"Pf"f %"Pf"f %"Pf"f\n", ip->Feps, ip->amin, ip->amax);
     printf("%"Pf"f %"Pf"f %"Pf"f\n", ip->ajump, ip->anwidth,
            ip->lsigfac);
     printf("%"Pf"f %d %d\n", ip->usigfac, ip->maxiter, ip->miniter);
     printf("%"Pf"f %d %d\n", ip->minchange, ip->linear, ip->xdim);
     printf("%d %"Pf"f\n", ip->ydim, ip->a_cutoff);
     exit(1);
   */
  return ip;
}

/*read the text image data */
PRECISION *
readimage (char *filename, PRECISION * image,
   struct input_parm_struct * ip)
{
  FILE *fptr;
  int i, j;
  PRECISION temp;

  if ((fptr = fopen (filename, "r")) == NULL)
    {
      printf ("\n\nCannot open %s\n", filename);
      exit (0);
    }
  /*allocate memory for image array */
  if ((image = calloc (ip->xdim * ip->ydim,
      sizeof (PRECISION))) == NULL)
    {
      printf ("\n\nCannot allocate memory for image array\n");
      exit (0);
    }

  for (j = 0; j < ip->ydim; j++)
    {
      for (i = 0; i < ip->xdim; i++)
```

```
{
  fscanf (fptr, "%" Rf "f ", &temp);
  *(image + j * ip->xdim + i) = temp;
}
    }
  fclose (fptr);
  return (image);
}

/*dump the output to file */
void
output (char *outfile_name, struct ell_parm_struct *ep,
struct input_parm_struct *ip)
{
  int b;
  PRECISION radius;
  FILE *fptr;

  /*open output file */
  if ((fptr = fopen (outfile_name, "w")) == NULL)
    {
      printf ("\n\nCannot open %s\n", outfile_name);
      exit (0);
    }

  /*loop through the elliptical annuli */
  for (b = 0; b < ip->num_annuli; b++)
    {
      radius = sqrt (ep[b].a * ep[b].b);
      fprintf (fptr, "%9.4" Pf "f " /* a */
       "%9.4" Pf "f " /* b */
       "%9.4" Pf "f " /* radius */
       "%9.4" Pf "f " /* a1 */
       "%9.4" Pf "f " /* a2 */
       "%15.6" Pf "f " /* sum */
       "%15.6" Pf "f " /* mean */
      /*"%15.6"Pf"f " start_sigma */
       "%15.6" Pf "f " /* sigma */
       "%8.3" Pf "f " /* x */
       "%8.3" Pf "f " /* y */
       "%6.2" Pf "f " /* teta */
       "%6.4" Pf "f " /* eps */
```

```
        "%3i " /* last_iter */
        "%10li " /* startN */
        "%10li " /* N */
        "\n",
        ep[b].a,
        ep[b].b,
        radius,
        ep[b].a1,
        ep[b].a2,
        ep[b].sum,
        ep[b].mean,
       /* ep[b].start_sigma, */
        ep[b].sigma,
        ep[b].x,
        ep[b].y,
        ep[b].teta,
        ep[b].eps,
        ep[b].last_iter,
        ep[b].startN,
        ep[b].N);
    }

  fclose (fptr);
  return;
}
```

Curriculum Vitae
Todd Michael Fuller
September, 1996

Address
Department of Physics and Astronomy
The University of Western Ontario
London, ON N6A 3K7
tfuller@phobos.astro.uwo.ca

Personal
Date of Birth: December 8, 1968
Place of Birth: Simcoe, Ontario, Canada
Citizenship: Canadian

Education

- Ph.D. 2000 — The University of Western Ontario
  Astronomy
  Advisor: Dr. Hugh M. P. Couchman
- M.Sc. 1996 — Saint Mary's University
  Astronomy
  Advisor: Dr. Michael West
- B.Sc. 1994 — University of Waterloo,
  Applied physics, Houours Co-operative program, teaching option
  Advisor: Dr. Gretchen Harris
- B.Ed. 1994 — Queen's University at Kingston,
  Education, physics and mathematics

Teaching Experience

- 09/94 - 04/96 — conducted introductory undergraduate astronomy laboratories
  lectured introductory astronomy classes on an incidental basis
  Saint Mary's University, Halifax
- 09/92 - 12/92 — taught grade twelve advanced and OAC physics
  J. S. Woodsworth Secondary School, Nepean, Ontario
- 09/91 - 12/91 — assisted teaching grade twelve general physics
  Thomas A. Stewart Secondary School, Peterborough, Ontario
- 01/91 - 04/91 — tutored students in mathematics and physics at a help centre
  Mohawk College of Applied Arts and Technology

Publications and Presentations

- "Alignment effects in the dominant galaxies of the MKW and AWM poor clusters", T. M. Fuller and M. J. West, in preparation
- "Angular Correlation Function of a Cluster of Galaxies", poster paper presented at the CASCA meeting, May 1994, University of Western Ontario

Awards

- Saint Mary's Graduate Student Scholarship, 1994-96
- Special University Scholarhip (University of Western Ontario), 1996

Professional References

- Dr. Hugh M. P. Couchman
  The University of Western Ontario
  London, ON N6A 3K7
  `hcouchman@coho.astro.uwo.ca`
- Dr. Michael J. West
  Saint Mary's University
  Halifax, NS B3H 3C3
  `west@sisyphus.stmarys.ca`
- Dr. David A. Clarke
  Saint Mary's University
  Halifax, NS B3H 3C3
  `dclarke@olympus.stmarys.ca`
- Dr. Gretchen L. Harris
  University of Waterloo
  Waterloo, ON N2L 3G1
  `glharris@astro.uwaterloo.ca`